R-08-26

Discrete fracture network modelling of a KBS-3H repository at Olkiluoto

G W Lanyon, Fracture Systems Ltd, St Ives, UK

P Marschall, Nagra, Wettingen, Switzerland

June 2008

SKB

Discrete fracture network modelling of a KBS-3H repository at Olkiluoto

G W Lanyon, Fracture Systems Ltd, St Ives, UK

P Marschall, Nagra, Wettingen, Switzerland

June 2008

A pdf version of this document can be downloaded from www.skb.se.

Foreword

Abstract

This report presents Discrete Fracture Network (DFN) models of groundwater flow around a KBS-3H repository situated at Olkiluoto. The study was performed in support of the Safety Case for the KBS-3H Concept, being jointly studied by SKB and Posiva. As part of the preliminary assessment of long term safety of a KBS-3H repository, a Process Report and an Evolution Report (evolution of the disposal system from the emplacement of the first canister to the long term) are being produced. In the course of the task definition the project team identified the need for complementary modelling studies aimed at increasing insight into the hydrodynamic evolution of the disposal system after waste emplacement. In particular, the following issues were identified as requiring input from hydrodynamic models:

- Probability of high inflow points which may cause buffer erosion.

- Time transients of inflows after construction of deposition drifts.

- Interference between deposition drifts and transport tunnels.

The DFN models represent the fault and fracture system in the planned repository volume at Olkiluoto. In particular, they represent the hydrogeologically significant features. The types of hydrogeological features included in the models are:

- Major Fracture Zones (MFZs).

- Local Fracture Zones (LFZs) and associated water conducting features (LFZ-WCFs).

- Water Conducting Features in the background rock (BR-WCFs).

These feature types are derived from the current geological and hydrogeological interpretations developed by Posiva. Several model variants were developed during the study and these variants were used for geometric simulations of the WCF network around the deposition drifts. A simple layout adaptation scheme has been applied to the network models to derive statistics for performance measures relating to the deposition drifts, compartments, plugs and super-containers.

A single fracture transient flow model was developed to provide insight to transient flow behaviour around deposition drifts. As part of the development of the single fracture model the importance of the storage term related to the EBS components within the drift was identified.

Detailed transient flow models of single drifts were developed to address the specific needs of the Project Team related to the hydrodynamic evolution of the near-field WCF network. The transient single drift models considered the response to excavation and emplacement of the EBS (super-containers, distance blocks and plugs). In addition dual drift models considered interference effects between drifts. Five different storage models were identified to bound the likely coupling between the hydraulic behaviour of the EBS and the geosphere.

Contents

1 Introduction

1.1 Background and scope

In 2002 SKB and Posiva initiated a feasibility study with the overall aim of developing the horizontal emplacement concept, KBS-3H, into a real alternative to the vertical emplacement concept, KBS-3V. In the KBS-3H concept several super-containers, each containing a copper-iron canister surrounded by a buffer of highly compacted bentonite, are emplaced in a horizontal deposition drift. General repository design and geological environment as assessed in the KBS-3H Project correspond to a repository for spent fuel sited at Olkiluoto.

The feasibility study includes a preliminary assessment of long-term safety, focussing on the buffer material in combination with the perforated disposal container enclosing the copper-iron canister and bentonite blocks around it. The Basic Design phase of KBS-3H was completed in 2003 /Thorsager and Lindgren 2004/ and comprised three major projects: technical development, preparations for demonstration at Äspö and long-term safety studies. The first plans for the studies to be performed within the safety case were set up in 2004 and specified the requirements for a Process Report and a Long-term Evolution Report (evolution of the disposal system from the emplacement of the first canister to the long term).

The KBS-3H Safety Case Project team (the Project team) has given Nagra responsibility for the compilation of these two reports. In the course of the task definition the Project team identified the need for complementary modelling studies aimed at increasing insight into the hydrodynamic evolution of the disposal system after waste emplacement. In particular, the following issues have been identified as requiring input from hydrodynamic models:

- Probability of high inflow points which may cause buffer erosion.
- Time transients of inflows after construction of deposition drifts.
- Interference between deposition drifts and transport tunnels.

A Discrete Fracture Network (DFN) modelling study in support of the Process Report and the Evolution Report was initiated in August 2005. The DFN was based on existing descriptive structural and hydrogeological models of the site /Hellä et al. 2006, Vaittinen et al. 2003/.

The implementation of the descriptive geosphere model in the DFN study, the specification of alternative geosphere representations and the definition of evolution scenarios were carried out in close collaboration with the Project team and in particular with the authors of the Process and Evolution Reports. Three progress meetings were held to monitor the task status and approve the proposed modelling procedure. Results were communicated to the Project team during the course of the study via technical notes covering: geosphere representation, geometric simulations; single fracture flow models and drift-scale flow models. The notes were revised on the basis of comments from the Project team and form the basis for this report. On completion of the DFN study, a final meeting was held in Finland on May 2, 2006 and comments were received from members of the Project team.

This report summarises the DFN study, describing the objectives, task procedure, achievements and conclusions as detailed in the Process and Evolution Reports. Comments and general feedback from the Project team are also addressed here.

1.2 Objectives of the DFN study

The DFN modelling study was set up to investigate expected behaviour of the disposal system and deviations from that behaviour.

The objectives related to expected system behaviour were:

- Justification of conceptual assumptions (key processes, relevant scenarios, system parameterisation, boundary conditions).
- Provision of input values for Performance Assessment (PA) calculations (geometric simulations, transient inflows).
- Assessment of robustness of conceptual assumptions.

and for deviations from expected behaviour:

- Identification of relevant processes and parameters.

The Process and Evolution Reports teams suggested pertinent modelling scenarios, schematics of which are shown in Figure 1-1.

In addition to these scenarios, specific outputs were requested:

- Time required to fill the 1.5 m³ void space in each super-container drift section by inflow from the fracture network.
- Rate of increase of fluid pressure in each super-container drift section after filling, plus the final equilibrium pressure (criteria relevant to the possibility of piping).
- Rate of water flow into and out of each super-container drift section once an equilibrium state has been reached.
- Travel paths and times to the next major fracture zone.

All but one of the teams' suggestions and requests were accomplished: it was not possible to identify flowpaths to the next major fracture zone as this requires site- rather than drift-scale models as used in this study. It was possible, however, to perform some preliminary particle tracking models (see Appendix B).

1.3 Numerical model

All simulations were performed using the CONNECTFLOW hybrid CPM/DFN model from Serco Assurance /see Serco Assurance 2002, Holton and Milický 1997/. Simulations were performed using version 9.1 of the code with minor user modifications to allow:

1) More flexible borehole/tunnel boundary conditions.

2) Additional model outputs (shaft trace maps).

3) Fracture length-transmissivity correlations as discussed in Chapter 2.

1.4 Report outline

The structure of this report follows the chronological sequence of work. The content of Chapters 2–5 are based on the technical notes distributed during the study. Feedback from the Project team on these notes and at review meetings has been extremely beneficial to the quality of the study.

Chapter 2 describes the development of the DFN models of the fault and fracture system in the planned repository volume at Olkiluoto. Data and interpretations on which the models are based are detailed, together with model calibration and verification (confidence building) procedures. In addition, calculations concerning the "up-scaled" effective hydraulic conductivity of the fault and fracture system are presented.
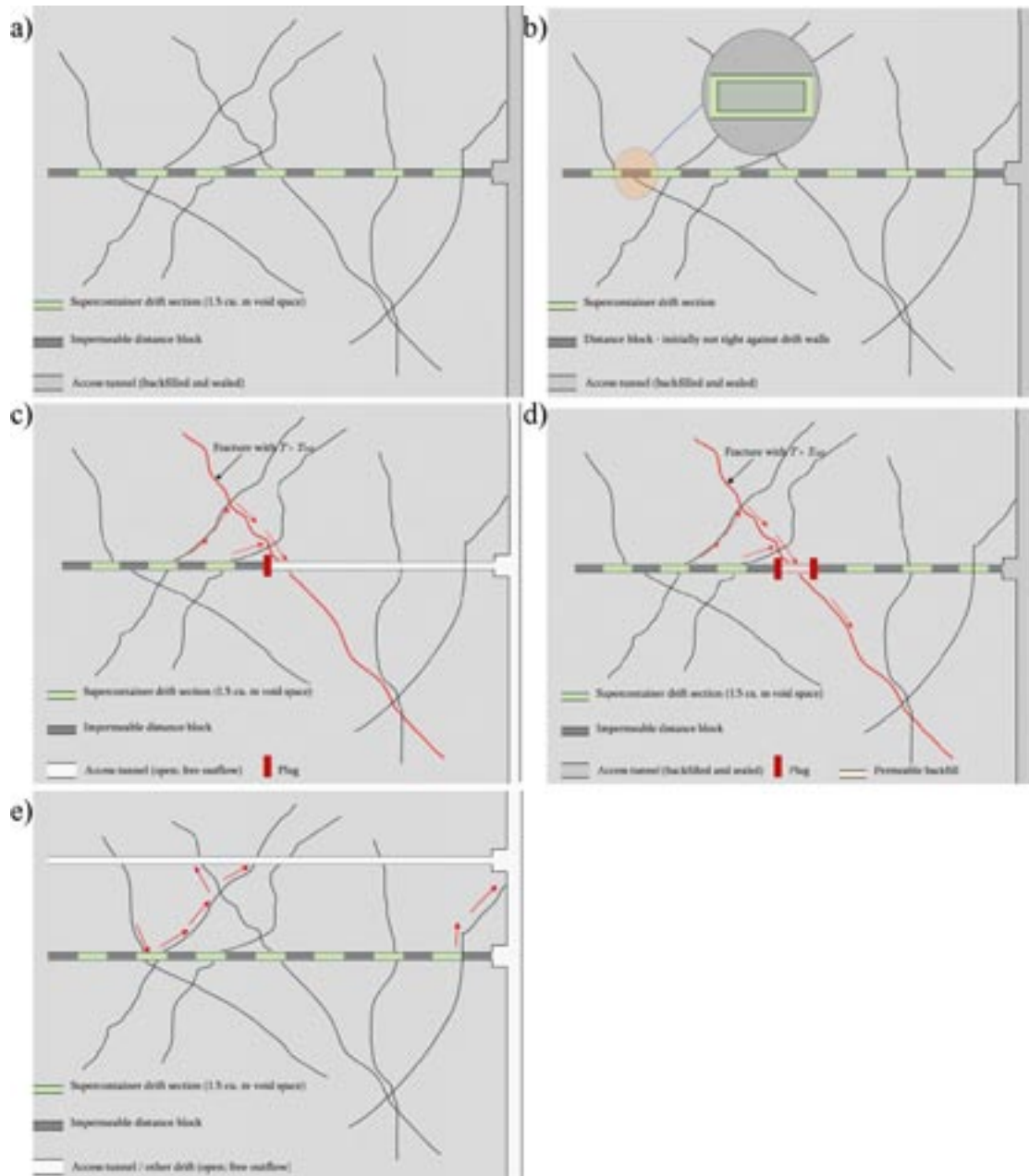
Figure 1-1. *Model scenarios outlined by Process and Evolution Reports teams. a) Reference variant, b) DAWE variant, c) Single compartment, d) multiple compartments, e) influence of adjacent drift.*

Chapter 3 describes geometric simulations of the fault and fracture system around a hypothetical repository. A simple set of layout adaptation rules concerning the location of repository components: compartment plugs, distance blocks and super-containers; have been used to determine statistics for measures such as numbers of super-containers emplaced per drift.

Chapter 4 describes a flow model for a single fracture considering the effect of excavation and emplacement. The model was used to illustrate the sensitivity to model parameters and develop understanding of likely flow and pressure responses at a super-container/distance block during excavation, operation and closure.

Chapter 5 describes the development of transient models of flow in the fracture system around single and dual drifts during excavation and emplacement. The outputs from the flow models include time-histories of the simulated pressure, pressure gradient and inflow.

11

Chapter 6 presents conclusions from the study, together with recommendations for application of results and suggestions for further interpretation and modelling. In addition, uncertainties and "open questions" related to the models are discussed. Chapter 6 also highlights the relevance of the calculations as input for the Process and Evolution Reports.

Appendix A gives summary statistics from the geometric simulations described in Chapter 3. Appendix B describes drift-scale steady state flow and particle tracking models performed as part of the study. Appendix C includes transient flow model results for the different drifts. Appendix D discusses fracture length scales used within the models and input data for the modelling is included in Appendix E.

2   Representation of the geosphere

2.1   Posiva's descriptive geosphere model

The DFN models represent the fault and fracture system in the planned repository volume at Olkiluoto. In particular, they represent the hydrogeologically significant features. The types of hydrogeological features included in the models are:

- Major Fracture Zones (MFZs).
- Local Fracture Zones (LFZs) and associated water conducting features (LFZ-WCFs).
- Water Conducting Features in the background rock (BR-WCFs).
- The background rock itself.

These feature types are derived from the current geological and hydrogeological interpretations developed by Posiva (see /Hellä et al. 2006/ and /Vaittinen et al. 2003/).

The geosphere description is based on that given in the Inflow Study performed by Pöyry Environment /Hellä et al. 2006/. It had originally been intended to use the model parameters given in the report from Hellä et al. (op cit) directly within the simulations. These values were intended only for trial simulations, however, and it was therefore decided to incorporate other information including the properties used by /LaPointe and Hermansson 2002/ in a previous DFN modelling study of the site.

The datasets used to develop the DFN models were:

- Inflow Study /Hellä et al. 2006/.
- Olkiluoto bedrock model /Vaittinen et al. 2003/.
- Compilation of 2 m packer test data /Hämäläinen 1997abcde, 2003abc, 2004ab, 2005, 2006ab/.
- LaPointe and Hermansson DFN model /LaPointe and Hermansson 2002/.

The data used are discussed in more detail below.

2.1.1   Inflow study

A compilation of measured inflow data from borehole intervals between approximately 300 and 750 m depth below ground level in the planned repository volume was developed by Pöyry Environment as part of a study to determine the expected frequency and magnitude of inflows to deposition drifts. A spreadsheet (InflowPoints.xls) containing this dataset was provided by Pöyry Environment. The "detection limit" for inflow points was estimated to be 10^{-9} m^2/s (Hellä et al. op cit). It is believed that all inflows with transmissivities greater than the detection limit are included in the spreadsheet. Lower transmissivity features can, in favourable circumstances, also be detected and about 40% of inflows in the spreadsheet are below the detection limit. The borehole intervals used in the Inflow Study are listed in Table 2-1.

2.1.2   Borehole survey data

The borehole survey data from the boreholes listed in Table 2-1 were provided as text files by Pöyry Environment. Within the Inflow Study only selected intervals were considered. These intervals were those within the depth zone of interest excluding intervals associated with MFZs with a margin zone of 20 m. Within this study the borehole intervals are called KRXX.y where y is the interval number along the borehole. For example KR01.1 is used to identify the top interval in borehole KR01 that is within the study limits and was not associated with an MFZ.

Table 2-1. Borehole intervals used in Inflow Survey /Hellä et al. 2006/.

Borehole	Azimuth	Inclination	End depth (m.a.s.l.)	Survey depth range	
				Start depth (mah)	End depth (mah)
KR01	341	75	–889.29	325	750
KR02	359	76	–961.2	325	750
KR03	306	68	–434.9	325	502
KR04	0	77	–847.37	325	750
KR05	340	65	–474.28	350	558.85
KR07	43	70	–632.96	325	811.05
KR08	155	64	–529.4	350	600.59
KR09	360	70	–538.36	325	601.25
KR10	0	90	–602.39	300	614.4
KR11	310	70	–869.6	325	800
KR12	90	70	–749.8	325	740
KR13	285	56	–408.29	375	500.21
KR14	0	70	–458.44	325	514.1
KR15	321	89	–503.48	300	518.85
KR19	307	76	–516.22	315	544.34
KR20	290	50	–384.91	400	494.72
KR22	271	59	–389.34	350	500.47

2.1.3 Olkiluoto bedrock model

A subset of structural information from the bedrock model /Vaittinen et al. 2003/ covering the boreholes used in the Inflow Study (see Table 2-1) was provided as a spreadsheet by Pöyry Environment (Structures_v2003.xls). This spreadsheet identified the intervals of each borehole associated with LFZ and MFZ structures.

A subset of the MFZs contained in the bedrock model has been used in the DFN models. The MFZs considered were: RH9, RH19A, RH19B, RH20A, RH20B, RH20C, RH21 and RH24. Within the Inflow Study, fractures in a margin zone around each MFZ (taken as ± 20 m along the borehole) were assumed to relate to the MFZ. Within this study MFZs have been included in repository-scale geometric models (although they do not intersect deposition drifts); in the upscaling calculations presented at the end of this chapter and in the drift-scale flow models.

2.1.4 2 m packer test data compilation

Pöyry Environment provided a filtered (selection of best data) dataset of 2 m packer test results /Hämäläinen 1997abcde, 2003abc, 2004ab, 2005, 2006ab/ and this was used to calibrate models of lower transmissivity features in the background rock. Background rock intervals were identified using the structural information from the Olkiluoto bedrock model.

2.2 DFN model concept

2.2.1 Major Fracture Zones

The location of MFZs was deterministic using the positions given in the Olkiluoto bedrock model (see Figure 2-1). Within the CONNECTFLOW models the MFZs have been represented as "Transmissive Surfaces": meshes of triangular elements of fixed transmissivity. In all models MFZs have been assumed to have a transmissivity of 10^{-5} m^2/s. The representation of the MFZs did not vary between model variants.
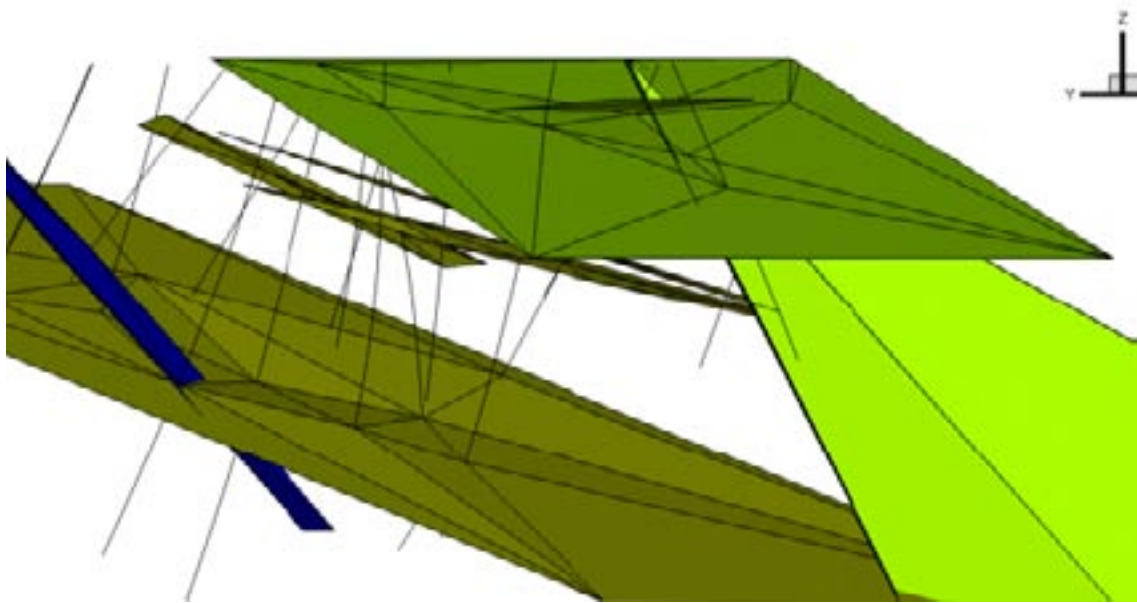
Figure 2-1. *MFZ triangular meshes as provided by Pöyry Environment. View looking northeast at approximately repository level. RH9 is steeper blue zone on left; RH24 light green feature on right. The planned repository location is below RH20 (upper green zone) and above RH21 (lower green zone).*

The MFZs have been included in the DFN repository geometry simulations for consistency and in some of the hydraulic upscaling models to understand the likely influence of such structures on effective properties. The detailed DFN flow simulation model volumes sometimes include a small portion of an MFZ near the model boundaries.

2.2.2   Local Fracture Zones

These features are extensive highly fractured or crush zones which have been identified in boreholes. Fracture zones correspond to fractured intervals with > 10 fractures/m over a minimum 2 m interval along the borehole (therefore at least 20 fractures). Crush zones correspond to intervals where the fracturing class is Ri IV or Ri V (according to Finnish engineering geological classifications see Vaittinen et al. 2003). The LFZs have therefore been identified from the fracture intersections in the boreholes. LFZs in the Olkiluoto bedrock model also include features where the hydraulic conductivity exceeds 5×10^{-7} m/s over a 2 m interval. These "hydraulic features" are typically relatively shallow and none were identified in the Inflow Study borehole intervals. Water conducting features are commonly associated with LFZs and appear to cluster around the highly fractured part of the LFZ.

Within the DFN models the LFZs were represented as non-transmissive "parent" planes around which stochastic sub-parallel transmissive fracture planes are clustered. The non-transmissive parent planes play no role in hydraulic simulations.

This concept is illustrated in Figure 2-2 where the LFZ-WCF planes are shown coloured by transmissivity. The non-transmissive parent planes are not shown. The size of the LFZs was chosen to be 500 m square with associated WCFs 50 m (1/10th length of LFZ). The 500 m LFZ size is below the size of the smallest MFZ and corresponds to the largest stochastic features used in the models of /LaPointe and Hermansson 2002/, who argued that all larger structures would be identified as deterministic features. It is likely that some of these features are in fact smaller than 500 m, but within the current study conservative values have been chosen for poorly known parameters.

The distribution of orientation of the LFZ parent planes used the sets derived from outcrop measurements analysed by /Poteri 2001/. These sets were used as input to the DFN modelling by /LaPointe and Hermansson 2002/. The density of the LFZ central planes was calibrated to
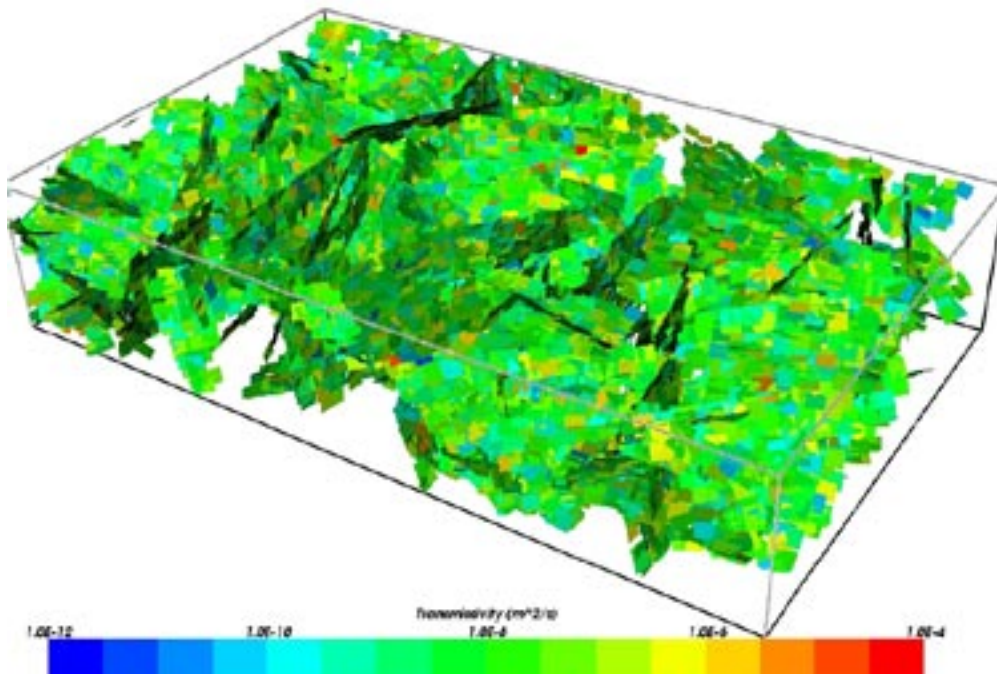
Figure 2-2. *Illustration of LFZ representation. Central planes of LFZs shown in blue, transmissive fracture planes in red.*

match the observed average spacing of 150 m in vertical and sub-vertical boreholes for the given set orientations. The calibration was performed by numerical simulation of borehole intersections over multiple realisations. The simulated borehole trajectories were taken from the survey data.

2.2.3 Water Conducting Features in the background rock

These features have been identified from flow logging with a "detection limit" of 10^{-9} m²/s and exclude those related to LFZs. In all they represent about 70% (117 out of 175) of the inflows in the Inflow Study.

The orientation distributions for these features have been taken from the work by /Poteri 2001/ using the same 3 orientation sets. The length scale distributions have been taken as Power-Law distributions with a minimum fracture size of 10 m. It was assumed that smaller fractures would not be hydraulically significant. The power-law exponents used are smaller than those derived from the analysis of outcrop and lineament data /LaPointe and Hermansson 2002/ resulting in a greater proportion of large fractures. The networks therefore include fewer but typically larger fractures than those used by LaPointe and Hermansson (op cit) and are typically better connected (fewer dead-ends and disconnected features). This is both numerically convenient (fewer fractures in the model) and conservative in terms of the effective properties of the network. The power law distributions used and the relationship to those used by LaPointe and Hermansson are discussed in Appendix C.

Different model variants have been developed using different transmissivity distributions for the features. In all, 4 model variants were defined:

- Reference Case: uniform transmissivity WCFs with transmissivity distribution from Inflow Study.

- Length Transmissivity (LT) Correlation Variant: where WCF length and transmissivity are correlated.

16

- Channel Variant: where transmissivity varies across each WCF.
- Extended Reference Case: where transmissivity is calibrated to 2 m packer test data to include lower transmissivity features.

The differences between the model variants are discussed in the next section.

The densities of the BR-WCF sets were calibrated to match either:

- The observed inflow frequency in the Inflow Study borehole intervals.
- The distribution of 2 m packer test hydraulic conductivity.

The calibration was performed by numerical simulation of borehole intersections over multiple realisations.

2.2.4   Background rock

The background rock and associated fracture network consists of the rock between WCFs, excluding LFZs, MFZs and their margin zones. The Reference Case WCFs use a transmissivity distribution derived from the Inflow Study, which extends from 10^{-10} m^2/s to 10^{-7} m^2/s, although this is likely to be censored below 10^{-9} m^2/s (estimated detection threshold of inflow surveys). Lower transmissivity WCFs are included in the Channel Variant and Extended Reference Case.

The background rock identified in boreholes includes low transmissivity fractures, low transmissivity parts of channelled WCFs and "matrix" zones. Discussions with Posiva's experts suggest that the true matrix permeability may be ~10^{-14} m/s. The background rock is not explicitly represented within the DFN models as it is assumed that flow is dominated by the WCFs.

2.3   Model variants

Geometric simulations of the system of MFZs, LFZs and WCFs are inexpensive and so can be used to investigate the effect of different concepts for the network of WCFs in the repository volume. The model variants considered are listed in the table below. The flow simulations described later in this report used only the Extended Reference Case.

The model variants differed only in their treatment of the WCFs. The treatment of MFZs and LFZs was identical in all variants (although different pseudo-random number sequences were used to generate stochastic realisations for each variant).

The Reference Case variant uses a log-normal transmissivity distribution for BR-WCFs, is centred on about 2×10^{-9} m^2/s and containing only a few features below 5×10^{-10} m^2/s. This distribution is obtained directly from the transmissivity of detected inflow points not associated with LFZs or MFZs as given in the Inflow Study /Hellä et al. 2006/.

The Extended Reference Case variant uses a BR-WCF transmissivity distribution that extends to below 10^{-12} m^2/s, although it is probable that data is only reliable to a transmissivity of 10^{-10} m^2/s (equivalent to a hydraulic conductivity of 5 10^{-11} m/s over a 2 m interval). The distribution and increased density of features has been determined by calibration of fracture intersection simulations to the compilation of 2 m packer data /Hämäläinen 1997abcde, 2003abc, 2004ab, 2005, 2006ab/. The geometric and flow simulations used two versions of the variant, with transmissivity cut-offs of 10^{-10} and 10^{-11} m^2/s. The use of the lower cut-off was to check that no significant changes in output measures occurred when including additional low transmissivity features.

The Channel variant again includes lower transmissivity features and has a consequently higher density of features. It has been fitted to the observed inflow data assuming that only a fraction of the features below the 10^{-9} m^2/s detection limit will be identified.

Table 2-2. Model variants used in this study.

Concept	Reference Case – based on /Hellä et al. 2006/	Extended Reference Case	LT Correlation variant	Channel variant
Description/ motivation	Model based on input from Inflow Study.	Model based on input from Pöyry Environment study. Model extended to address lower transmissivity range.	WCF length and transmissivity are correlated.	WCFs assumed to be channelled; only a fraction of WCFs identified during flow logging.
Number of realisations	100	100	100	50
Treatment of background rock WCFs	Density based on borehole data. Orientation from outcrop mapping. Power law length distribution (see Appendix D). Transmissivity uniform across feature.	Increased density log normal distribution fitted to 2 m packer test data /from Hämäläinen 1997abcde, 2003abc, 2004ab, 2005, 2006ab/ two variants with cut-off at $T = 10^{-10}$ and $T = 10^{-11}$ m²/s.	Length and transmissivity are highly correlated. The longest WCFs are also the most transmissive. Density, size and orientation are the same as reference case. Transmissivity distribution adjusted to compensate for size-biased sampling.	Same as reference case apart from channelling. Five times as many WCFs but only 20% of WCF area greater than flow logging detection limit. WCFs split into 10×10 subplanes. Transmissivity varies across WCF.
Treatment of LFZs	Average spacing of 150 m in borehole. Orientation uses same sets as WCFs. LFZ associated WCFs cluster around LFZ plane.	As reference case	As reference case	As reference case
MFZ Treatment	Deterministic structures Transmissivity $=1\times10^{-5}$ m²/s.	As reference case	As reference case	As reference case

The LT Correlation transmissivity distribution was also fitted to the same data as the Reference Case from the Inflow Study, but was corrected for the borehole bias due to longer fractures being more transmissive and more likely to be intersected by a borehole.

The different $\log_{10}$ transmissivity distributions are shown in Figure 2-3. The distributions are specified per fracture (or sub-fracture for the Channel variant) within each variant and not by fracture area. A plot by fracture area would result in a different distribution for the LT Correlation variant.

Tables 2-3 and 2-4 give the parameters used in the DFN model variants, including the density (given as P_{32} m²/m³ two-sided macroscopic fracture area per unit volume, see /Dershowitz 1984/) and transmissivity for each variant.
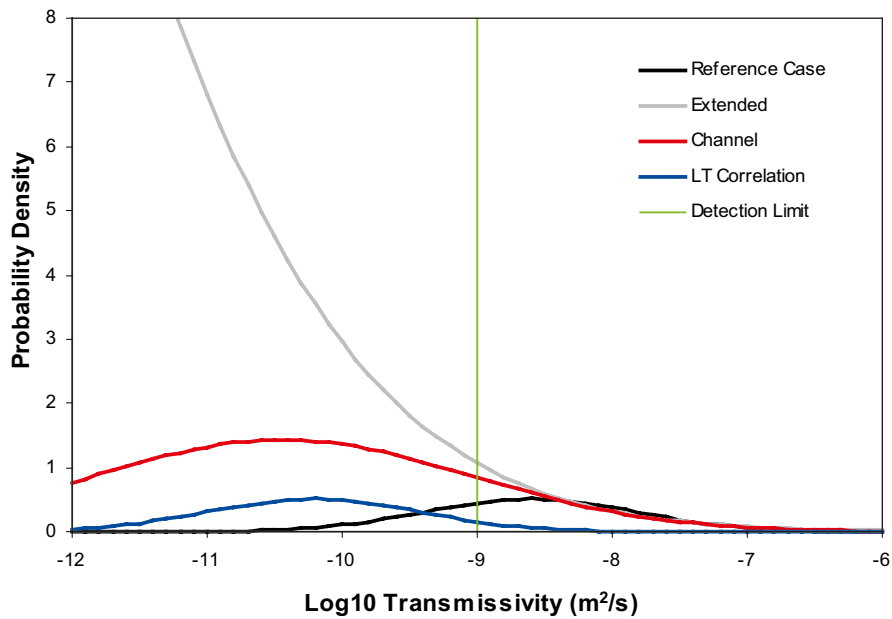
Figure 2-3. *Probability density functions for BR-WCF log transmissivity distributions from model variants. Functions scaled by relative density of fractures. In LT correlation variant the largest fractures are also the most transmissive and so more likely to intersect a borehole.*

Table 2-3. DFN model parameters for density (P_{32}) and transmissivity.

	P_{32} Set 1	P_{32} Set 2	P_{32} Set 3	P_{32} Total	Mean $log_{10}T$	Sd $log_{10}T$
MFZS		DETERMINISTIC			−5	
LFZ parent	0.0056	0.00127	0.00306	0.00993	−8.1	1.4
LFZ associated WCFs	density 2 m around parent structure			0.52	−7.9	1.0
		WCFs away from LFZs				
Reference Case	0.0276	0.0063	0.0151	0.049	−8.6	0.8
Reference Case Extended	0.476	0.108	0.256	0.840	−15.0*	2.3
Channel model variant	0.138	0.0315	0.0755	0.245	−10.4	$1.4 = \sqrt{(1.0^2+1.0^2)}$**
LT correlation model variant	0.0276	0.0063	0.0151	0.049	−10.2	0.8

* Truncated log-normal distribution used with 10^{-12} m^2/s as lower cut-off.

** Log transmissivity variance split equally between features and within features.

Table 2-4. Orientation, relative density and length scale of fracture sets in DFN model variants. Three set definition derived from outcrop analysis by /Poteri 2001/.

| | WCFs and LFZ central parent planes* | | | LFZ-WCFs |
	Set 1	Set 2	Set 3	
Dip direction	150	257	330	Normally distributed around central plane σ = 10
Dip	20	88	73	Normally distributed around central plane σ = 10
Fisher k value	6.9	16	2	Not applicable
Relative density	56%	13%	31%	Single set sub-parallel to parent plane.
Power law length scale exponent	2.5	2.72	2.66	Fixed size 50 m square

* LFZ central parent planes use only the orientation distributions and set definitions.

2.4　Model verification and confidence building

2.4.1　Intersection statistics

In order to check that the model parameterisation and calibration has been adequately performed, intersection statistics for the intervals used in the Inflow Study were simulated for multiple realisations. The frequency and transmissivity distribution of intersections was calculated for each model variant and a comparison with the data is given in Table 2-5.

The transmissivity distributions of the simulated intersections are shown in Figure 2-5. Again, it can be seen that the model variants are well calibrated to the distribution of transmissivity above the detection limit of the flow logging (10^{-9} m²/s). Differences arise in the frequency of lower transmissivity intersections in the variants that include additional low transmissivity features (Channel and Extended Reference Case). The vertical axes of the plots are scaled to match the appropriate number of realisations (one realisation in the case of the measured data).

The comparison shown in Figure 2-5 is over many realisations and shows a good match between measurement and the average behaviour of the DFN model variants over multiple realisations.

Table 2-5. Comparison of intersection statistics from Inflow Study and simulated results for the four model variants.

	Inflow Study	Reference Case	Extended	Channelling	LT Correlation
Realisations	1	100	20	100	100
MFZs		All models use geometry from bedrock model.			
LFZs	31 structures 57 inflows	All models use same geometry/parameters. Structures mean 30.1 (31 over 50 realisations). Inflows mean 56 (57.5 over 50 realisations).			
Connected WCF $Log_{10}T > -10$	118 inflows	112	317	124	111
Connected WCF $Log_{10}T > -9$	77 inflows	83	90	69	90
Mean inflow spacing	20 m σ = 40	22 m σ = 27	11 m σ = 13	22 m σ = 27	21 σ = 24
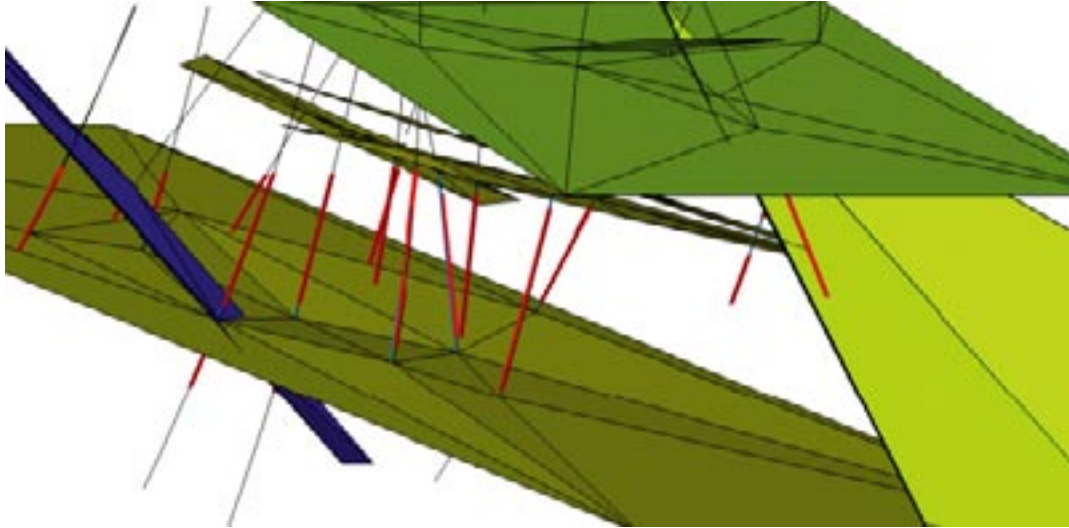
Figure 2-4. *Borehole intervals used in Inflow Study. Red intervals indicate the zones away from MFZ intersection over which statistics were calculated. Colour coding of the other structures corresponding to Figure 2-1.*
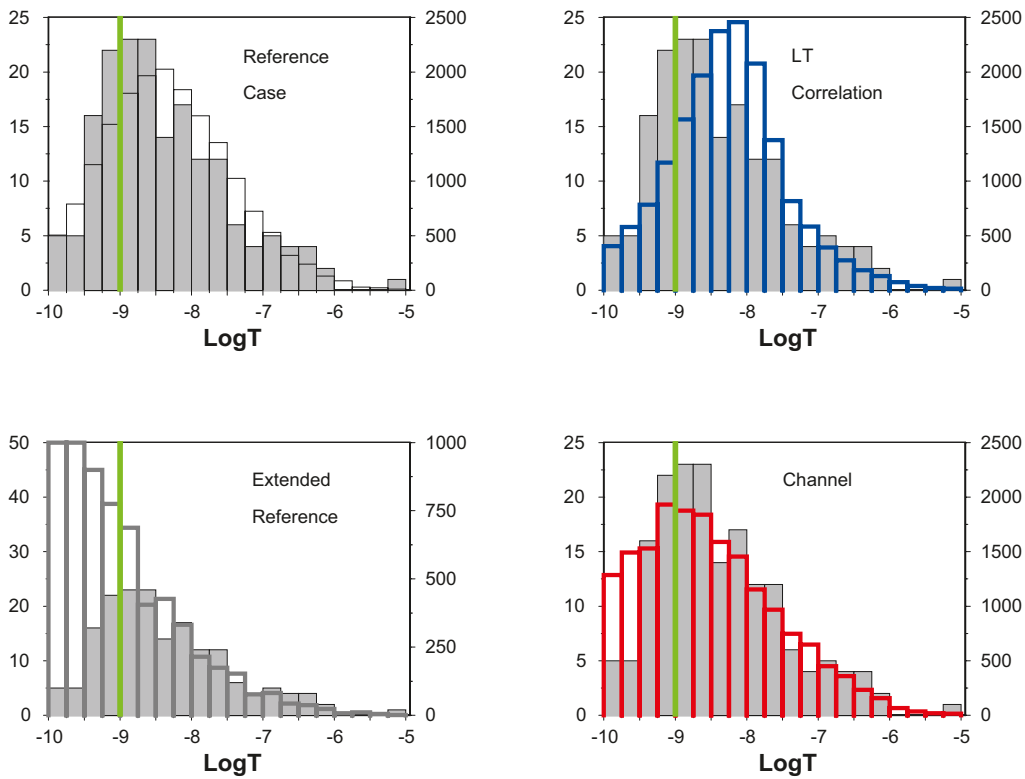
Figure 2-5. *Comparison of simulated and measured intersection transmissivity distribution for the model variants. Data shown in grey, inflow logging detection limit shown in green.*

It is also useful to look at realisation dependence and frequency of intersections for individual boreholes. Table 2-6 presents the measured and simulated intersection counts for each borehole section. The simulated counts are summarised as minimum, maximum and median over 100 realisations of the Reference Case. There are considerable variations between realisations. The boreholes whose measured intersection count is outside the range of the simulations have been shaded in grey. In two sections the density is higher than expected: KR03.1 and KR08.1, while in KR02.2, KR07.1, KR07.2 and KR19.2 the count is lower than expected.

Table 2-6. Comparison of measured and simulated borehole intersections (Reference Case).

		KR01.1	KR02.1	KR02.2	KR03.1	KR04.1	KR04.2	KR05.1
Measured		17	10	1	30	0	4	6
Simulated 100 realisation	Min	4	2	1	1	1	5	5
	Max	30	26	20	12	3	34	12
	Med	13	11	5	4	1	17	4

		KR07.1	KR07.2	KR08.1	KR09.1	KR09.2	KR10.1	KR10.2
Measured		3	0	16	1	3	1	14
Simulated 100 realisation	Min	5	1	1	1	1	1	4
	Max	28	16	14	15	20	3	23
	Med	16	3	6	4	4	1	11

		KR11.1	KR11.2	KR12.1	KR12.2	KR13.1	KR14.1	KR15.1
Measured		16	0	9	9	8	7	6
Simulated 100 realisation	Min	3	1	4	1	1	2	3
	Max	24	15	26	8	15	19	21
	Med	13	6	11	2	5	8	10

		KR19.1	KR19.2	KR20.1	KR22.1	KR22.2
Measured		10	1	2	0	0
Simulated 100 realisation	Min	1	1	1	1	1
	Max	15	15	11	4	7
	Med	6	3	2	1	2

KR08 is almost parallel to RH24 and may be within its "damage" zone. In KR03 the majority of the inflows are in the upper section where there is also a fracture zone R72. Hydraulic fractures appear to be less dense in KR04, KR07 and KR11.2 in the central block (perhaps due to an over-estimate of hydraulic fracture density due to inclusion of the high inflow density zones in KR03 and KR08).

There is a good match between the data and the simulations showing that the model variants have been well calibrated to average behaviour. Note that the comparison has been made with all data from the Inflow Study and not just the data from KR01.1 which in fact has a slightly higher than average density of WCFs (see Table 2-6).

2.4.2 Simulated borehole test

In order to develop further confidence in the model variants a steady state flow test was simulated to check that the computed inflows were consistent with the data from the Inflow Study. The upper interval in KR01 (from 325.0 to 590.3) was selected and is shown in Figure 2-6. The model region for flow simulation was a cylinder of 50 m radius centred on the borehole interval (shown in light blue). The outer surfaces of the cylinder were treated as constant head boundaries and a 50 m drawdown was applied to the borehole interval. Sample realisations of the model volume are shown in Figure 2-7.

The computed inflows were converted to transmissivity using the method and assumptions specified in the Inflow Study, and histograms of the data (from all intervals) and simulations are shown in Figure 2-8. The scale of vertical axes for the simulations and data has been chosen to account for the length of the KR01.1 interval versus the total interval length considered within the Inflow Study and the number of realisations.
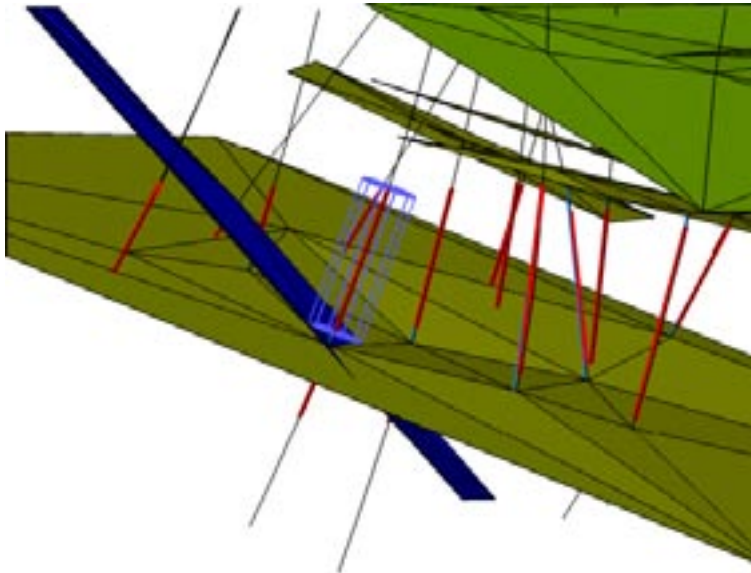
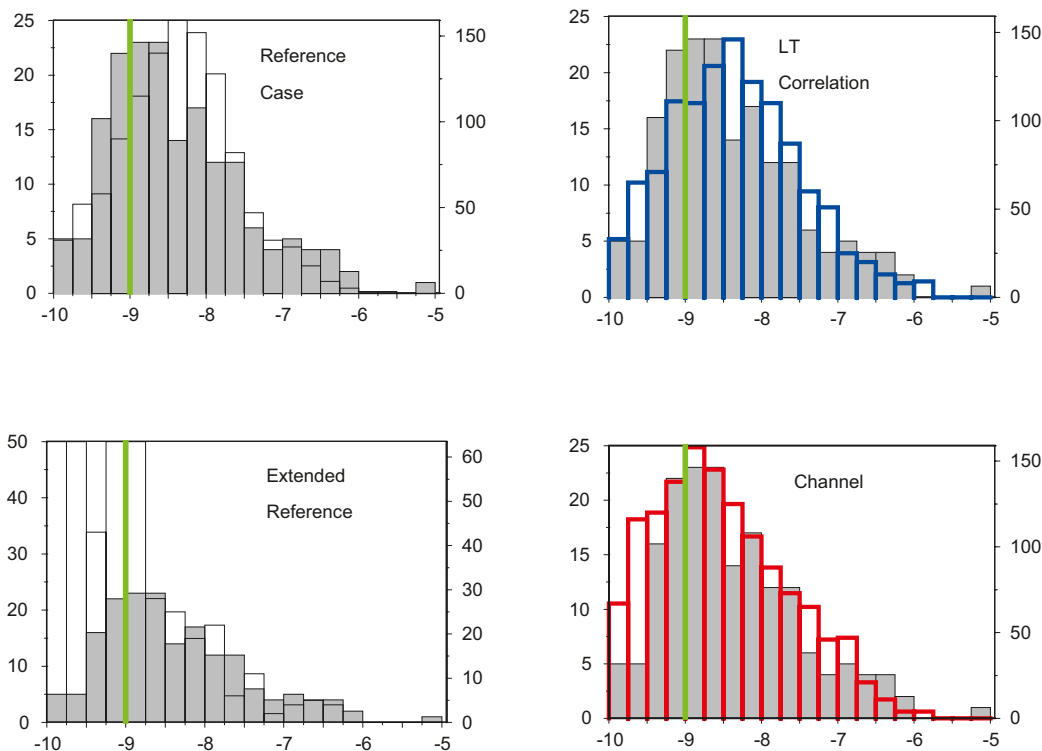**Figure 2-6.** *Interval KR01.1 used for flow simulations consistency checks. Colour coding of the other structures corresponing to Figure 2-1.*
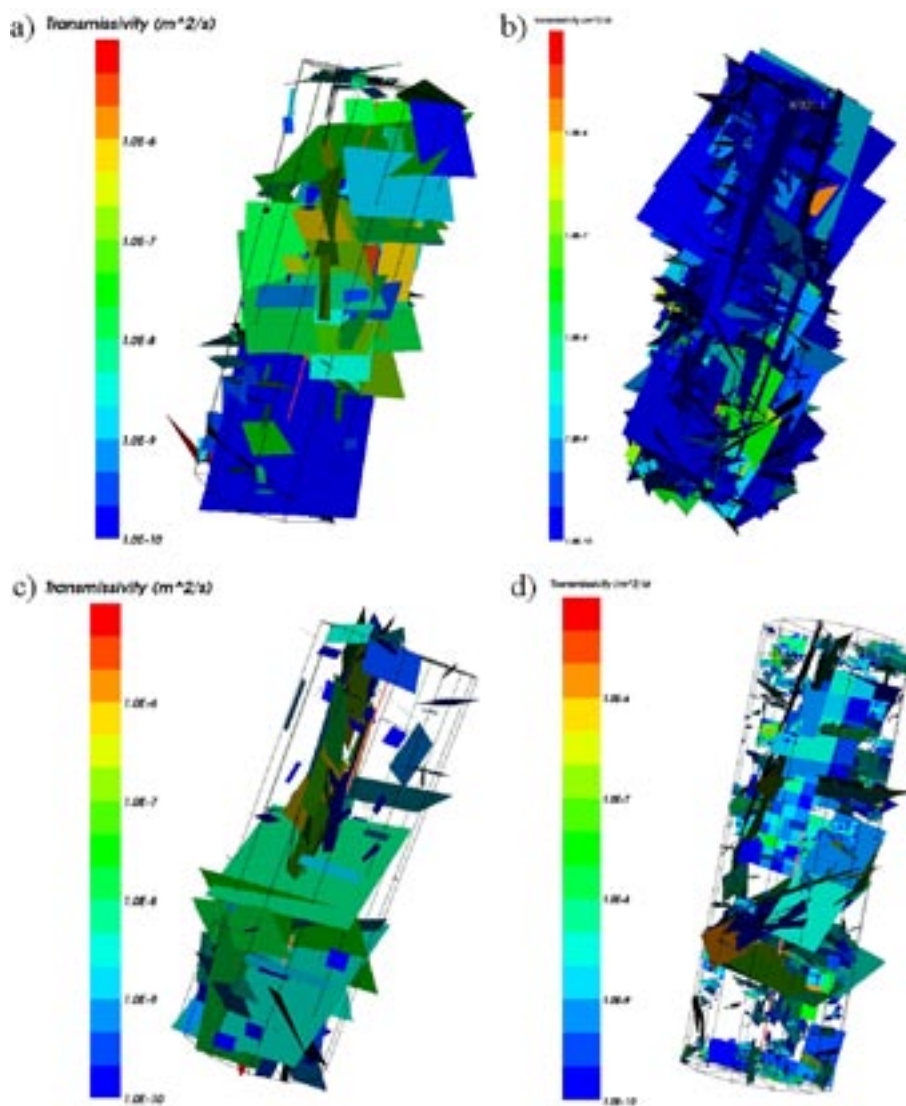
Figure 2-7. *Sample realisations of KR01.1 flow simulation model region (50 m radius cylinder): a) Reference Case, b) Extended; c) LT Correlation; d) Channel.*

Figure 2-8. *Comparison of simulated flowing and measured* log_{10} *transmissivity distribution for the model variants. Data shown as solid grey columns, model fits as hollow columns.*

2.5 Effective conductivity of the fault and fracture system

In order to determine the consistency of the DFN model variants with continuum site-scale models developed by VTT for Posiva /Posiva 2005/, the effective hydraulic conductivity of the fault and fracture network was calculated. The upscaling method implemented within CONNECTFLOW fits a permeability tensor to the flux through a cube for gradients in a variety of directions. The flux can be calculated on the cube surfaces where the pressure boundary conditions are applied or on internal surfaces called a "shrink zone" (see Figure 2-9). A least-squares fit to the permeability tensor is made using the fluxes calculated for multiple gradient directions.

The upscaling method was applied to 10 realisations of a 2,500×1,500 m block between –300 to –800 m around the planned repository location. Simulations were made for the Reference Case and LT Correlation variants. This volume contained MFZ features, which were treated as surfaces of constant transmissivity 10^{-5} m²/s. Figure 2-10 shows the up-scaled DFN volume as coloured cubes of either 100 or 250 m side-length. The locations of the MFZs are clearly seen in the blocks of high maximum (k_1) and intermediate (k_2) permeability in red.

Histograms of the principal components (k_1 maximum, k_2 intermediate and k_3 minimum) and anisotropy ratio (k_1/k_3) of the effective permeability tensor are shown in Figure 2-11 and statistics for the effective hydraulic conductivity at 100 and 250 m scale have been compiled for cubes with and without MFZs in Table 2-7. For comparison with the VTT model parameters /Posiva 2005/ the permeability was converted to hydraulic conductivity, assuming a water density of 1,000 kg/m³, viscosity of 1×10^{-3} Pa·s and gravitational constant of 9.81 m²/s.

The hydraulic conductivity used in calibrated site-scale groundwater flow models from VTT /Posiva 2005/ is given in Table 2-8. The porous medium models assume isotropic conductivity and the hydrologic "units" cover a slightly different depth range. Typically, the up-scaled DFN values are intermediate between the initial (Case 1) values and the calibrated (Case 3) values. The DFN models have assumed extensive uniform transmissivity features with a greater proportion of longer fractures than indicated by the site data and so are expected to be conservative in terms of the larger scale effective hydraulic conductivity.
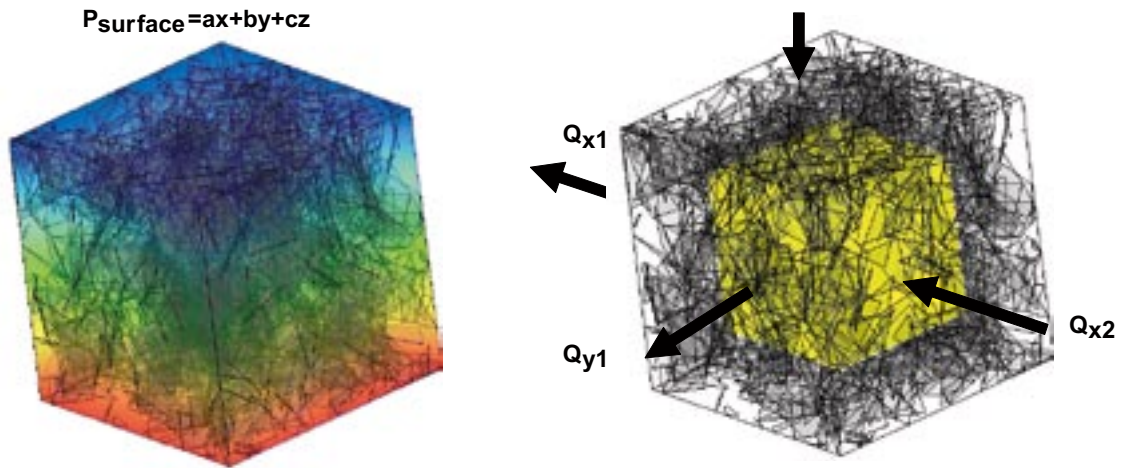
Figure 2-9. *Linear pressure boundary conditions are applied to a cube surface and the flux calculated on the surface or internal surface. Yellow cube on right figure.*
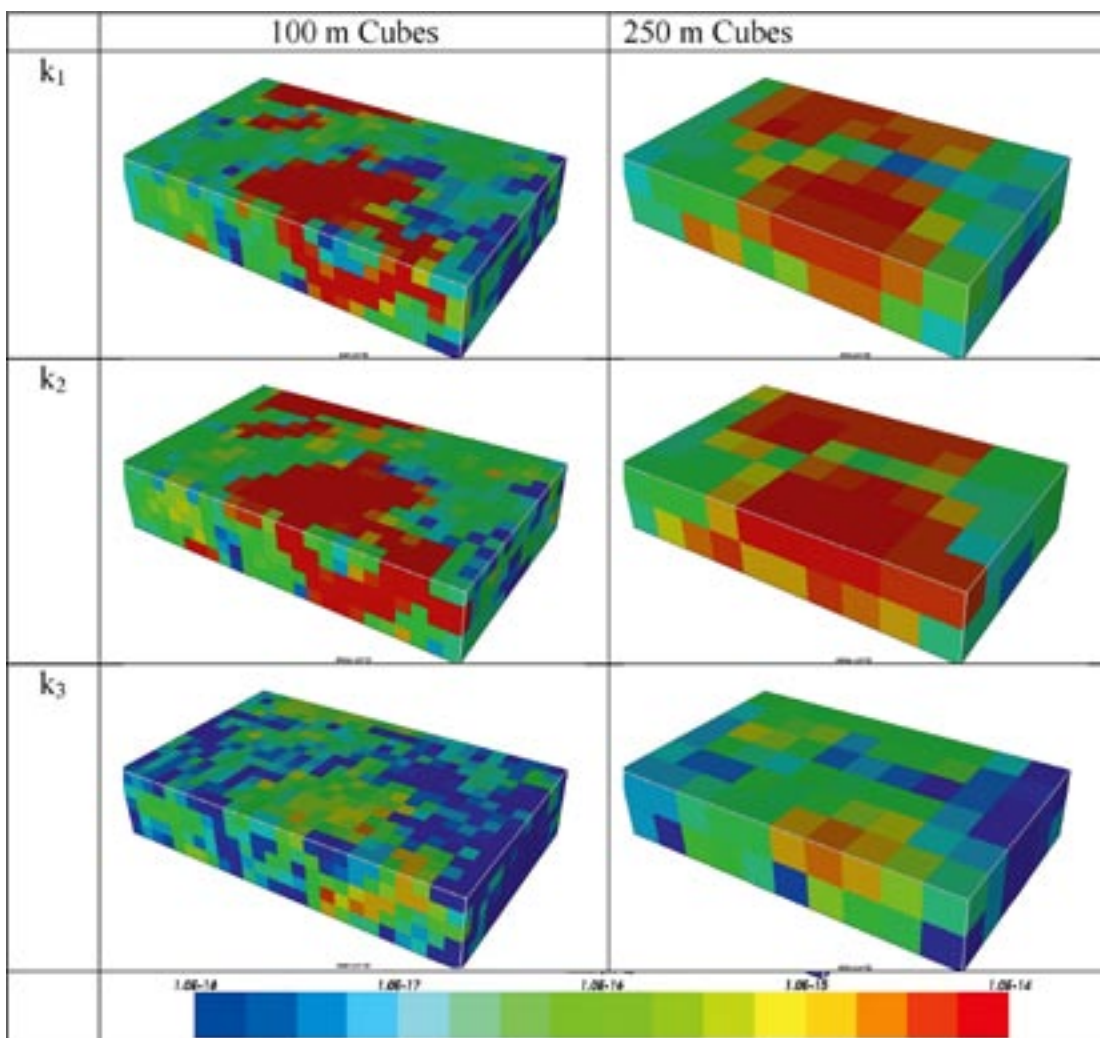
Figure 2-10. *Effective permeability of a DFN model realisation from the Reference Case, up-scaled to 100 m and 250 m cubes. Cubes coloured using a log scale with blue 10^{-18} m^2 and red 10^{-14} m^2.*
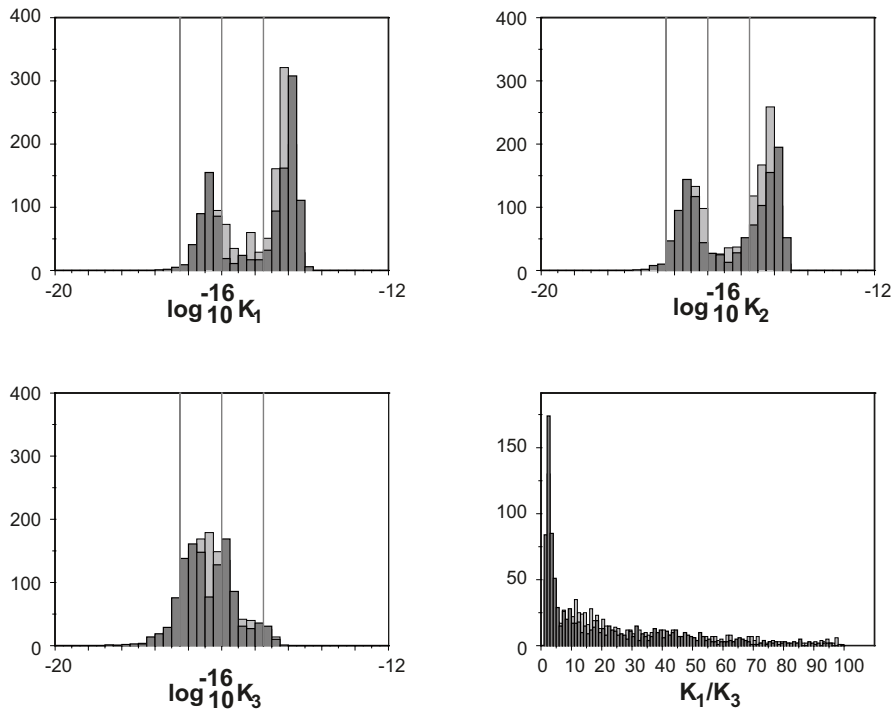
Figure 2-11. *Histograms of principal components of effective permeability tensor (m^2). Vertical lines show $k = 1 \times 10^{-17}$, 1×10^{-16} and 1×10^{-15} m/s.*

Table 2-7. Mean and standard deviation of effective principal components of $\log_{10}$ hydraulic conductivity (m/s) tensor for 100 and 250 m cubes.

Model	Block type	Cube side-length (m)	$\text{Log}_{10}\,K_1$	$\text{Log}_{10}\,K_2$	$\text{Log}_{10}\,K_3$
Reference	MFZ	250	−7.8 (1.8)	−8.2 (1.8)	−9.3 (1.6)
Reference	No MFZ	250	−9.3 (0.3)	−9.5 (0.3)	−9.8 (0.3)
Reference	No MFZ	100	−9.3 (0.5)	−9.6 (0.5)	−10.2 (0.7)
T-L correlation	No MFZ	250	−9.2 (0.2)	−9.4 (0.2)	−10.7 (0.3)

Table 2-8. Comparison of effective hydraulic conductivity (m/s) from calibrated porous medium models with values from up-scaled DFN models.

| Depth	Case 1 Initial (m/s)	Case 3 Calibrated (m/s)	DFN Model Up-scaled Effective Hydraulic Conductivity
0–50	1×10^{-7}	1×10^{-7} (xy) 1×10^{-9} (z)	Not relevant to this depth range
50–100	5×10^{-8}	5×10^{-10}	
100–200	3×10^{-9}	3×10^{-11}	
200–400	1×10^{-9}	1×10^{-11}	300–750 m
400–2,000	3×10^{-10}	3×10^{-12}	$K_1 \sim 5 \times 10^{-10}$ m/s, $K_3 \sim 1 \times 10^{-10}$ m/s

3 Geometric simulations

All geometric calculations were performed on a 2,400×1,600×100 m block at 400 m depth as shown in Figure 3-1, corresponding to one of the repository layouts identified in WR2002-57 /Johansson et al. 2002/. The generation region for the fracture network model was much larger to avoid edge-effects. The repository panel and tunnel numbering scheme used in this study are also shown in Figure 3-1.

Realisations of the different networks are shown in Figures 3-2 and 3-3. The number of WCFs in a realisation range from about 20,000 for the Reference Case to 110,000 for the extended reference case with a cut-off at 10^{-11} m^2/s. In the Channel Model there are approximately 30,000 WCFs but each WCF is represented by up to 100 sub-fractures resulting in over 1,500,000 sub-fractures.

3.1 Inflow classes

The repository layout adaptation scheme uses both geological and hydrogeological criteria to determine the layout of the repository. Within deposition drifts the major focus is on the level of groundwater inflow to the open drift. The adaptation scheme includes a set of inflow classes which are used to determine the layout within an individual drift. Inflow classes (related to transmissivity) for WCFs were discussed at the first review meeting (30/09/05). Following the meeting these classes were revised based on input from Posiva.
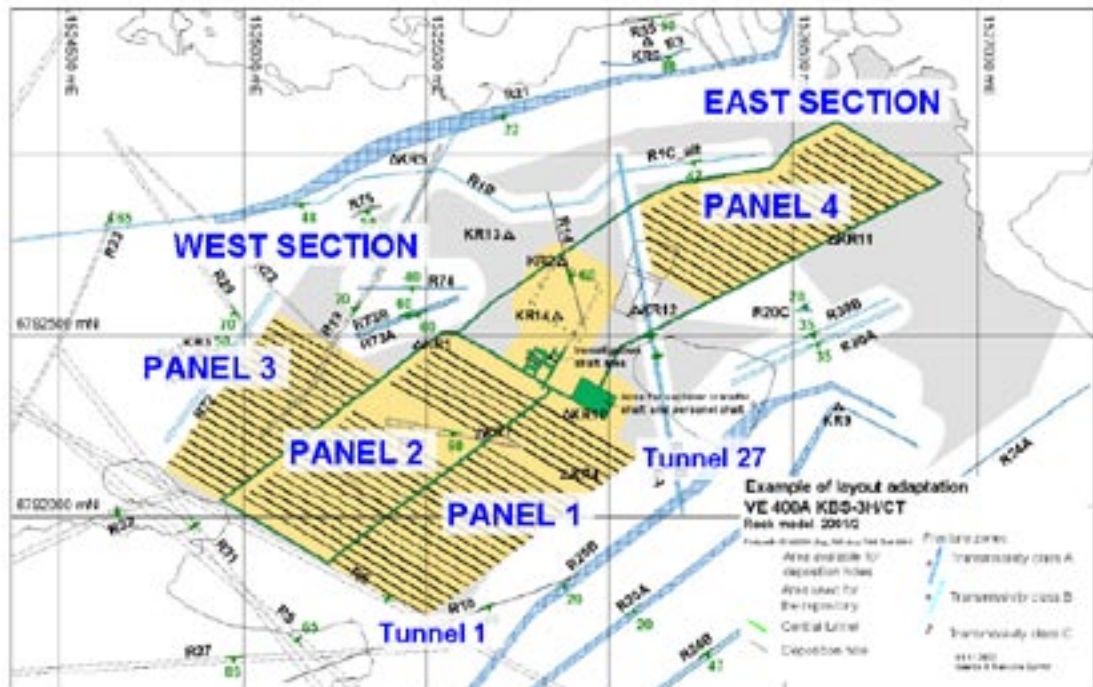
Figure 3-1. *Repository plan /from Johansson et al. 2002/ and DFN model volume (in red) used for geometric simulations. Tunnel and Panel numbering scheme used in simulations also shown in blue.*
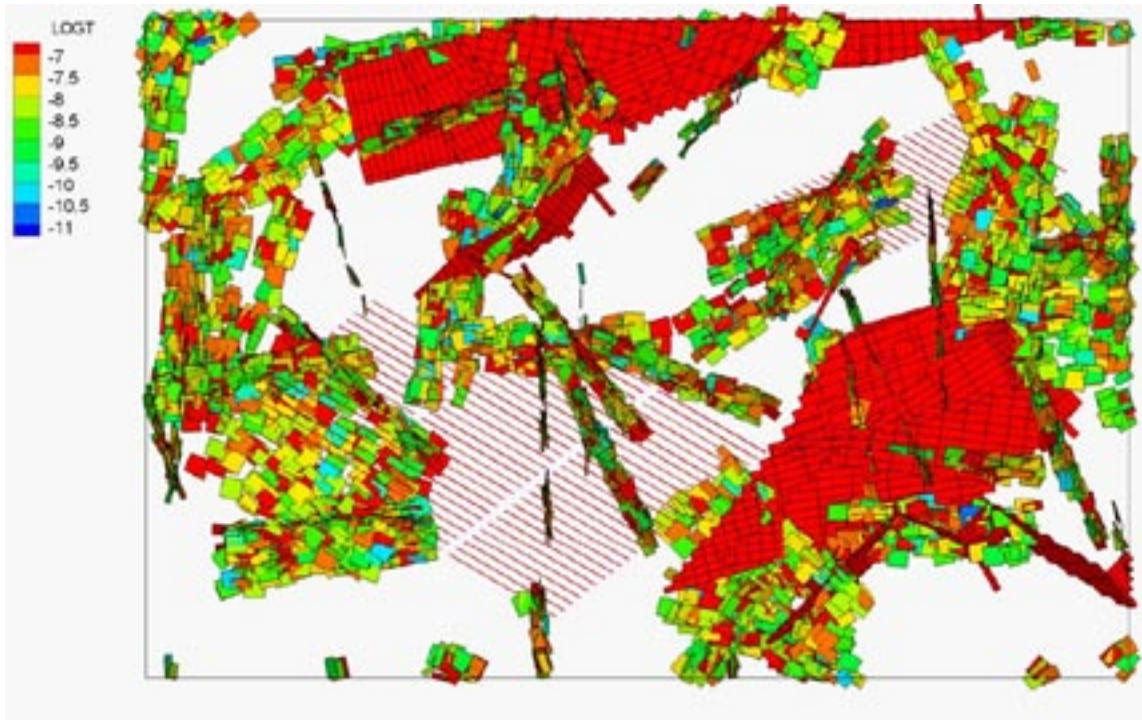
a) MFZs (red) and WCFs associated with LFZs (representation common to all models) and deposition drifts.
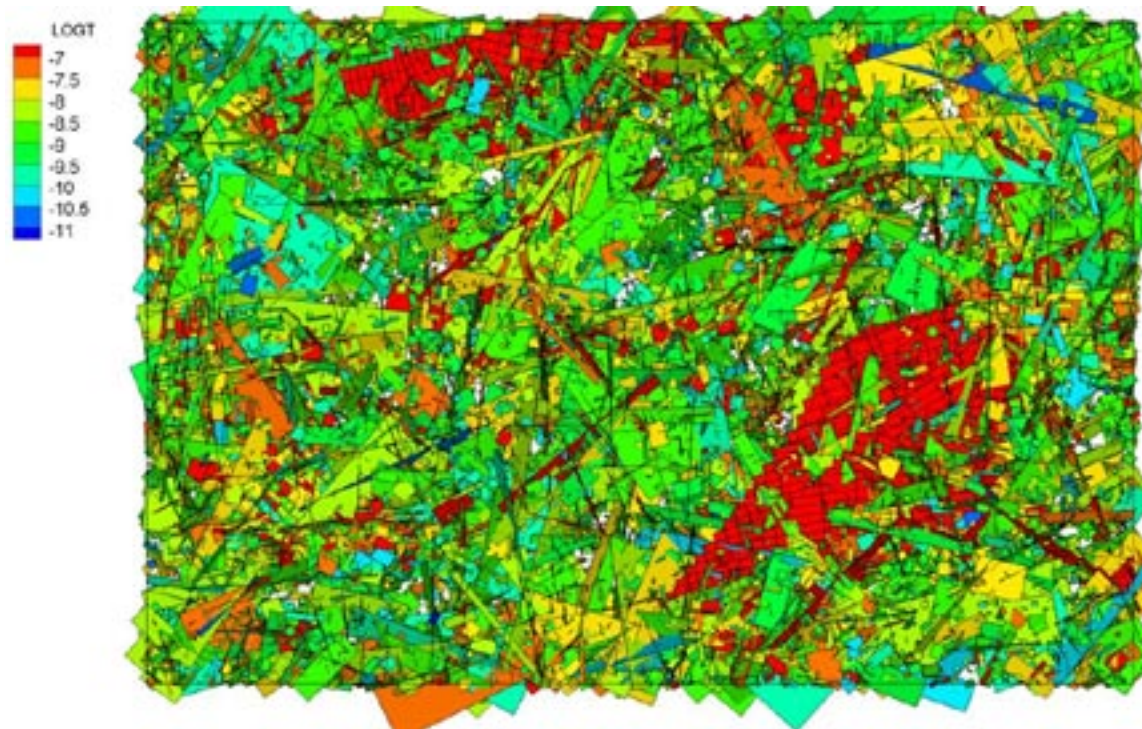
b) Reference case DFN model realisation. WCFs coloured by $\log_{10}$ transmissivity (m²/s).

Figure 3-2. *Plan views of realisations of the different DFN model variants.*
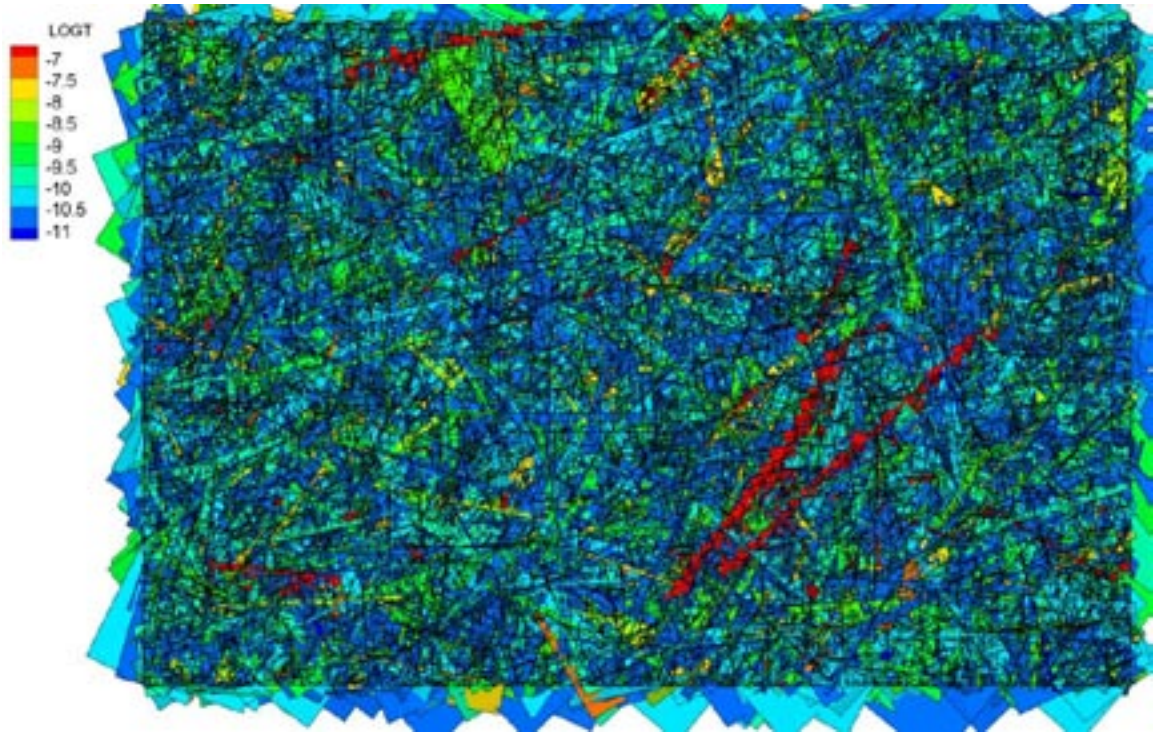
c) Extended Reference (cut-off T = 1.0×10^{-11} m^2/s) DFN model realisation. WCFs coloured by log$_{10}$ transmissivity (m^2/s).
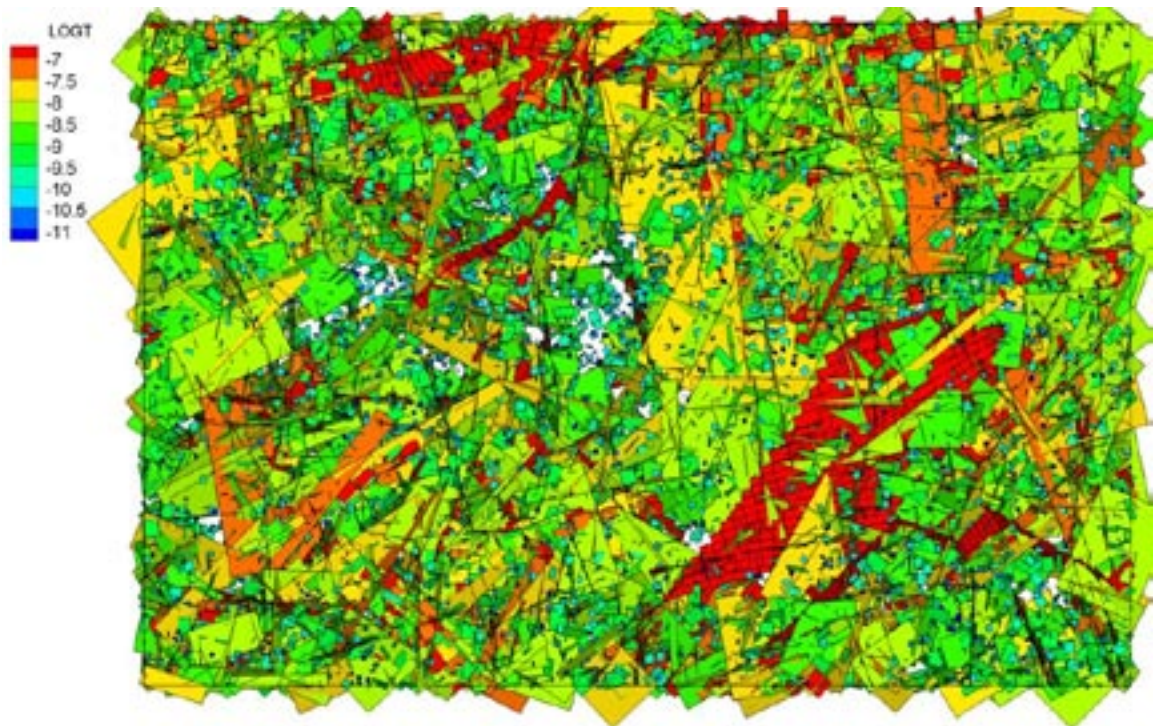
d) LT Correlation variant realisation. WCFs coloured by log$_{10}$ transmissivity (m^2/s).

Figure 3-2. *Continued.*
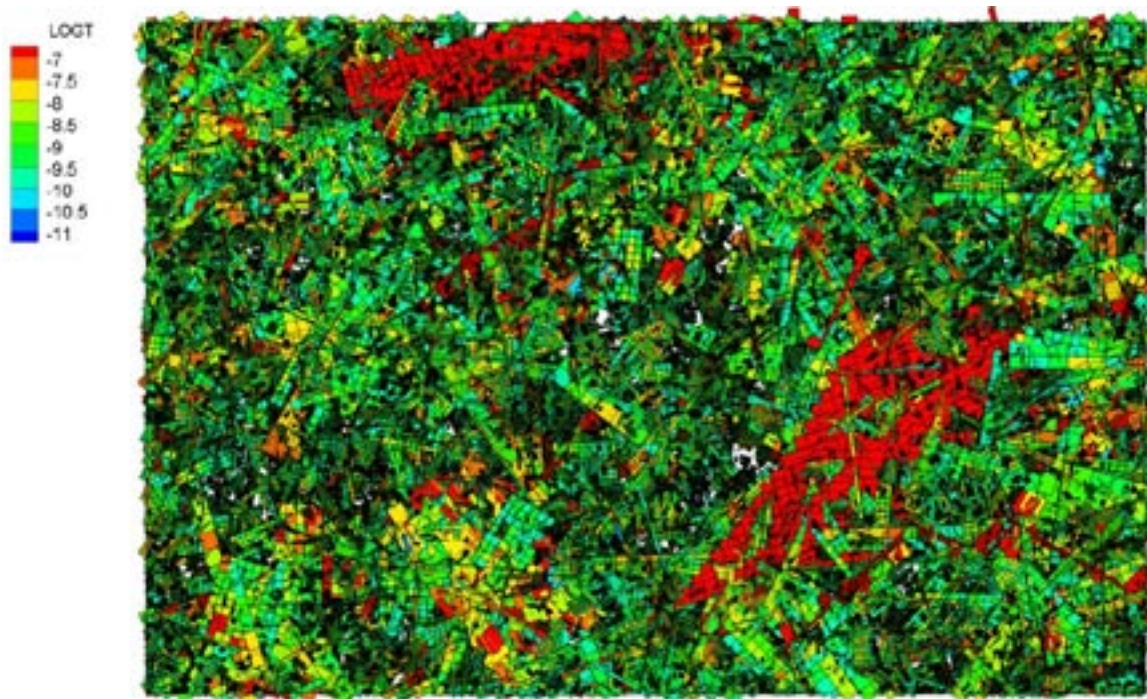
e) Channel variant realisation. WCFs coloured by $\log_{10}$ transmissivity (m²/s).

Figure 3-2. *Continued.*
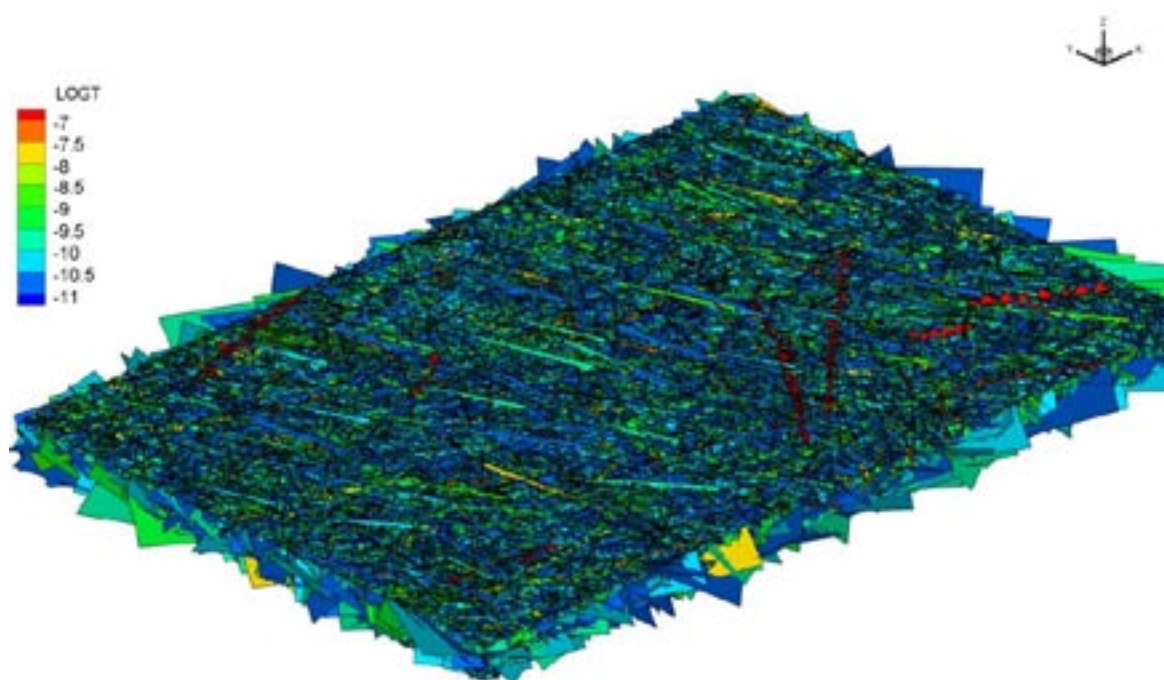
Figure 3-3. *Oblique view of realisation of repository block for the Extended Reference DFN model. MFZs visible as red (high transmissivity features).*

In cases where large inflows are grouted it is assumed that they would also be subsequently isolated by plugs. In certain occasions it is optional to use structural seals to reduce significant inflows. Post grouting flow may be used as input to decision for abandoning a drift.

Within the geometric models the average (along trace) local WCF transmissivity where it intersects the drift wall has been used to identify the inflow class using the transmissivity values given in the table above.

In reality inflows into the drift will be more complex because:

- Interaction with other excavation may reduce inflow on high transmissivity features.
- Inflow may be locally highly channelled.
- Flow may be diverted into EDZ fractures or local small scale fractures away from larger structures.
- Formation of skin zone (e.g. two-phase flow, mechanical effects).

It may therefore be easier to identify such features in the field on the basis of probe holes rather than inflow to the drift itself. However, the inflow rate after excavation in to the open tunnel seems to be significant to the function of buffer components and may therefore define the limits. After the drift is filled, the pressure increase rate becomes one key parameter.

Table 3-1. Inflow classes.

Inflow Q* (l/min)	Transmissivity T** (m²/s)*	Hydraulic aperture e*** (µm)	Compartment/ Isolated	Treatment of inflow in deposition drift
$Q < 0.004$	$T < 1.0 \times 10^{-10}$	$e < 5$	Super-container Compartment	Tight section where gas build-up possible
$0.004 \leq Q < 0.1$	$1.0 \times 10^{-10} \leq T < 2.65 \times 10^{-9}$	$5 \leq e < 15$	Super-container Compartment	Acceptable
$0.1 \leq Q < 1$	$2.65 \times 10^{-9} \leq T < 2.65 \times 10^{-8}$	$15 \leq e < 32$	Compartment or isolation (in compartment but no super-container, only filling)	Sealing by using extra fine low pH grout. Limit for sealing by cementitious grout is likely at the level of 1.0×10^{-8} (the same limit is probably also applicable for non-cementitious grout; /Ahokas et al. 2006/).
$1 \leq Q < 10$	$2.65 \times 10^{-8} \leq T < 2.65 \times 10^{-7}$	$32 \leq e < 69$	Isolated	Defines compartment – inflow reduced by grouting or optional structural sealing.
$10 \leq Q < 30$	$2.65 \times 10^{-7} \leq T$	$69 \leq e$	Isolated	As above, optional structural sealing, abandon drift if flow after sealing above 30/min. (Note: 30 l/min is a first estimate and may be revised in the future).

* Assuming one inflowing fracture.

** Into one super-container section from fractures without sealing.

*** Hydraulic apertures have been calculated assuming a water density ρ of 1,000 kg/m³ and viscosity μ of 1×10^{-3} Pa·s using the cubic law

$$T = \frac{\rho g e^3}{12\mu} \qquad (1)$$

where T is the transmissivity in m²/s and e the hydraulic aperture in m.

3.2   Repository layout and adaptation

The terminology used within this study is illustrated in Figure 3-4 which also gives the values for transmissivity thresholds (based on the inflow classes) used to make the layout adaptation.

Deposition drifts

Drifts are assumed to be 300 m in length, 1.85 m diameter at 25 m spacing located at 400 m depth and laid out according to /Johansson et al. 2002/ for the variant without side tunnels. In this report, drift lengths vary (and some drifts are not excavated) according to intersection with various R zones (local fracture zones) predicted to lie at the 400 m horizon (see Figure 3-1). In the simulations all drifts are 300 m in length (for simplicity of statistical measures) and drift utilisation is controlled by the intersection with stochastic features (LFZs and WCFs). The drifts avoid the MFZs.

Compartment plug (or seal zones)

Compartment plugs are used to isolate higher transmissivity WCF intersections from the compartments where the super-containers will be emplaced. Compartment plugs are shown outlined in red in the simulated drift maps. In addition to the compartment plugs a seal will be placed at the start of each drift after emplacement – these drift end plugs are not shown.

Compartment plugs are set around WCF intersections where the average transmissivity is greater than 2.65×10^{-8} m^2/s. Where multiple high transmissivity features overlap the compartment plug extends around the overlapping traces. The ends of the plug are positioned at the end of the high transmissivity traces and extend beyond them (or to the end of the tunnel). Where the compartment that would be formed between two compartment plugs is smaller than the minimum size required for a compartment the compartment plug is extended to form a single compartment plug.

Drift compartments

Compartments are the sections of the drifts where super-containers will be emplaced.

Super-container locations

Super-containers are of length 5.56 m located within the compartments separated by distance blocks of length 5.35 m. A distance block is located at the start of each compartment and after every "blank zone".

Compartment blank zones

A "blank zone" is an interval within a compartment which contains WCFs of transmissivity greater than 2.65×10^{-9} m^2/s. Super-containers will not be emplaced in such zones and the drift will be filled with a permeable fill. The limit chosen of 2.65×10^{-9} m^2/s corresponds to an inflow of 0.1 l/min (see Table 3-1) which is considered a possible limit for piping in the buffer.

Compartment dry zones

A "dry zone" is an interval within a compartment which does not intersect any WCF of transmissivity greater than 10^{-10} m^2/s and is of length greater than 10.91 m (length of super-container plus distance block). The reason for identifying dry zones is that these may be the locations where free gas may become trapped. Dry zones are shown outlined in blue in the simulated drift maps.

A visualisation from one realisation of a single panel is shown in Figure 3-5.
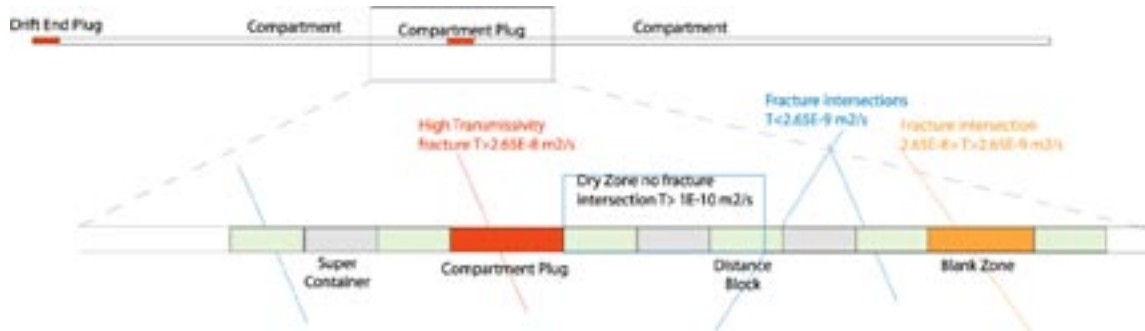
Figure 3-4. *Layout showing terminology used in layout adaptation within this study.*
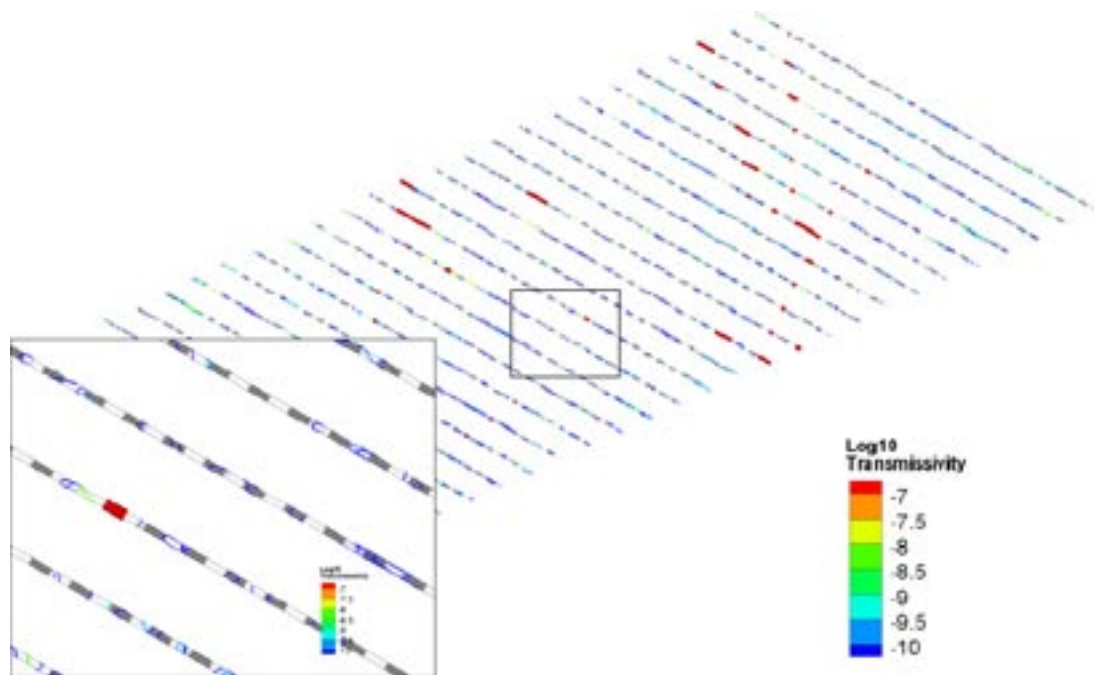
Figure 3-5. *Detail for sample realisation of Reference Extended model showing compartment plugs (red) and container positions (dark grey). WCF traces are also shown coloured by transmissivity and can be seen most clearly in the detail shown in bottom left of figure.*

Detailed flow simulations at the drift scale are presented later in the report. Within the geometric simulations inflows have been estimated to allow comparison with the flow simulations and current plans. Inflow estimates are calculated from the Thiem equation for steady state radial flow:

$$Q = \frac{2\pi T \Delta h}{\ln\left(r_{BC} / r_T \right)} \tag{2}$$

for each WCF with a head change Δh of 400 m from constant head hydrostatic boundary at 50 m radius (r_{BC}) from the tunnel (radius r_T 0.925 m).

This takes no account of:

- The angle at which the WCF intersects the drift.
- Whether the WCF is fully cut by the drift. Where WCFs do not fully cut the drift, inflow will be restricted, but no account is taken of this in the geometric calculations.
- Channelling of WCFs such that inflow is restricted close to the tunnel.

- Reduced head at 50 m due to drawdown from other tunnels, roadways, shaft etc. The method assumes that there is no drawdown due to the presence of the repository.

- Reduced head at 50 m due to the absence of any high transmissivity features able to provide sufficient water. The MFZs are typically more than 50 m from the drifts.

- Connection of the WCF to other water conducting features.

- Damage/skin effects around drift.

It is believed that the assumptions will result in an overestimate of total inflow to a drift as for all but a tiny number of intersections the effect of fracture angle is small (increase of at most 50% in calculated flow), while the other factors could result in significant reductions in flow (possibly up to an order of magnitude).

WCF grouting

Inflow estimates are provided for each WCF (and hence compartments, seals and drifts) assuming no grouting or post grouting where the average transmissivity of grouted features is assumed to have been reduced to 2×10^{-8} m²/s. This simple model of grouting performance is the same as that used in numerical modelling of the impact of ONKALO shaft /Vieno et al. 2003/. The actual grouting performance is currently uncertain and it is possible that grouting could be more widely used and results in a greater reduction in inflow.

3.3   Results

The outputs were provided as text files and spreadsheets. Spreadsheet size was limited to ~65,000 rows so in some cases outputs from a subset of the realisations were included in the spreadsheets. Summary statistics were provided for each measure in each spreadsheet: Arithmetic mean, median, standard deviation, minimum, 1, 5, 25, 75, 95, 99 percentiles and maximum of sample. All outputs were tied to model (realisation) number, tunnel number and panel number (1–4). Panels were numbered 1–4 and tunnels (emplacement drifts) are numbered from 1–27 increasing eastwards as shown in Figure 3-1. In all there were 97,300 m drifts in each realisation of the simulated repository.

Simulated trace maps

Simulated trace maps were calculated for each panel. The trace-maps show the dry sections (outlined in blue in Figure 3-6) where gas may not be able to escape and also those fractures greater than 2.65×10^{-9} m²/s (shown as red fracture traces) which could potentially deliver inflows of 0.1 l/min or more. A detail of one trace map is shown in Figure 3-6 to illustrate the colour scheme and detail available.

Histograms of selected drift measures

Histograms of the number of seals, compartments and super-containers in a drift (over all tunnels, panels and realisations) are shown in Figure 3-7. All model variants in general show similar behaviour. The only significant difference is in the length of dry sections per drift which is smaller in the models that include lower transmissivity features (between 10^{-9} and 10^{10} m²/s), as would be expected. The Reference Case and LT Correlation model variants contain WCFs with transmissivity distribution derived directly from the flow logging which has a "detection limit" of 10^{-9} m²/s (note that many of the transmissivity values in the flow logging dataset are below 10^{-9}, but it is assumed that detection below this value is not 100%). In some drifts, compartment plugs have been emplaced at the start or end of the drift, this results in the number of compartments not being a simple function of the number of seals (e.g. number of seals plus 1). Selected statistics are tabulated in Appendix A.

Figure 3-6. *Detail of trace map. Red rectangles are compartment plugs. WCF traces with transmissivity greater than 2.65×10^{-9} m^2s (blank threshold) are shown in red, all other traces are in green. Blue rectangles show dry zones.*
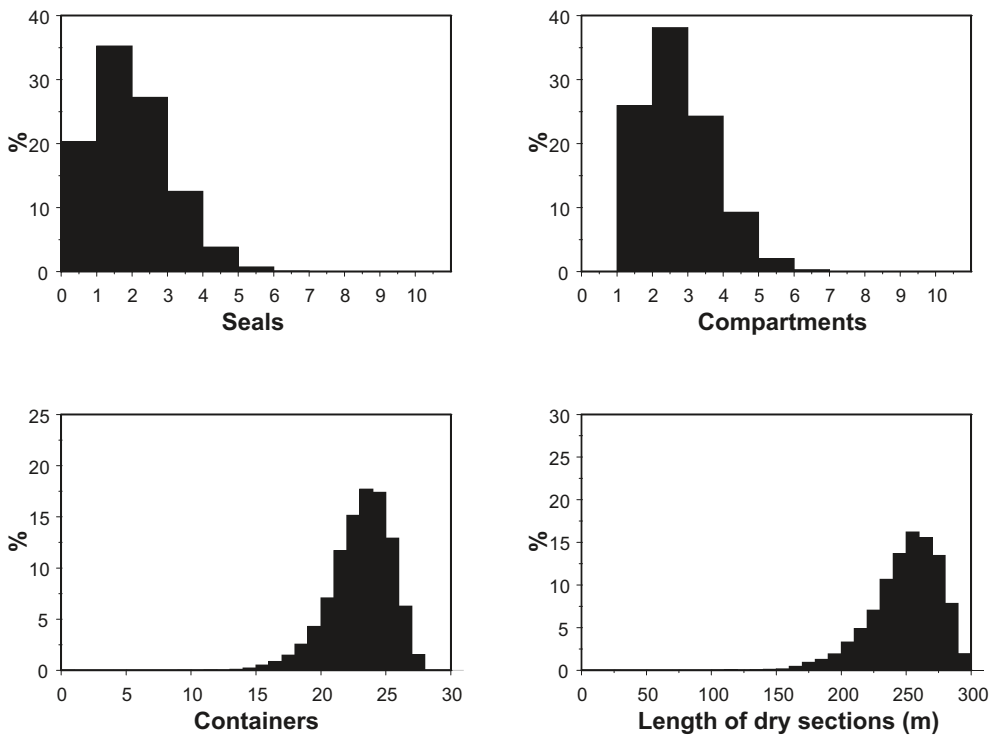
a) Reference case based on /Hellä et al. 2006/

Figure 3-7. *Summary histograms of selected drift measures for each model variant.*
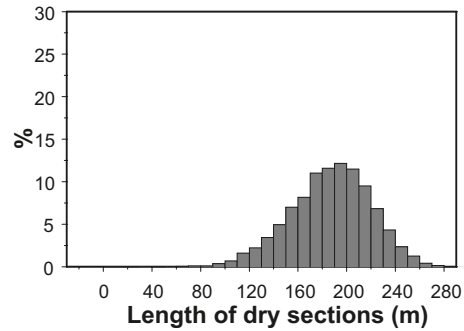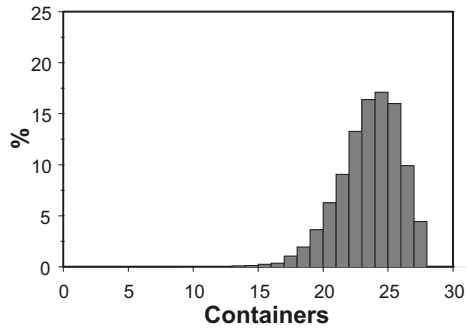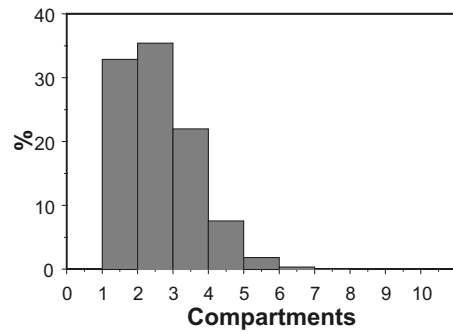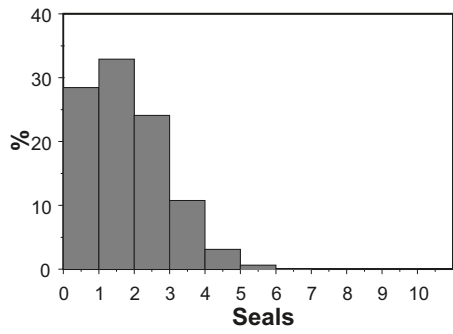
b) Extended reference case
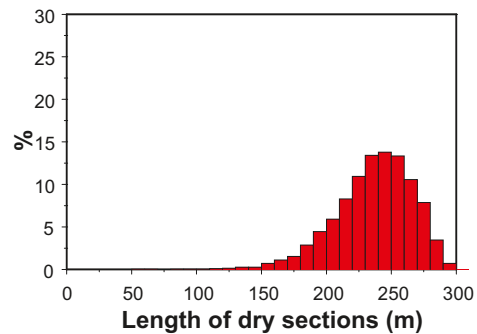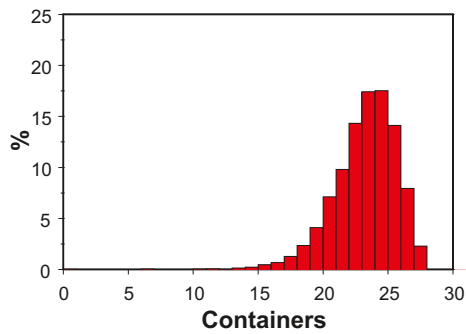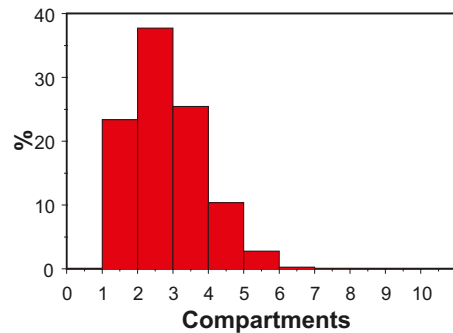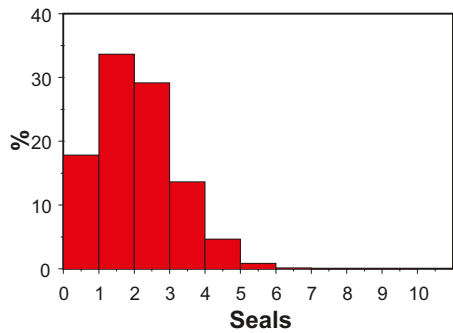
c) LT correlation variant

Figure 3-7. *Continued.*
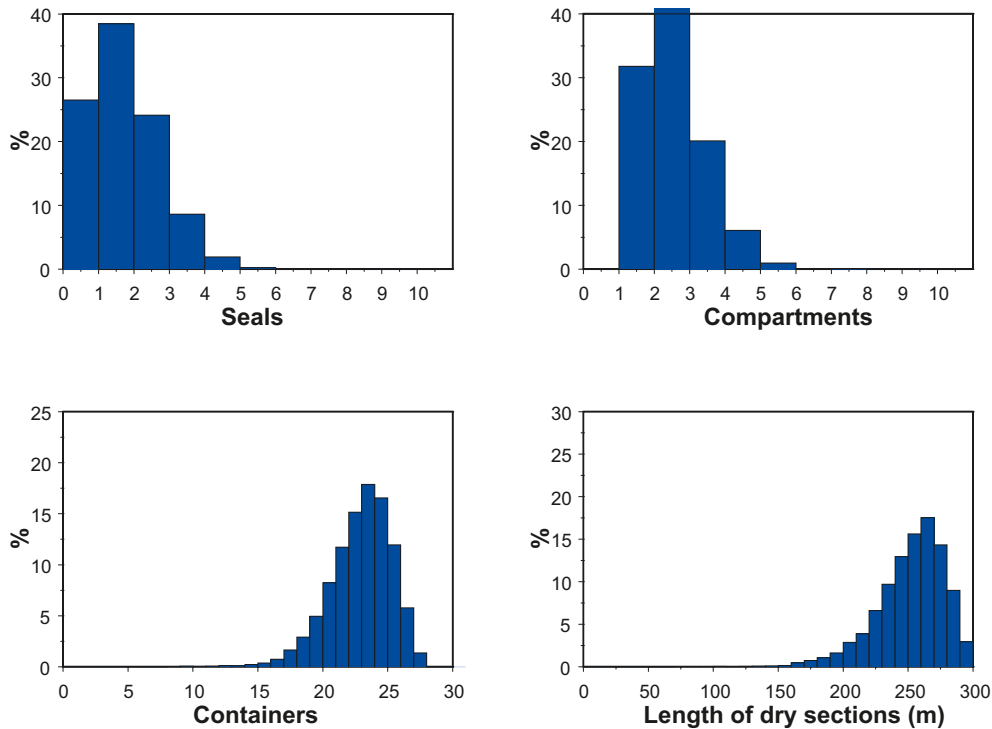
d) Channel variant

Figure 3-7. *Continued.*

Histograms and statistics of selected compartment measures

Histograms of the length, inflow (without grouting), number of dry sections and super-containers in a compartment (over all tunnels, panels and realisations) are shown in Figure 3-8. All model variants in general show similar behaviour.

The only significant difference is in the number of dry sections per compartment, which is greater in the model variants that include lower transmissivity features (between 10^{-9} and 10^{10} m^2/s), as would be expected (more but shorter sections). Also the percentage of very low inflow compartments (< 0.1 l/min) is different for those model variants with more low transmissivity features. For a small number of compartments ($\sim 1\%$) no super-container is emplaced because the compartment contains a WCF with transmissivity $> 2.65 \times 10^{-9}$ m^2/s.

Histograms of selected WCF measures

Histograms of the log $T_{Average}$, inflow (without grouting), intersection angle and trace length for WCFs (over all tunnels, panels and realisations) are shown in Figure 3-9. Again all model variants in general show similar behaviour.

The only significant differences are in the distribution of $\log T_{Average}$ and inflow. Again the difference relates to the treatment of WCFs with transmissivity less than of 10^{-9} m^2/s. All model variants show similar transmissivity distributions above this value (although the percentage of such feature reduces when more low transmissivity WCFs are included in the models). The trace-length distribution peaks at about 6 m because the trace-length for a model fracture normal to the tunnel is about 5.8 m ($2 \times \pi \times 0.925$). Trace lengths below this correspond to cases where the tunnel intersects the edge of a model fracture. This causes the rather unusual shape to the trace-length distribution.
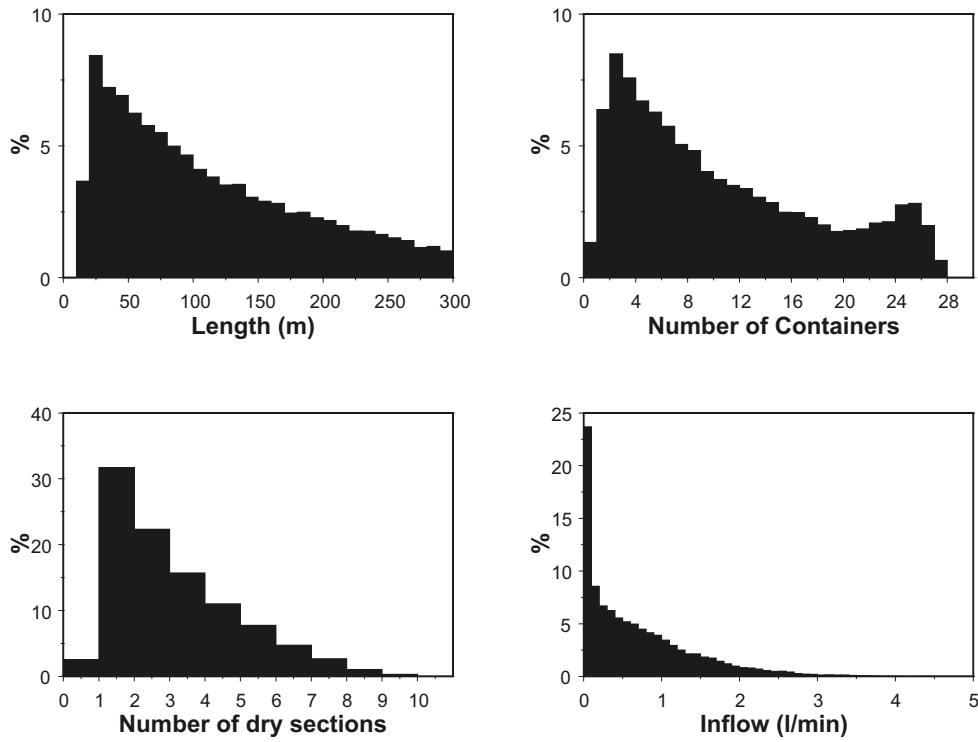
a) Reference case based on /Hellä et al. 2006/
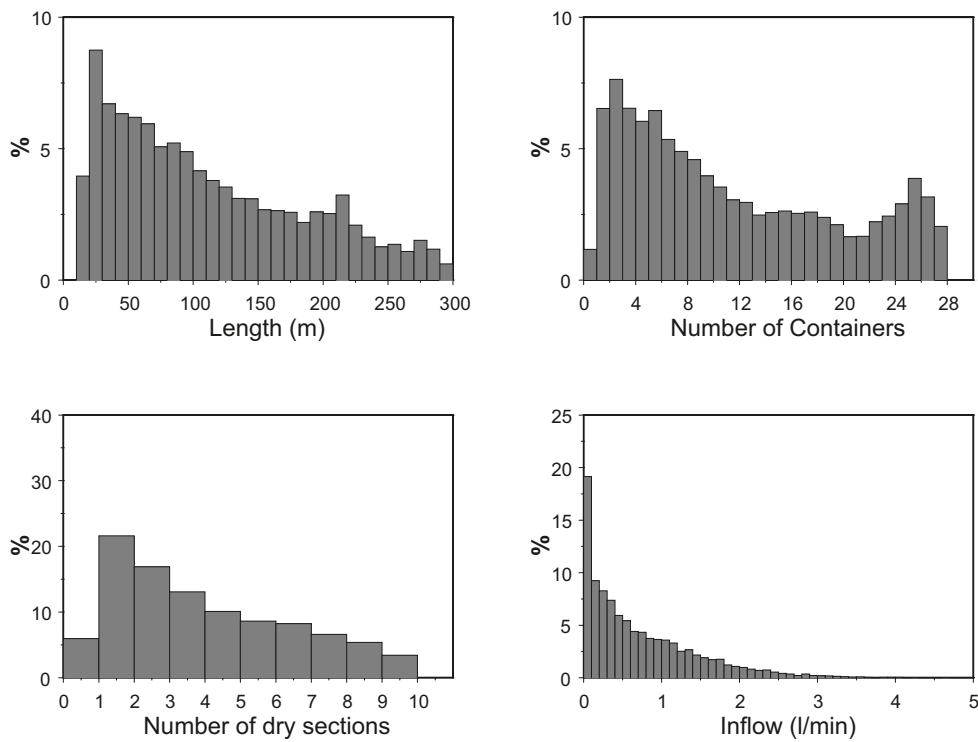
b) Extended reference case

Figure 3-8. *Summary histograms of selected compartment measures for each model variant.*
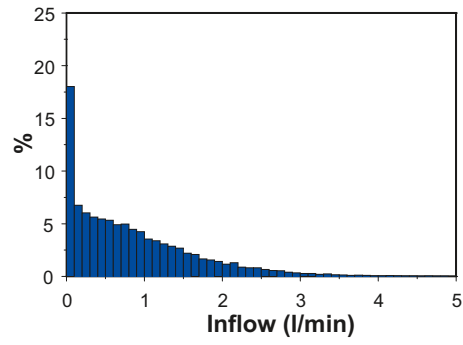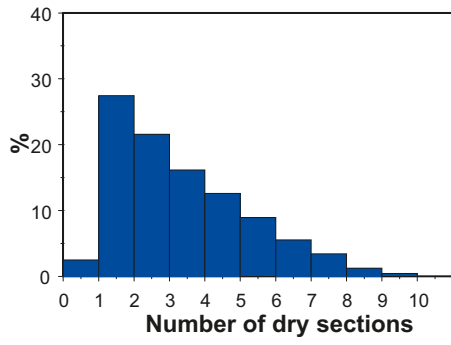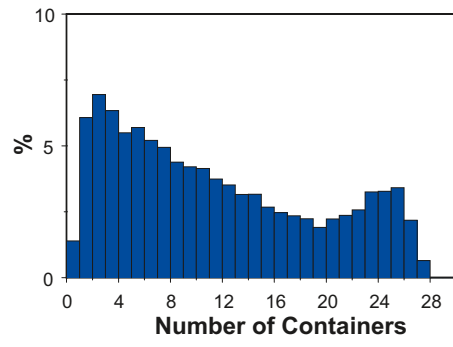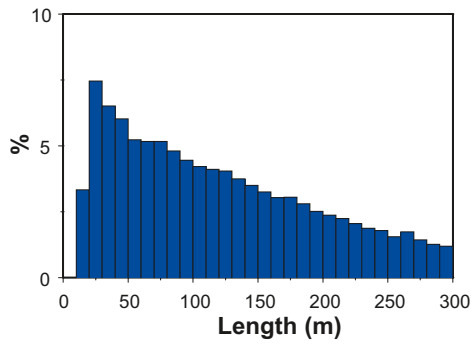
c) LT correlation variant
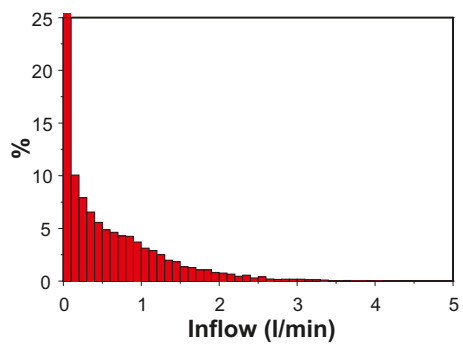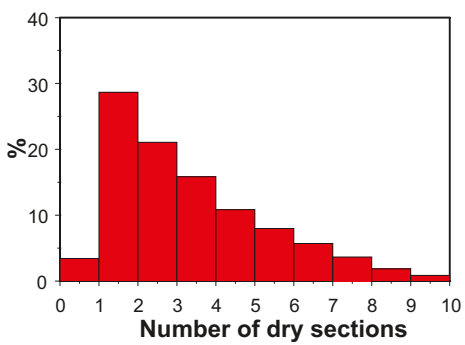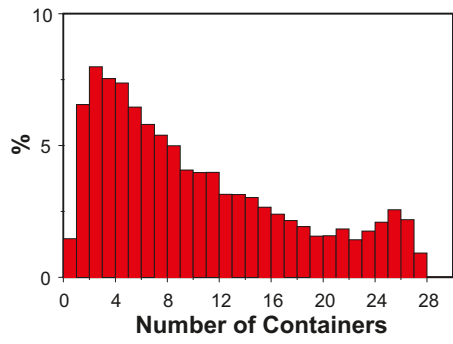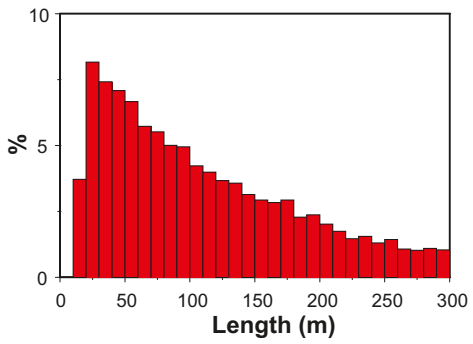
d) Channel variant

Figure 3-8. *Continued.*
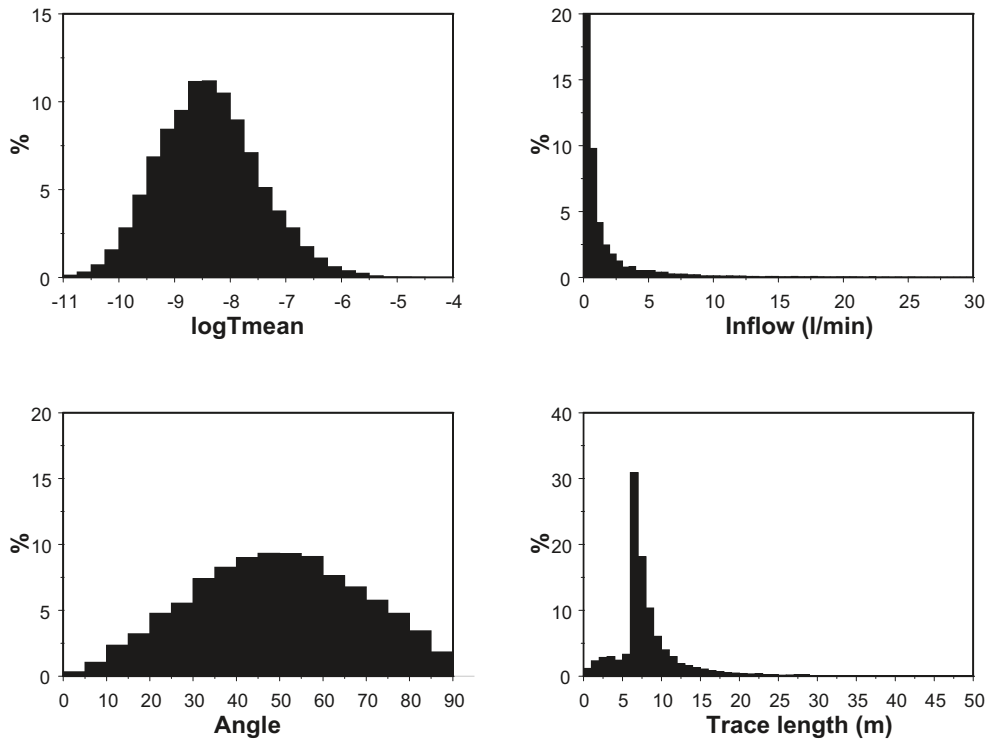
a) Reference case based on /Hellä et al. 2006/
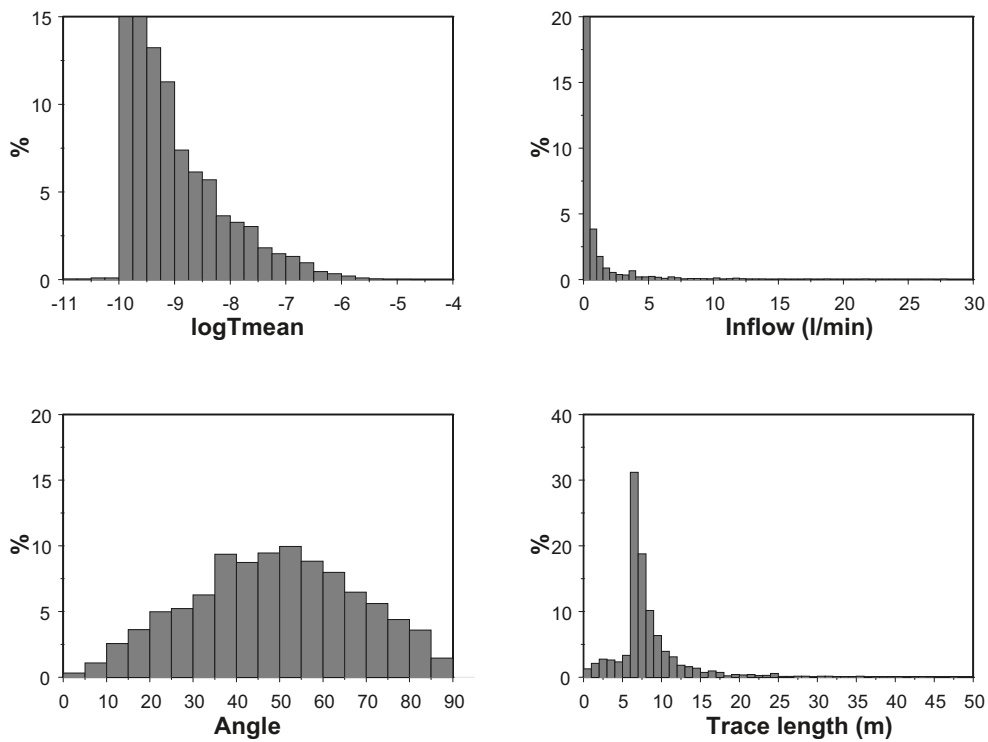
b) Extended reference case

Figure 3-9. *Summary histograms of selected WCF measures for each model variant.*
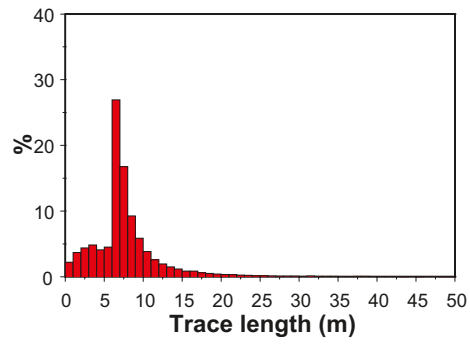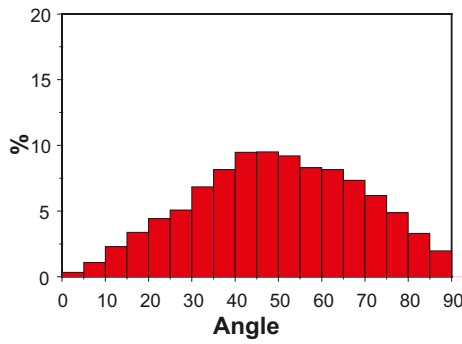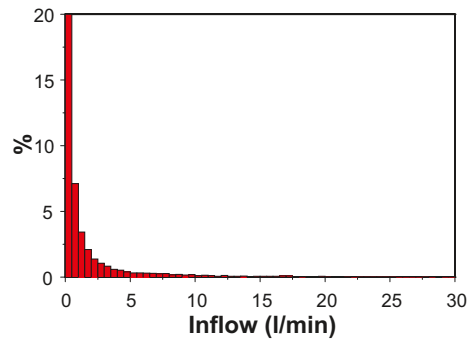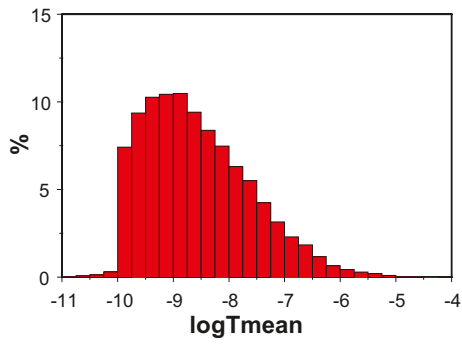
c) LT correlation variant
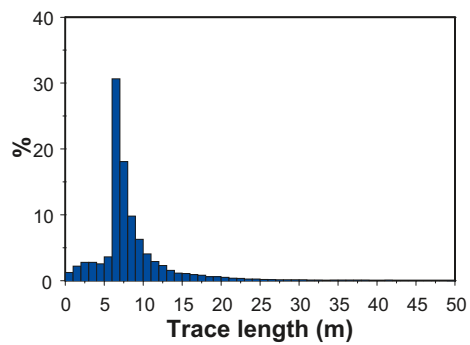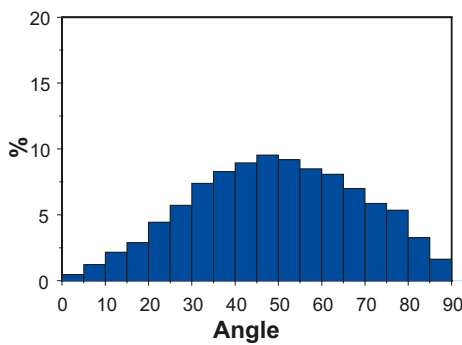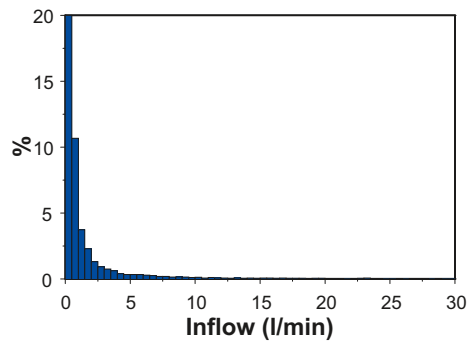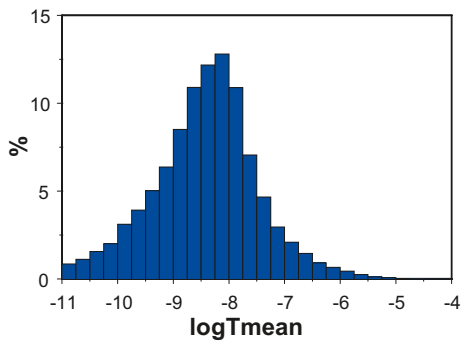
d) Channel variant

Figure 3-9. *Continued.*

3.4   Conclusions

The simulations indicate a very consistent layout across all the model variants and realisations. Typically each 300 m drift is divided into 2 compartments by a compartment plug. Each drift contains on average 23 super-containers with 3–4 blank sections. Total inflow to the compartments (prior to grouting) within a drift is on average about 1.5 l/min. Inflows to a single compartment are below 1.0 l/min.

The different measures are generally insensitive to the differences in the model variants. This is because, for the most part, the measures focus on the probability of intersection with transmissive features with transmissivity $> 10^{-9}$ m^2/s. As all the model variants have been well calibrated to the borehole inflow data as shown in Figure 2-5, there is very little difference in the results. The only significant differences arise from the treatment of lower transmissivity features and prediction of dry zones (drift intervals with transmissivity below 10^{-10} m^2/s). For the two model variants where additional transmissive features in the range 10^{-10} to 10^{-9} m^2/s have been added (Reference Extended and Channel variant) dry section lengths are reduced as would be expected.

Given the observed lack of variation between the model variants it is useful to consider what features of the fracture system might make significant differences to the results. Possible fracture system features are:

- Clustering of WCFs and LFZs creating zones of more intense fracturing and large un-fractured regions.

- Depth trends in the fracture system such that the properties derived by averaging over the 300–750 m depth horizon are not representative of 400 m depth (e.g. if fracture density dropped significantly below 500 m).

- Different interpretations of LFZ orientation and distributions (currently assumed to mimic the orientation distribution derived from outcrop maps).

- Very small scale channelling at sub-metre scales. The channel variant includes transmissivity variation across WCFs at 1/10 the size of the WCF i.e. from 1 to 50 m. Given most intersections are with the largest structures there is little difference in the intersection statistics of a 100 mm diameter borehole and a 1.85 m tunnel. However if channels occur at small scales e.g. cm or dm then intersection statistics for tunnels might be significantly different than for boreholes.

- Flow concentrated in small fractures. The models have only considered fractures > 10 m in length as contributing to significant flow.

- Any bias in the measurement of transmissivity during flow logging.

- Action of near tunnel-wall processes in changing inflows (e.g. ventilation, EDZ, two-phase flow).

4   Single fracture flow model

A semi-analytic model of flow and pressure in a fracture intersecting a drift containing a super-container or distance block was developed using the advanced well-test analysis package nSights /Roberts et al. 2002/. The aims of the single fracture model were to:

- Illustrate sensitivity to model parameters and identify suitable parameter ranges.

- Develop understanding of likely flow and pressure response at a super-container during excavation, operation and post closure.

- Provide verification for CONNECTFLOW developments using time-varying boundary conditions.

4.1   Model

The model features are listed in Table 4-1 and the geometry illustrated in Figure 4-1.

The different excavation phases considered were:

- Excavation and operation represented as a fixed atmospheric pressure inner boundary in the test zone.

- Filling of open (gap) void space around super-container represented as a period of atmospheric pressure in the test zone until the volume around the super-container is filled.

- Saturation of bentonite pore volume and pressure recovery represented as a "shut-in" (end of flow) period with fixed storage (volume and compressibility of super-container and associated voids).

The timescales used for simulation of each phase were:

- Excavation and operation: 30 days (720 hours)

- Filling of open void space: Calculated from void space volume/inflow

- Pressure recovery: 10 years

Table 4-1. Well-test model and disposal system features represented in single fracture model.

Well-test model feature	Disposal system feature	Properties
Test zone	Storage term associated with super-container or distance block volume.	Pore volume (m^3)
		Pore compressibility (Pa^{-1})
Skin zone	Possible zone of grouting.	Thickness/radius (m)
		Transmissivity (m^2/s)
		Storativity (–)
Formation	A single uniform transmissive fracture.	Transmissivity (m^2/s)
		Storativity (–)
Boundary	Distance to geosphere unaffected by drawdown to drift.	Radius (m)
		Pressure (kPa)
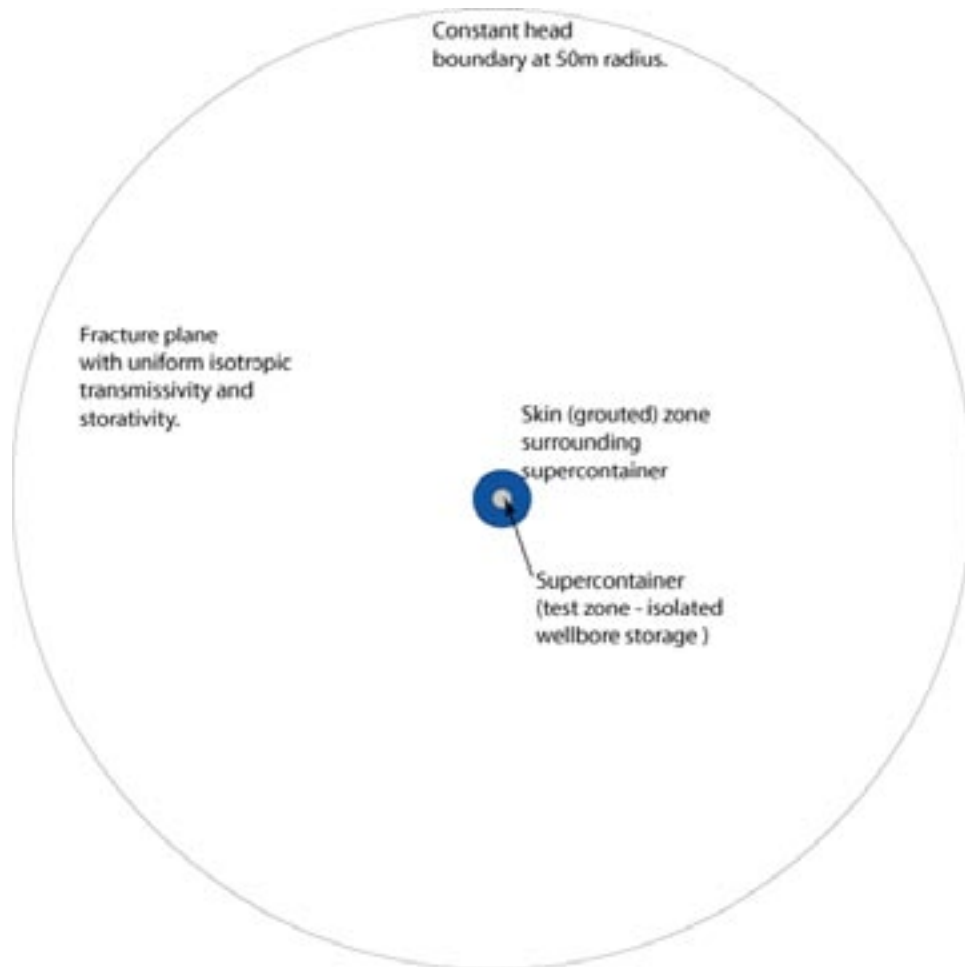
Figure 4-1. *Single fracture well-test analysis model geometry.*

Note that the timescales for excavation and operation represent an absolute minimum given the planned excavation schedule.

The following sets of model run were performed:

1. Model with no skin (grouted) zone for varying fracture transmissivity.
2. Model with skin (grouted) zone for varying fracture transmissivity.
3. Sensitivity of models to fracture storativity for model with no skin.
4. Sensitivity of models to test zone storage model with no skin.
5. Sensitivity of models to skin zone conductivity.

Within the models fracture storativity has either a) been held constant at 10^{-8} or b) it has been assumed that fracture transmissivity T and storativity S are correlated. /Doe and Geier 1990/ have suggested a power-law relationship of the form $S = c_1 T^{c_2}$. The CONNECTFLOW DFN model uses such a relationship with $c_1 = 0.25$ and $c_2 = 0.74$ as its default for estimation of storativity from transmissivity. The value of 10^{-8} is equal to that predicted by the power law for fractures with a transmissivity of 10^{-10} m^2/s.

Within the model the pressure rise in the EBS due to inflow after closure is controlled by a storage term (equivalent to wellbore storage in a well test). In this context storage is a "lumped term" incorporating multiple effects (e.g. inflow into the compacted bentonite; compressibility of gel/water mix in the gap volume, effect of trapped air and compressibility of the rock and compacted bentonite), which will change with time as the bentonite swells and homogenises.

Table 4-2. Single Fracture Model properties.

Property	Value	Comment
Fracture Transmissivity (m^2/s)	10^{-11}–10^{-7}	Features with inflows greater than that corresponding to a transmissivity of 2.65×10^{-8} m^2/s will be sealed with plugs, while features greater than 2.65×10^{-9} m^2/s correspond to blank zones where no super-container will be emplaced.
Fracture Storativity (–)	10^{-8} or $S = 0.25T^{0.74}$	See discussion below
Test Zone Compressibility (m^3/Pa)	Range of values used	See discussion below
Skin zone transmissivity (m^2/s)	10^{-10}	Assumption – results in reduction of flow for fracture transmissivity > 10^{-10}
Skin zone storativity (–)	10^{-9}	Fracture is assumed to be stiffer after grouting
Skin zone thickness (m)	2	Assumption

Values for the storage term for super-containers and distance blocks are uncertain and a range of approaches to estimating the parameter have been suggested:

- Assume zero storage – equivalent to assuming that the drifts are completely filled with rigid material

- Assume storage is dominated by the compressibility of the water in the gap volume around the super-container or distance block

- Assume storage is dominated by the compressibility of air trapped in the gap volume

- Scaling of the results from laboratory sealing tests using the Big Bertha mock-up tests performed by Clay Technology /Börgesson et al. 2005/.

These different approaches are considered in more detail in the drift-scale flow models discussed in Chapter 5. For the single fracture flow model either zero storage or scaled values of the laboratory tests were used to bound the behaviour.

A series of near full-scale tests have been performed by Clay Technology to investigate the behaviour of distance blocks and super-containers during saturation and swelling /Börgesson et al. 2005/. The largest tests were performed with the "Big Bertha" test cell (see Figure 4-2). After filling of the "gap" in the Big Bertha experimental setup, water was injected into the test cell to create a roughly linear pressure rise as shown in Figure 4-3. The storage was calculated from the change in pressure with net injected volume (see Figure 4-4). Storage varies during the test but a typical value when pressures were rising with injected volume is ~2×10^{-9} m^3/Pa.

Average values for storage have been and are listed in Table 4-3. Given the complex processes that occur during the hydration of the bentonite there is significant uncertainty as to how the Big Bertha values could be scaled (e.g. no scaling, by linear dimension, by surface area or by volume). Scaling by volume was taken as the upper bound and for a super-container cell of length 5.56 m and tunnel diameter of 1.85 m results in an increase by a factor of 85. The storage values appear to increase with the volume of open void space (largest value in BB-1) and Clay Technology /Börgesson et al. 2005/ suggest that values from other tests are in the 10^{-10}–10^{-9} m^3/Pa range, resulting in scaled storage values in the range 10^{-8}–10^{-7} m^3/Pa. Within the single fracture models two values of storage 8.0×10^{-8} and 2.7×10^{-7} m^3/Pa have been used to understand the sensitivity to this parameter. Most models have used a value of 2.7×10^{-7} m^3/Pa. The lower value was used to illustrate the sensitivity to the parameter.
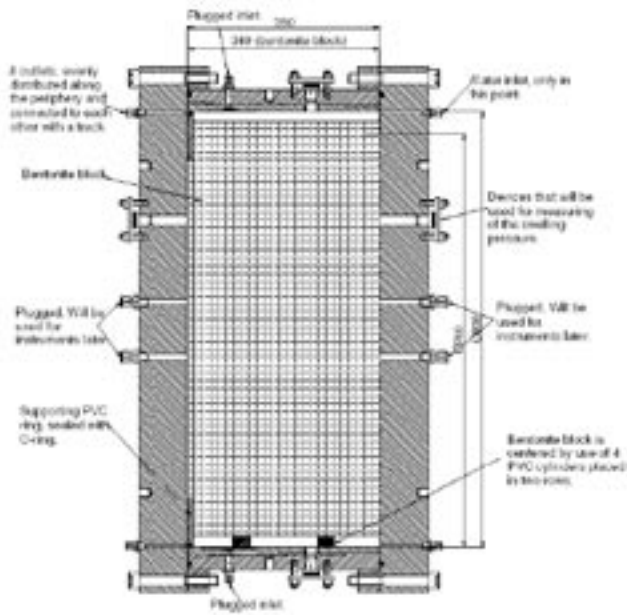
Figure 4-2. *Big Bertha setup for distance block sealing test 2 /from Börgesson et al. 2005/.*
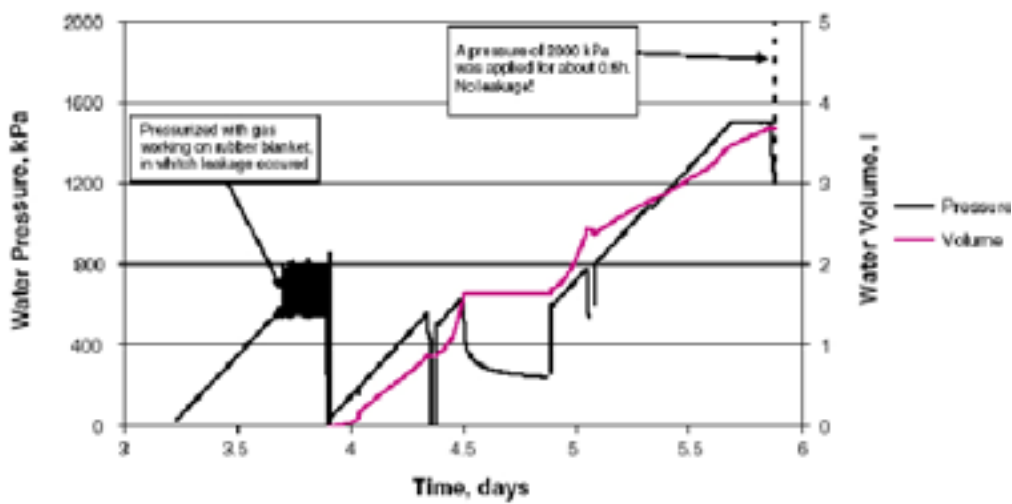
Figure 4-3. *Sealing Test 2 plot of pressure and volume versus time in days /from Börgesson et al. 2005/.*
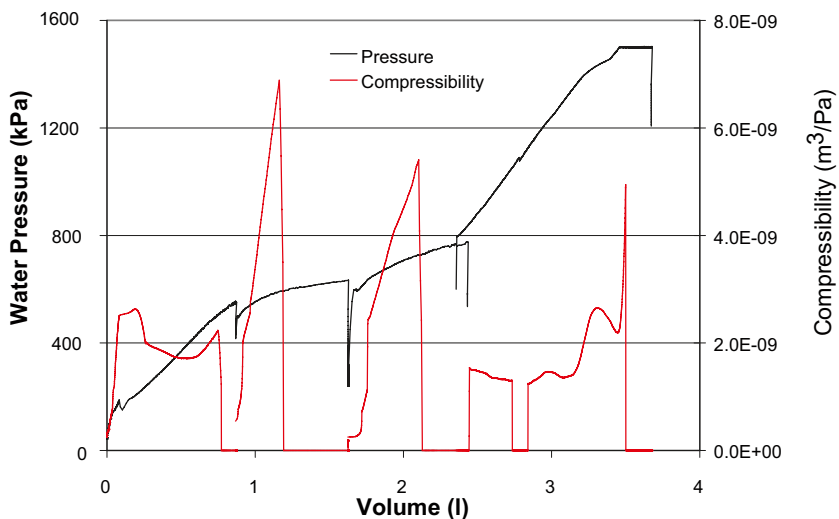
Figure 4-4. *Sealing test 2 plot of pressure and compressibility versus volume.*

Table 4-3. Average compressibility from Big Bertha tests /see Börgesson et al. 2005/.

Test	Gap/ open voids	Injected volume (l)	Pressure rise (kPa)	Mean storage (m³/Pa)	Scaled-storage (m³/Pa)
BB-1	4 cm + vertical slot	10	1,200	8.3×10^{-9}	7.1×10^{-7}
BB-2	4 cm	3.5	1,500	2.3×10^{-9}	2.0×10^{-7}
BB-7	4 mm	1.5	2,000	7.5×10^{-10}	6.4×10^{-8}

Excavation and operation

Figure 4-5 shows the calculated inflow rates for varying fracture transmissivity with and without a skin (grouted) zone. The presence of the skin zone results in a reduction in inflow for transmissivity greater than 10^{-10} m²/s as would be expected. It can be seen that the inflows stabilize at close to the steady state values within 1,000 hrs of excavation for all fractures with transmissivity greater than 10^{-11} m²/s. Higher transmissivity features with a skin (grouted) zone also stabilise within 1,000 hrs.

Filling of open void space

The steady state inflow (taken as the flow at the end of the excavation and operation period) and the estimated time to fill the open volume around the super-container (1.5 m³) are given in Table 4-4. for varying fracture transmissivity with and without skin zone. Note the close correspondence between the nSights calculation and the analytic solution.

Pressure recovery

Figure 4-6 shows the pressure recovery and derivative for varying fracture transmissivity. Gradients greater than 100 kPa/hr are limited to the most transmissive fractures (> 10^{-8} m²/s) and occur in early time. The speed of pressure recovery is a function of the flow-rate (transmissivity) and compressibility of the test zone (super-container) volume.

The pressure recovery after "shut-in" is strongly controlled by the compressibility of the test zone. Information on the range of compressibility has been derived from the results of large scale (Big-Bertha) mock-up tests performed by Clay Technology /Börgesson et al. 2005/.

Table 4-4. Inflow to super-container section from model with skin zone for varying fracture transmissivity.

Fracture transmissivity (m²/s)	Skin Zone	Analytic steady state inflow (l/min)	Model inflow (l/min)	Time to fill open void space (days)
10^{-7}		3.7794	3.7809	0.3
10^{-8}		0.3779	0.3781	3
10^{-9}		0.0378	0.0378	28
10^{-10}		0.0038	0.0038	276
10^{-11}		0.0004	0.0004	2,755
10^{-7}	Y		0.0131	80
10^{-8}	Y		0.0128	81
10^{-9}	Y		0.0105	99
10^{-10}	Y		0.0037	276
10^{-11}	Y		0.0005	2,039
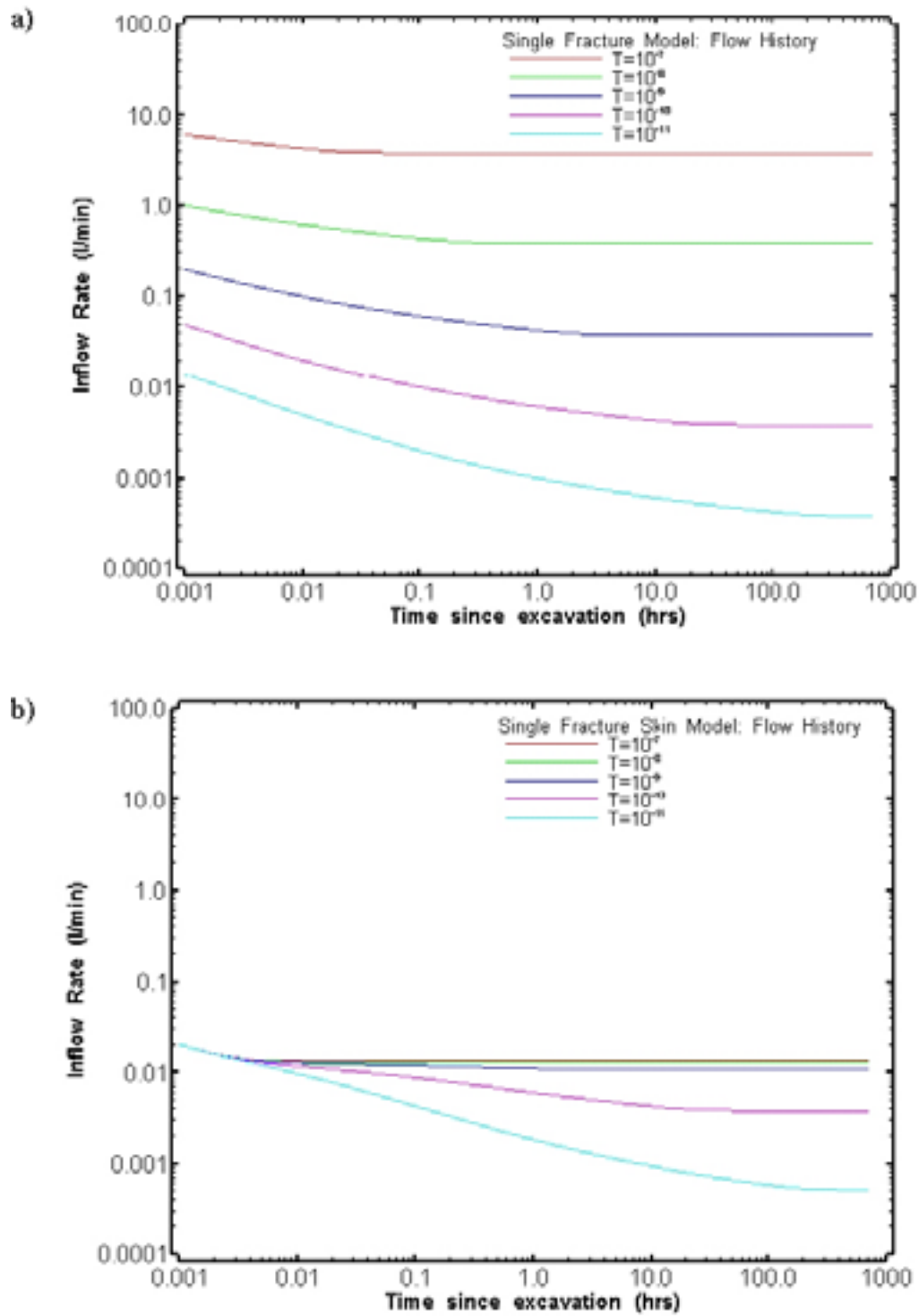
Figure 4-5. *Calculated inflow after excavation for varying fracture transmissivity. a) without skin zone, b) with skin zone.*
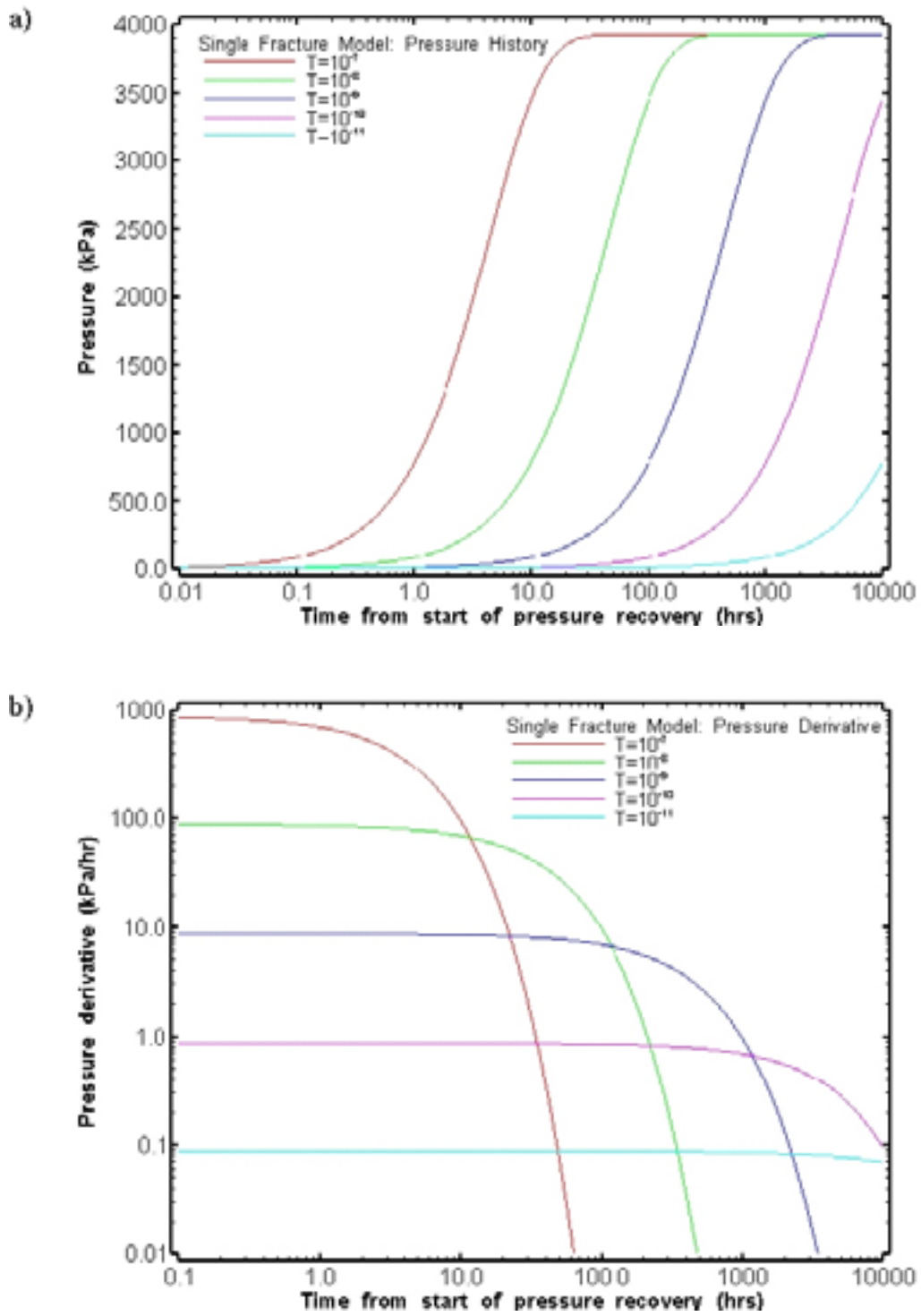
Figure 4-6. *a) Pressure recovery and b) pressure derivative (kPa/hr) for varying fracture transmissivity for varying fracture transmissivity.*
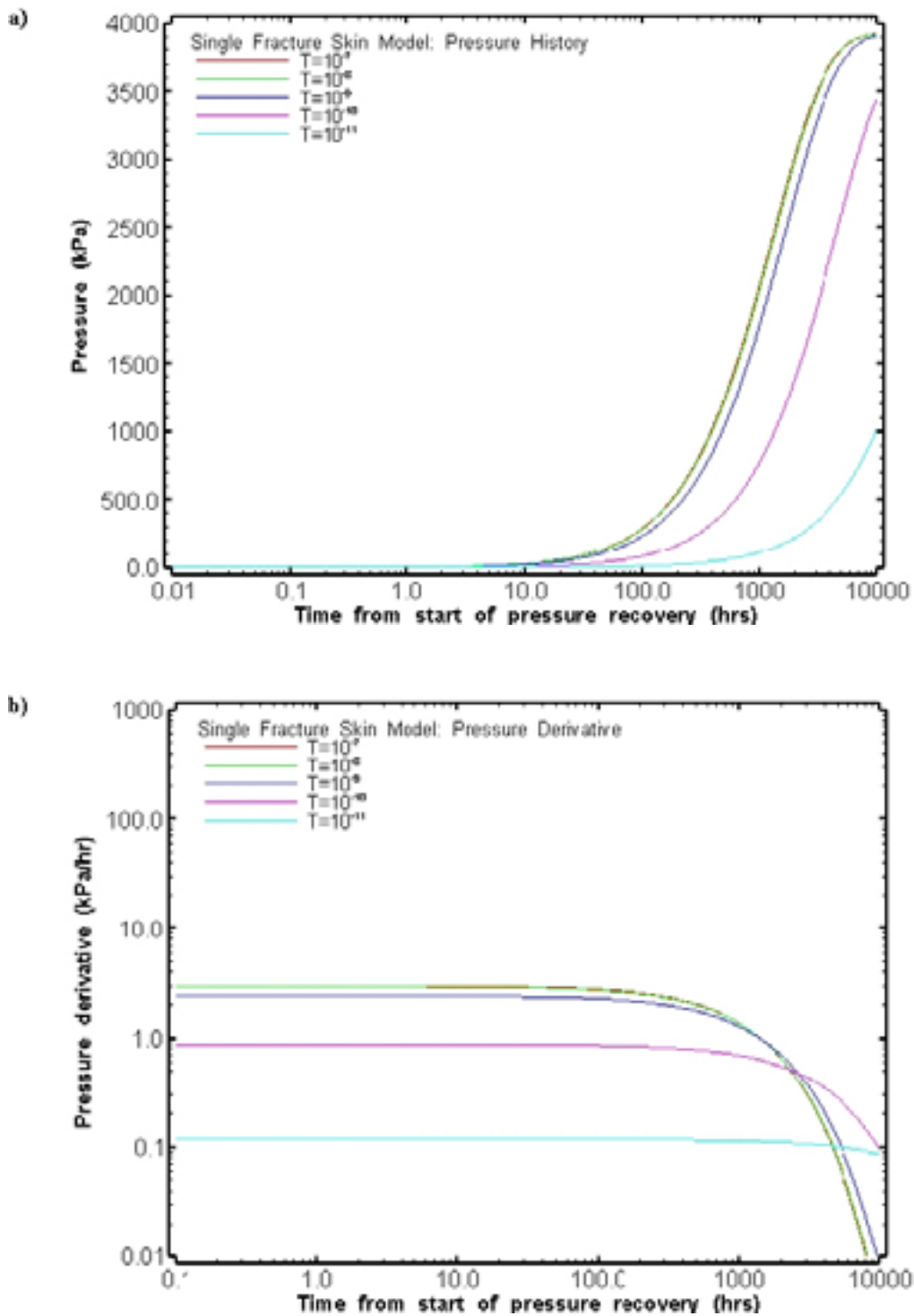
Figure 4-7. *a) Pressure recovery and b) derivative (kPa/hr) for varying fracture transmissivity with 2 m skin zone of transmissivity 10^{-10} m²/s.*

The effect of differing storage terms on the pressure recovery can be clearly seen in Figure 4-8 where the pressure and pressure derivative (kPa/hr) are plotted for a fracture transmissivity of 2.65×10^{-9} m²/s equivalent to a 0.1 l/min inflow (maximum inflow to super-container or distance block section according to current design see Table 3-1). For storage terms greater than 8×10^{-8} m³/Pa the pressure derivative does not exceed 100 kPa/hr.
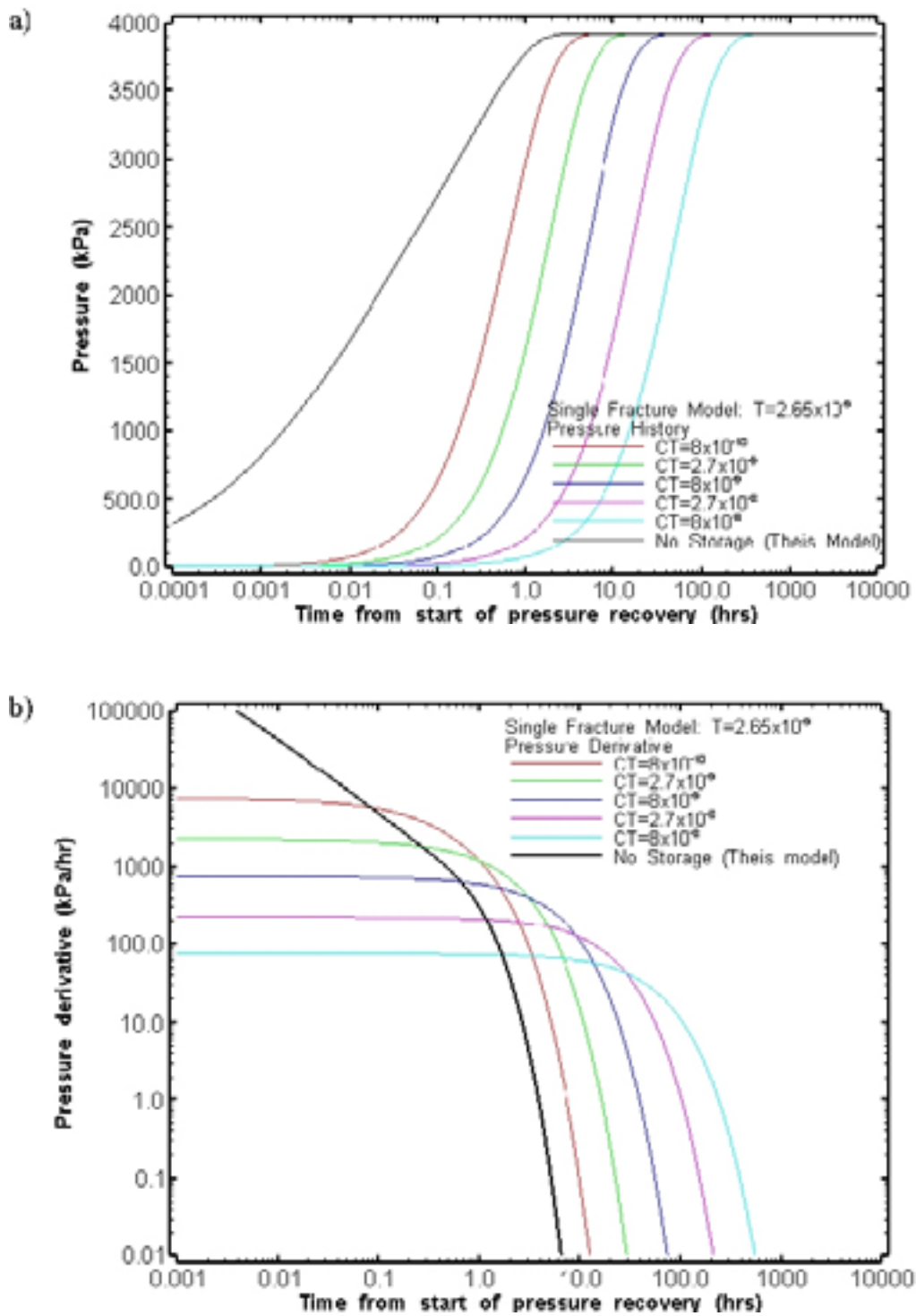
Figure 4-8. *a) Pressure recovery and b) derivative for fracture with transmissivity =2.65x10⁻⁹ m²
(0.1 l/min inflow) and varying storage CT (m³/Pa) from nSights model.*

4.2 Response to opening and closure of an adjacent drift

The nSights model allows the calculation of pressure responses at a distance from the test zone. The radial symmetry of the model, however, does not allow any storage to be associated with these "observation wells". The pressure responses at observation wells correspond to "point measurements" and may be significantly over-estimated for monitoring intervals (or closed drifts) with significant storage /see Black and Kipp 1977/. The single fracture model without skin zone was adapted to include an observation well at 25 m radius. The predicted drawdown as a response to excavation (application of atmospheric pressure boundary condition) for varying fracture transmissivity is shown in Figure 4-9. The delay in response decreases with increasing transmissivity while the final drawdown (approximately 650 kPa) does not vary.

The pressure recovery and pressure derivative are shown in Figures 4-10 and 4-11. It can be seen that the derivative is below 10 kPa/hr for fractures of 10^{-8} m²/s or lower. In reality the recovery is likely to be slower than that shown in the figures because:

- 25 m is the minimum distance between drifts.
- The effects of storage associated with the closed drift at 25 m distance have been ignored.
- The drift at 25 m distance may not have fully recovered from its own closure.
- The assumption of a fixed head boundary condition 25 m from the observation well (50 m from test zone).

In these models the drawdown and recovery are limited by the assumption of radial uniform properties and presence of a fixed head boundary condition. Higher drawdowns might occur in channelled or partially disconnected fracture systems, but recovery would then be slower.

The pressure converges to approximately 3,250 kPa in all the models, this is the steady state pressure at 25 m radius for the prescribed boundary conditions and is independent of transmissivity and storage.
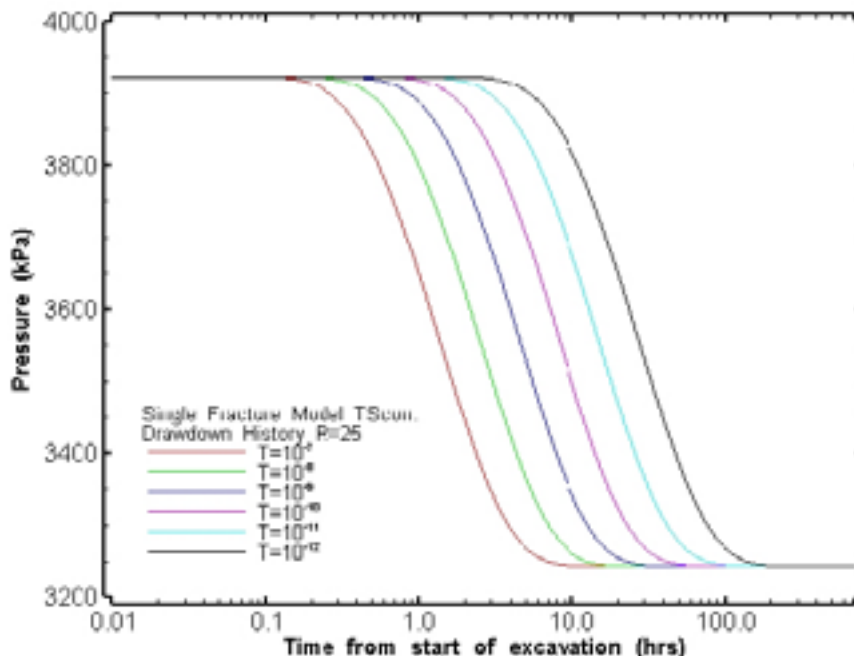
Figure 4-9. *Pressure for varying fracture transmissivity during drawdown (open drift) for a point at 25 m radius from drift.*
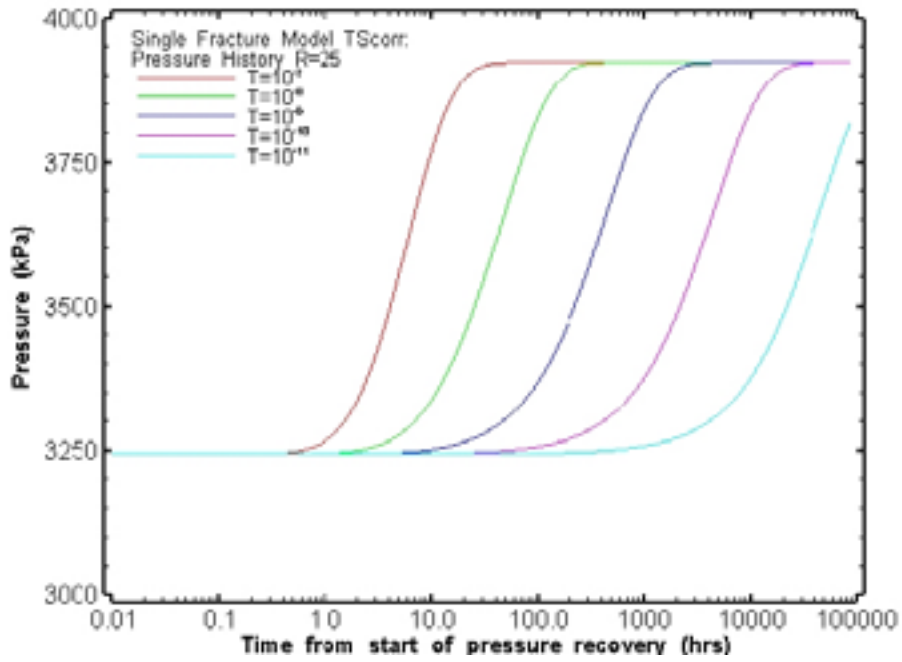
Figure 4-10. *Pressure recovery for varying fracture transmissivity during pressure recovery for a point at 25 m radius from drift.*
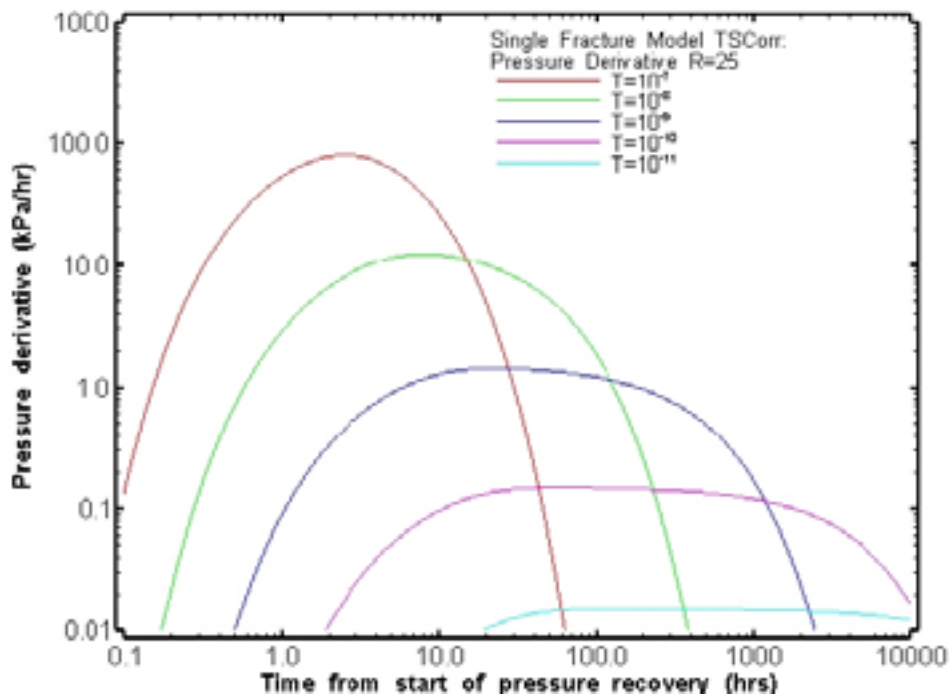
Figure 4-11. *Pressure derivative (kPa/hr) for varying fracture transmissivity during pressure recovery for a point at 25 m radius from drift.*

4.3   Single fracture model conclusions

The study has provided useful input to the development of the DFN models and illustrated the sensitivity of different measures to the parameters:

- Inflows during excavation and operation are controlled by fracture transmissivity and skin in late time, but in early time are also influenced by fracture storativity.

- Pressure in the transmissive part of the fracture network ($> 10^{-10}$ m²/s) is likely to be near steady state at the end of excavation/preparation of the drift. Transient conditions will continue within the matrix and very low transmissivity fractures. Any transients within the more transmissive network will be due to sealing and excavation of nearby drifts, changes in ventilation. Transients due to annual cycles, barometric and earth tide responses would be expected to be small.

- Within the model the time prior to start of pressure rise is largely a function of open volume and fracture transmissivity and skin.

- Speed of pressure recovery is largely a function of inflow rate (controlled by fracture transmissivity and skin) and storage of the test zone (super-container volume).

- Pressure drawdown and recovery in adjacent drifts are of limited magnitude in the single fracture model. Drawdowns may be larger in highly channelled fracture geometries.

- Data on the test zone storage has been taken from the Big Bertha experiment and scaled to super-container volumes. Compressibility varies significantly between tests and the appropriate scale factor is uncertain.

The model assumes that the super-container can be treated as "wellbore storage" with a fixed volume and compressibility. In reality part of this compressibility comes from leakage into the compacted bentonite and so the "compressibility" will vary with time also after the bentonite has swollen into the gap and homogenised we might expect the system to have significantly lower compressibility. Any trapped air within the gap (most likely at early time) will result in significantly higher compressibility.

The treatment of the super-container volume also ignores issues relating to two-phase flow (e.g. presence of trapped air or waste generated gas) within the super-container volumes and assumes that there is no influence from flow from surrounding distance blocks. Models including representations of flow within the bentonite buffer indicate long saturation times (/Börgesson et al. 2005/ see Figure 5-19). The bentonite blocks are however likely to start to swell as soon as water is available.

5 Drift scale flow models

The drift scale models described in this chapter considered transient flow around either one or two drifts. The models used the Extended Reference case DFN model (see Chapter 2) as this model variant was consistent with both inflow and 2 m packer test data and included low transmissivity features. The aim of the modelling was to simulate the scenarios of interest to the Process and Evolution teams as outlined in Chapter 1. Steady state models of flow post EBS saturation were also performed and are described in Appendix B.

Only a limited number of model runs were performed due to the cost of the transient flow simulations. Four sample drifts were selected from one realisation of the Extended Reference Case. All four drifts were located in Panel 1 of the western section of the repository. Figure 5-1 shows the DFN models used for each of the drifts considered here. The individual features are split up into 10×10 m sub-fractures which are each in turn discretised as a grid of 1,000 or more linear finite elements for flow calculations.

Within the transient flow models, the storativity of each feature within the network has been assumed to be correlated with its transmissivity. /Doe and Geier 1990/ suggested a power-law relationship of the form $S = c_1 T^{c_2}$. The CONNECTFLOW DFN model uses such a relationship with $c_1 = 0.25$ and $c_2 = 0.74$ as its default. The main influence of the different storativity on the models within this study is in the change in inflow during excavation (higher flow rates occur as water come out of storage in the fracture) and the speed of pressure recovery for models where storage associated with drift elements is small.

5.1 Repository layout and adaptation

The repository layout and adaptation is substantially the same as that used in the geometric simulations discussed in Chapter 3. The only changes relate to compartment plugs and blank zones, where the designs had evolved during the course of this study.
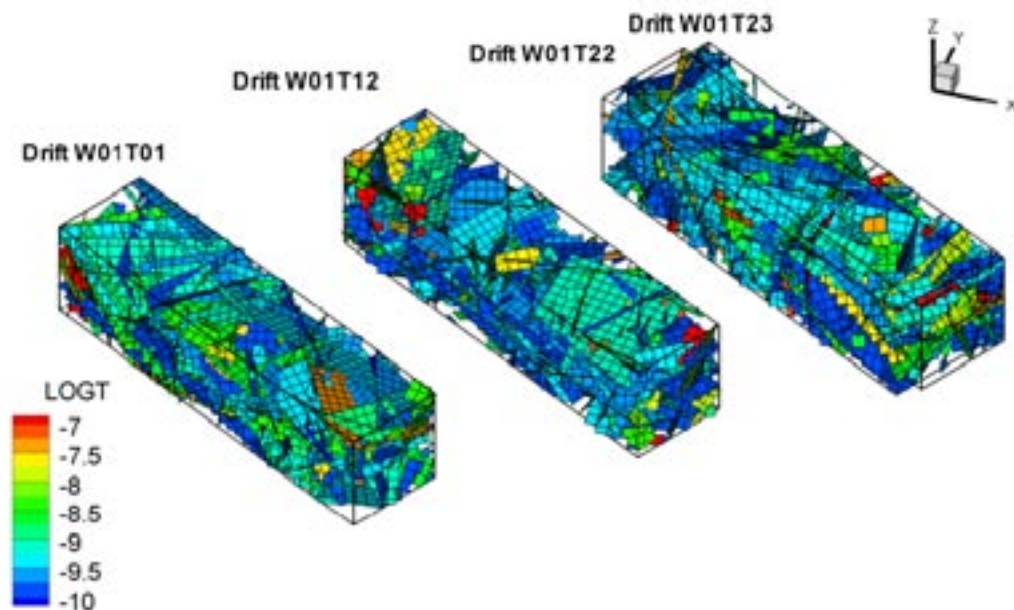
Figure 5-1. *Fracture network model volumes around selected drifts – Extended Reference model for features with transmissivity > 10^{-10} m²/s.*

5.1.1 Compartment plugs and blank zones

Plugs are set around WCF intersections where the average transmissivity is greater than 2.65×10^{-8} m^2/s. The ends of the seals are positioned beyond the end of the high transmissivity traces and extend 15 m on either side of them (or to the end of the tunnel). The design of the plugs is still under discussion and the representations used here are based upon those discussed at a meeting of 7–8/02/06 in Espoo. The geometric simulations assumed a smaller minimum plug length compared to the 30 m used here. Within the flow models each plug is represented as three sections: a 10 m low permeability compartment plug; a permeable fill zone covering the high transmissivity feature traces and 5 m either side of the trace; and a second 10 m low permeability compartment plug.

Compartment blank zones

A "blank zone" of minimum length 10 m is emplaced over intervals within a compartment which contains WCFs of transmissivity greater than 2.65×10^{-9} m^2/s. Super-containers will not be emplaced in such zones. The limit chosen corresponds to an inflow of about 0.1 l/min which is considered a possible limit for piping in the buffer. The geometric simulations assumed smaller blank zones.

5.1.2 Deposition drift representation

The deposition drifts (containing super-containers, distance blocks and permeable fill elements and compartment plugs) have been represented within the CONNECTFLOW transient models as a series of 1D elements, where each super-container or distance block is represented as a single element. Typically each drift was made up of 50–55 such elements. Each element was associated with axial conductance (permeability×area) and storage and could be treated as either a fixed pressure (head) or flux boundary condition.

The 1-D borehole/shaft model in CONNECTFLOW is illustrated in Figure 5-2. The 1-D model was developed for modelling boreholes and has been adapted for modelling open shafts. The limitations of the model are:

- Storage is only associated with one fracture intersection on each element and is not distributed along the element.

- A point rather than distributed intersection is assumed (i.e. all intersections are equal and no account is taken of trace lengths or relative orientation).

- To accurately match the flow convergence around the borehole/shaft the local finite element discretisation needs to be larger than the borehole/shaft radius.

These limitations are typically insignificant for boreholes (small diameter, high axial conductivity) but should be born in mind when considering large diameter shafts and tunnels.

The axial permeability used for each type of drift element is given in Table 5-1. The permeability of the distance blocks, bentonite blank zones and compartment plugs have all been set to 10^{-20} m^2 so that cross-flow within the corresponding drift elements is limited. A higher axial permeability has been set for the super-containers to allow for cross-flow within a super-container section during the early stages of evolution.

The drift elements are assumed not to be connected as sealing of the distance blocks is expected to occur on emplacement for the Basic Design (tight distance block concept). For the DAWE concept we have also assumed disconnected elements which is perhaps more open to question.

An alternative representation using a continuous porous medium (CPM) mesh to represent the Engineered Barrier System was used for some of the steady state models discussed in Appendix B.
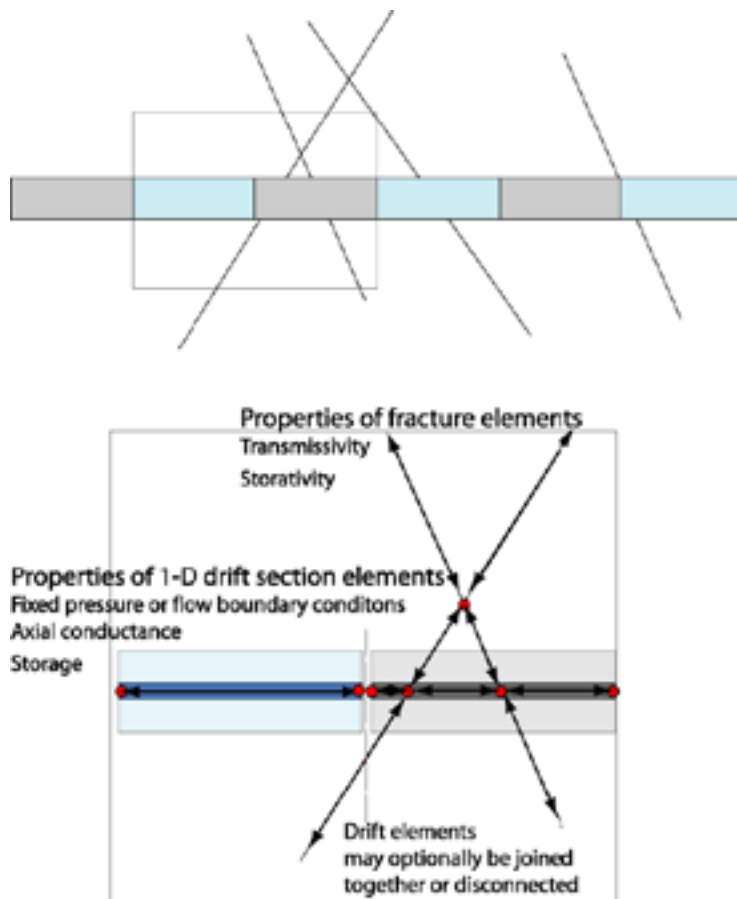
Figure 5-2. *Schematic showing drift representation.*

Table 5-1. Drift element properties used in models.

	Axial permeability (m²)	Radius (m)	Storage (m³/Pa)	Connectivity
Super-container	1×10^{-14}	0.925	See next section	Elements are not con-
Distance Block	1×10^{-20}	0.925		nected along drift – i.e.
Blank fill	1×10^{-20}	0.925		distance blocks assumed
Compartment Plug seal	1×10^{-20}	0.925		to seal.
Compartment plug fill	1×10^{-12}	0.925		

5.1.3 Drift element storage coefficient

A range of different models has been developed for the "storage term" associated with each drift section in the DFN flow models. Within the models it is necessary to link the flow into the element with the pressure via a storage term in m³/Pa. In the real system a range of processes occur as water enters the drift section and fills the gap volume around the super-container or distance block (see Figure 5-3) including:

• Compression of any trapped air.

• Loss of water to the partially saturated bentonite.

• Compression of water or water/bentonite gel.

• Compression of the fluid due to any swelling of the bentonite.

• Compression/deformation of the rock matrix and bentonite blocks (likely to be small if blocks fixed).
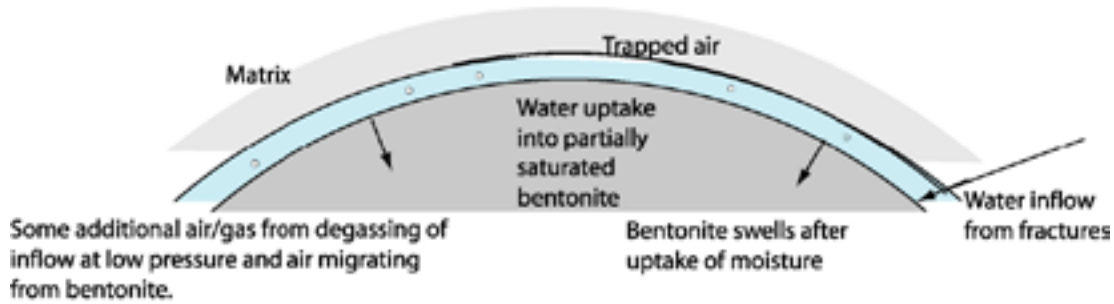
Figure 5-3. *Schematic of processes in annulus around super-container.*

These processes cannot be represented within the current model and their effect is lumped into a single storage term. The accessible pore volume associated with each drift element has been taken as the volume of open gaps around the super-containers and distance blocks, In order to address the parameter and conceptual uncertainties the following five cases have been used:

A) No storage associated with drift section – the only storage is associated with formation. This is equivalent to considering the super-containers and distance blocks as rigid inserts fitting perfectly into the drift.

B) Storage term calculated as water compressibility × accessible pore volume.

C) Storage term taken from Big Bertha distance block sealing tests /Börgesson et al. 2005/ with a factor 50 scale-up to account for larger gap volume and area around blocks.

D) Fixed volume compressibility model (Appendix G).

E) A model with an "unconfined" storage coefficient which switches to a confined value when the integrated inflow reaches the accessible pore volume.

Models A–C do not consider the filling of the accessible pore volume around the super-containers and distance blocks. Model A represents the fastest response (no filling of pore volume and no storage). The storage coefficients used in models C and E are scaled up from the Big Bertha experiments and must be associated with some significant uncertainty. In higher permeability intervals the effects of trapped air may be important while in low permeability intervals the water uptake into the bentonite will dominate. The details of models D and E are discussed below.

Storage model D

This model is based on that presented in Appendix G, which assumes a volume of trapped air within a rigid container. No account is taken of air dissolution, degassing or escape. Appendix G (op cit) gives the following relationship between pressure P (Pa) and inflow volume V (m³).

$$P(t) = \frac{P_o V_o}{V_o - V(t)} \tag{3}$$

Differentiating to calculate the storage coefficient (Pa/m³):

$$\frac{dP}{dV} = \frac{P_o}{V_0} \frac{1}{\left(1 - V/V_o\right)^2} \tag{4}$$

Note that $\frac{dP}{dV}$ increases with inflow volume as the air becomes compressed and pressurised. The parameters to the model are P_0 taken as 101.3 kPa and V_0 the volume to be filled (see Table 5-2).

Table 5-2. Storage coefficients for the five storage models as used in DFN Flow Model calculations. Model D depends only on the accessible pore volume.

	Accessible Pore volume	A	B	C	E
			Storage term m³/Pa		
Super-container	1.38	0.0	6.7×10^{-10}	1.0×10^{-7}	1.0×10^{-7}
Distance bock	0.08	0.0	3.9×10^{-11}	4×10^{-8}	4×10^{-8}
Distance block DAWE	1.38	0.0	6.5×10^{-10}	1.0×10^{-7}	10×10^{-7}
Bentonite blank zone	0.08	0.0	7.3×10^{-11}	4×10^{-8}	4×10^{-8}
Compartment plug stabilisation block	0.08	0.0	7.3×10^{-11}	4×10^{-8}	4×10^{-8}
Seal zone permeable fill	8.0		4.0×10^{-9}		
			/Domenico and Schwartz 1997/ (dense sandy gravel)		

Storage model E

A further variant was developed assuming a large compressibility while the open pore volume is being filled, and a lower compressibility after that. This model switches between an "unconfined" storage coefficient (calculated from the open pore volume and radius of the tunnel) and a "confined" storage coefficient given by storage model C

$$\frac{dV}{dP} = \frac{V_0}{2r_d \rho g} \qquad V < V_0$$

$$\frac{dV}{dP} = \text{Storage from Model C} \qquad V \geq V_0 \tag{5}$$

5.1.4 EDZ around drift

Studies for KBS-3H (Appendix D in /Johnson et al. 2005/) suggest that the Excavation Damage Zone will be a relatively thin zone (23 mm) of enhanced matrix porosity and permeability (2.96×10^{-19} m²). The inflow to a super container section from a transmissive feature at hydrostatic pressure through 1 m of EDZ would be approximately 1.3×10^{-5} l/min. This is less than 1% of the flow expected from a 10^{-10} m²/s fracture. The EDZ has not therefore been included within the transient flow models.

5.1.5 Flow through distance blocks and matrix

Assuming a saturated permeability of 10^{-20} m² the flow through a distance block from a super-container section at hydrostatic pressure to a section at atmospheric pressure can be calculated as 1.2×10^{-6} l/min. This is less than 0.1% of the flow expected from a 10^{-10} m²/s fracture. Flow through the distance block (which is in fact likely to be only partially saturated within the timescales of the transient models) has therefore been ignored and each drift section is treated as a disconnected element.

Assuming a transmissive fracture 1 m away from the drift and a matrix hydraulic conductivity of 10^{-14} m/s the inflow from the matrix to a super-container section at atmospheric pressure can be calculated as 1.1×10^{-5} l/min. This is less than 1% of the flow expected from a 10^{-10} m^2/s fracture. Flow through the matrix has therefore been ignored within the transient flow models.

5.1.6   Grouting model

Within the geometric models it was envisaged that all WCFs with average transmissivity greater than 2×10^{-8} m^2/s would be grouted. Within the DFN flow models a simple representation of grouting has been implemented. For all fractures within a given radius of the drift centre line r_{Grout} the local fracture transmissivity is set to the post-grout transmissivity T_{Pgrout} if the local fracture transmissivity is greater than the threshold T_{Grout}. Suggested values for the parameters are listed below: The transient response to closure assuming a storage of 3.8×10^{-8} m^3/Pa as calculated using the single fracture nSights model is shown in Figure 5-4.

5.1.7   Representation of excavation and emplacement schedule

In order to represent the progressive excavation of the drift and emplacement of super-container, distance blocks etc time varying boundary conditions were applied to each element of the drift representation. Initially all elements were set as zero flow (no production or injection – although some limited cross-flow was allowed, but this was small due to low axial permeability of the elements). The boundary conditions were switched to fixed zero head (relative to drift centre line at 400 mbgl) at the time calculated for the start of the excavation of that element. Emplacement schedules have also been calculated based upon the information provided in the design description /Autio 2006/ which have been updated for changes in the design of the compartment plugs.

In order to represent the progressive emplacement of the super-containers, distance blocks and compartment plugs, the boundary conditions were changed from zero head to zero flow. A simple schedule was developed for each drift realisation. All times are rounded to the nearest hour to simplify management of computation time-steps. The boundary conditions within the models were changed from open tunnel (fixed zero head) to closed (zero flow to drift element) when the next distance block, blank zone or plug element is emplaced, thus free flow continues into each super-container drift element until the sealing distance block is emplaced, when the drift elements for both the super-container and distance block are set to zero flow.

For the DAWE concept emplacement schedules have been assumed to be similar to those used for the basic design. The closure schedule is different as the drifts remain open to flow until they are filled prior to sealing of the compartment plug or drift end plug. The excavation and emplacement schedule for a drift (Drift W01T23) is shown in Figure 5-5. The drift contains a high transmissivity feature that requires a compartment plug at about 215 m and the time taken to emplace the compartment plug elements are shown in the figure as is the difference in drift closure schedules for the basic design and DAWE.

Table 5-3. Simple grouting model parameters used in this study.

Parameter	Value	Comment
T_{Grout}	2×10^{-8} m^2/s	Threshold for grouting – corresponds to bentonite block or compartment plug dependent on transmissivity.
T_{Pgrout}	5×10^{-9} m^2/s	Selected so that inflow for fractures >> 2×10^{-8} m^2/s is equivalent to inflow from 2×10^{-8} m^2/s ungrouted fracture.
r_{Grout}	2.925 m	Assumption 2 m thick grout fill in transmissive fractures.
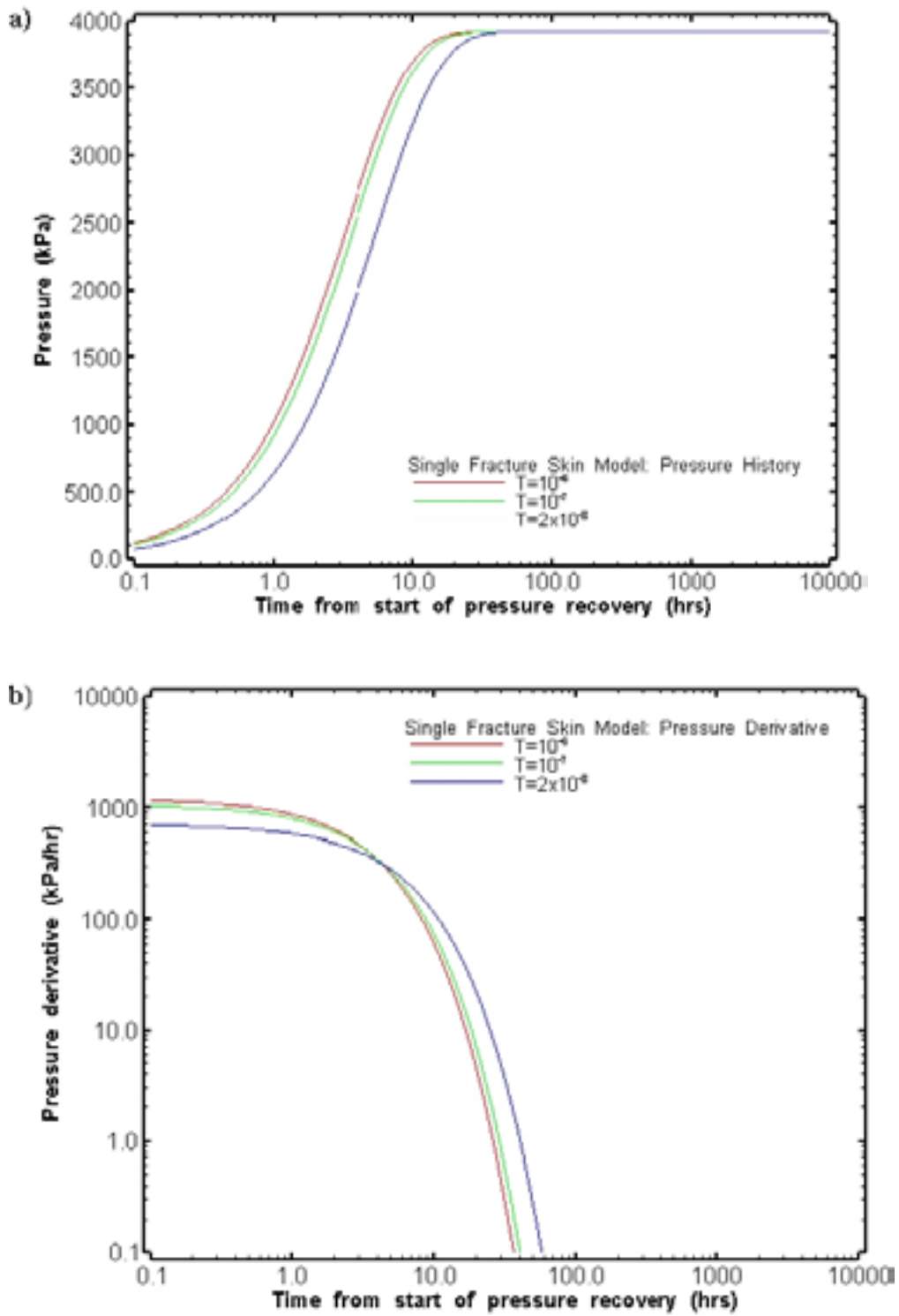
Figure 5-4. *Effect of grouting model for a single fracture model. a) pressure recovery and b) pressure derivative from nSights well test simulator.*
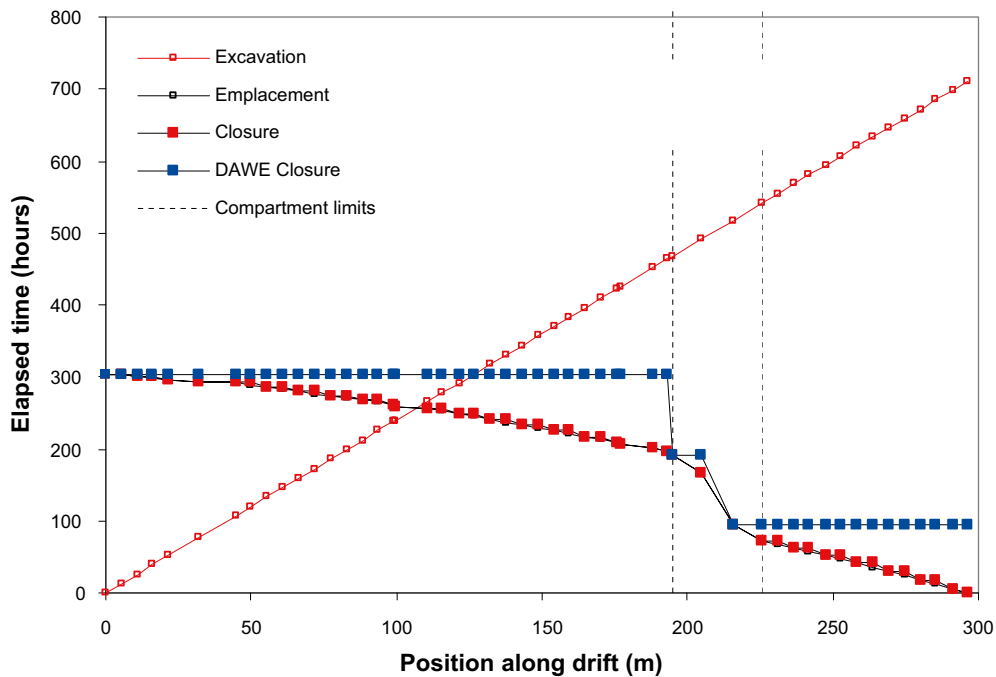
Figure 5-5. *Excavation and emplacement schedule for drift elements in Drift W01T23 for both reference and DAWE concepts.*

5.1.8 Outputs from models

The outputs derived from the transient flow models are:

- Pressure at feature intersections with drift elements.
- Pressure derivative (kPa/hr) at feature intersections with drift elements.
- Net in/outflow to each intersection on a drift element.
- Net in/outflow to each drift element (note not flow through the element).
- Integrated net inflow to each drift element.

These outputs are calculated at each time-step. Typically excavation and emplacement runs use 1,000–3,000 time-steps. The time-steps are chosen for each run to account for the number of events (excavation/emplacement steps) and the diffusivity of the feature elements. The outputs were tabulated in Excel spreadsheets for each model run.

It is important to note that flow through the EDZ, matrix and EBS along the drift are not included in the models (see previous discussion in this section). Table 5-5 compares the estimated inflow due to fracture elements with those from the EDZ, matrix and EBS. It can be seen that even a fracture of transmissivity 10^{-11} m^2/s can produce significantly more inflow than these features. Given the timescale for simulation of 1 year and that most models consider only fractures greater than 10^{-10} m^2/s, it is clear that the contribution from flow through the matrix, EDZ and EBS are insignficant for the flow models considered here.

5.2 Transient flow models

The results discussed here are for four drifts: W01T01, W01T12, W01T22 and W01T23 in panel 1 of the western section of the repository taken from the first realisation used in the geo-metric models. The drifts were selected purely on the number of compartments and the desire to consider interference between drifts during excavation.

Table 5-4. DFN Flow Model Features.

Feature	Representation in DFN flow models
Model region	Single drift models: 400 m long, 100×100 m cross-section rectangular block around deposition drift.
	Two drift models: 400 m long, 125×100 m cross-section rectangular block around deposition drift.
Geosphere representation	Selected realisations from Extended Reference Case geosphere representation. Only features with transmissivity > 10^{-10} m²/s included (variant cases where features with transmissivity > 10^{-11} m²/s included).
Emplacement drift	1-D elements representing 300 m drift with super-containers, distance blocks, blank zones and compartment plugs.
Transport tunnels and other excavations	Not included.
Outer boundary condition	Fixed 400 m (relative to drift centre line) head on all model outer surfaces.
Drift boundary conditions	a) fixed zero head (relative to drift centre line) to represent open drift. b) closed zero net flow condition to represent closure of drift section after emplacement.

Table 5-5. Inflow and estimated time to fill super-container gap volume (1.38 m³) for different features.

Flow Feature	Transmissivity (m²/s)	Inflow (l/min)	Fill time (years)	In model	Inflow Calculation
Fracture	2.65×10^{-09}	1.0×10^{-01}	0.03	In model	Inflow from single fracture hydrostatic boundary at 50 m
Fracture	1×10^{-10}	3.8×10^{-03}	0.69	In model	Inflow from single fracture hydrostatic boundary at 50 m
Fracture	1×10^{-11}	3.8×10^{-04}	6.94	Not in all models	Inflow from single fracture hydrostatic boundary at 50 m
	Hydraulic conductivity (m/s)	**Inflow (l/min)**	**Fill time (years)**	**In model**	**Inflow Calculation**
Matrix	1×10^{-14}	1.1×10^{-05}	229.35	Not in models	Inflow from matrix hydrostatic constant head boundary at 1 m from tunnel wall
EBS Along Tunnel	1×10^{-13}	1.2×10^{-06}	2,175.88	Not in models	Inflow from pressurised super-container through distance block
EDZ Along Tunnel	3×10^{-12}	2.4×10^{-06}	1,100.32	Not in models	Inflow through EDZ around DB from hydrostatic super-container section

W01T01 and W01T02 are single compartment drifts while W01T22 and W01T23 each include two compartments isolated by a compartment plug. Plots of pressure, pressure derivative and inflow have been produced using the following colour scheme

- Black: super-container drift elements.

- Green: distance block drift elements.

- Orange: blank zone drift elements.

- Red: compartment plug drift elements (dashed for sealing elements, solid for permeable fill element of compartment plug).

The positions along the drift of each type of element are shown in Figure 5-6.
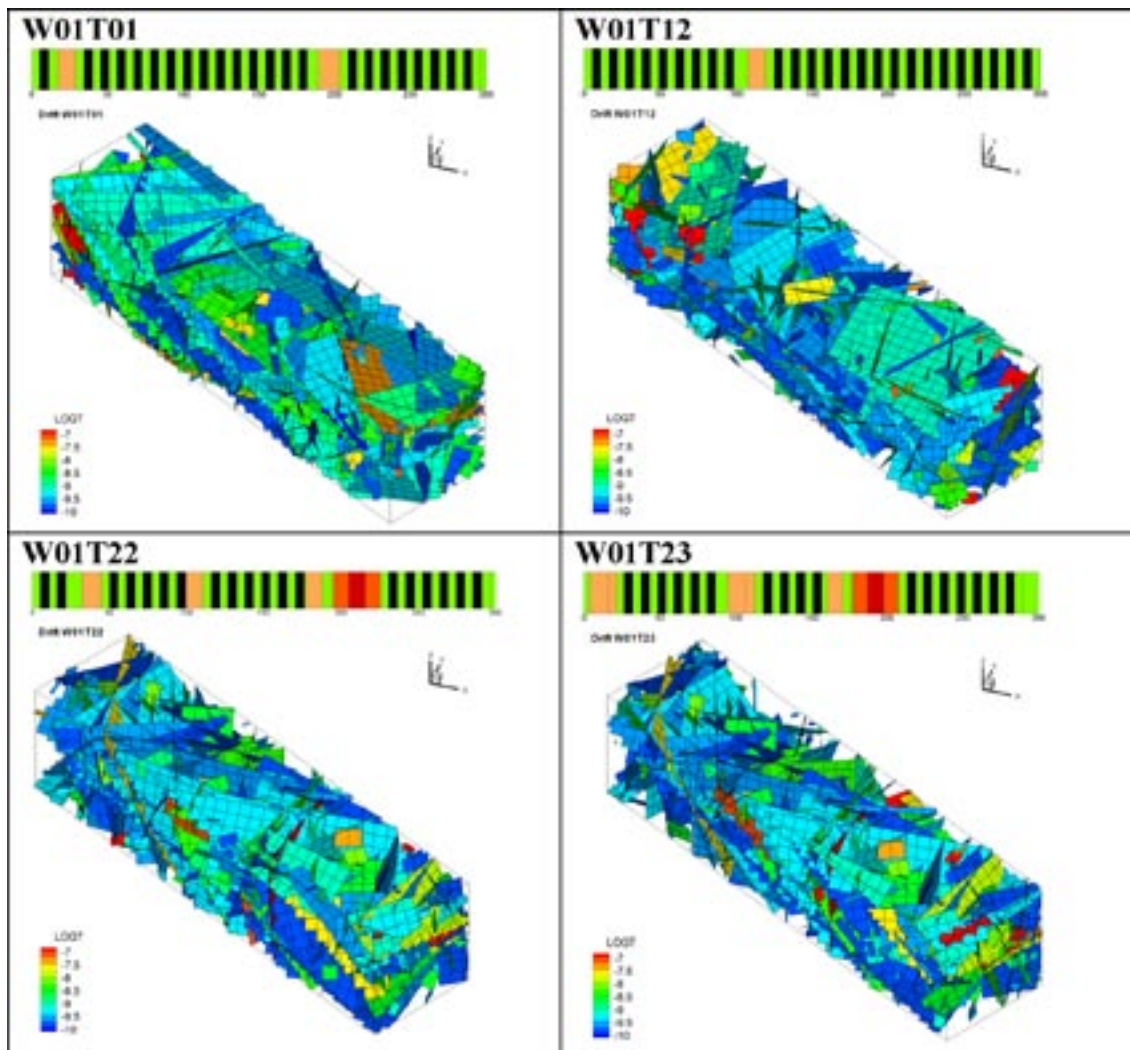
Figure 5-6. *Drift layouts and DFN models for the four drifts. Layout follows plot colour convention.*

5.2.1   Simulation of excavation

The calculated inflow versus time for the four drifts are shown in Figure 5-7. The timing of the inflows relate to the positions of the features along the drift assuming a 10 m/day advance rate. Typically inflow has stabilised within a few days of the last inflow encountered. Peak inflows occur as the largest inflow is penetrated by the drift and may be 2–3 times the stabilised flow. The calculated peak inflow rate is related to the timestep used in the simulations which is usually 200 seconds during the early parts of transients related to excavation and emplacement.

A variant where it has been assumed that all features with transmissivity greater than 2×10^{-8} m^2/s have been pre-grouted for drift W01T22 where a high transmissivity feature is encountered at about 215 m along the drift (21 days after start of excavation) is shown in Figure 5-8. The total inflow is significantly reduced as would be expected (by about a factor of 4). The low transmissivity finite elements in the grouted region required a larger time-step for numerical stability so the height of the peak flow is slightly reduced due to the lower time resolution.
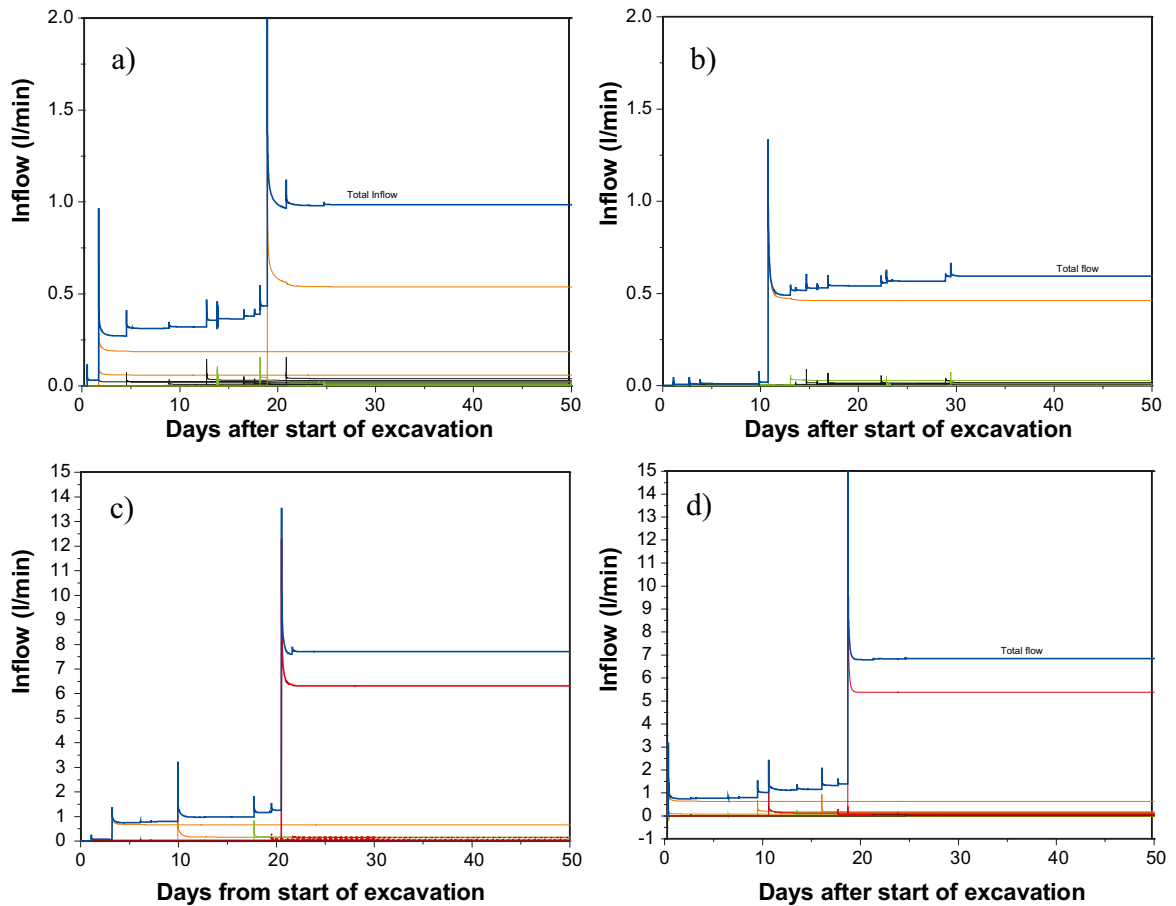
Figure 5-7. *Calculated inflow (l/min) versus time (days) for drifts. a) W01T01, b) W01T12, c)W01T22 and d)W01T23. Note higher rates in drifts W01T22 and W01T23 which require compartment plugs. Plots follow standard convention lines for super containers in black, distance blocks in green, blanks zones in orange and compartment plugs in red. Total inflow shown in blue.*
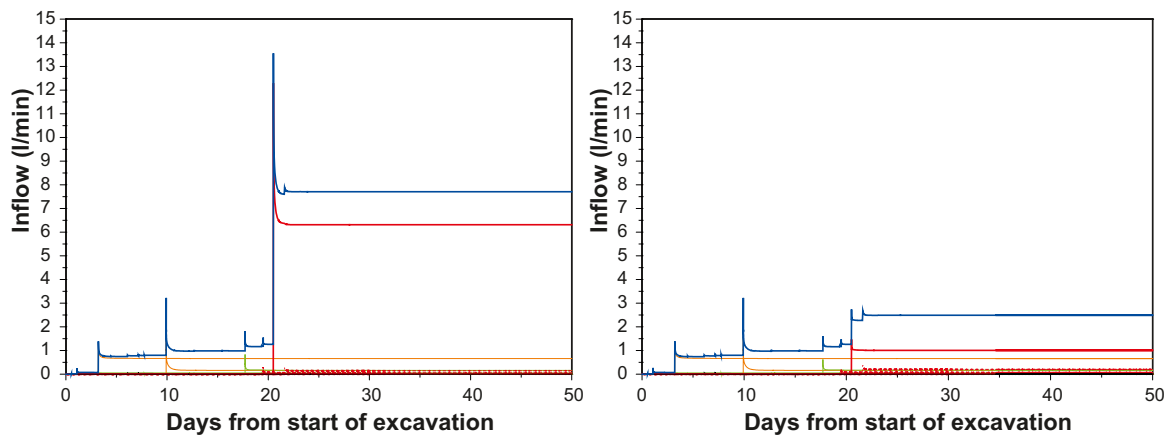
Figure 5-8. *Calculated inflow (l/min) versus time (days) for drift W01T22. a) without pre-grouting, b) with pre-grouting (see previous chapter). Note lower time resolution in grouted model may have reduced height of inflow spike.*

5.2.2 Basic design: Single compartment drifts

Influence of different storage models

Figures 5-9, 5-10 and 5-11 show the pressure, pressure derivative and inflow for each drift element after emplacement for the different storage models for drift W01T01. There is very little difference between storage models A and B showing that storage terms have to be significantly greater than that due to water compressibility before there is any real change in behaviour. Model C shows the effect of assuming higher storage with a much extended pressure recovery and inflow continuing until pressure has reached equilibrium. Models D and E show the delay due to the filling of the accessible pore volume.
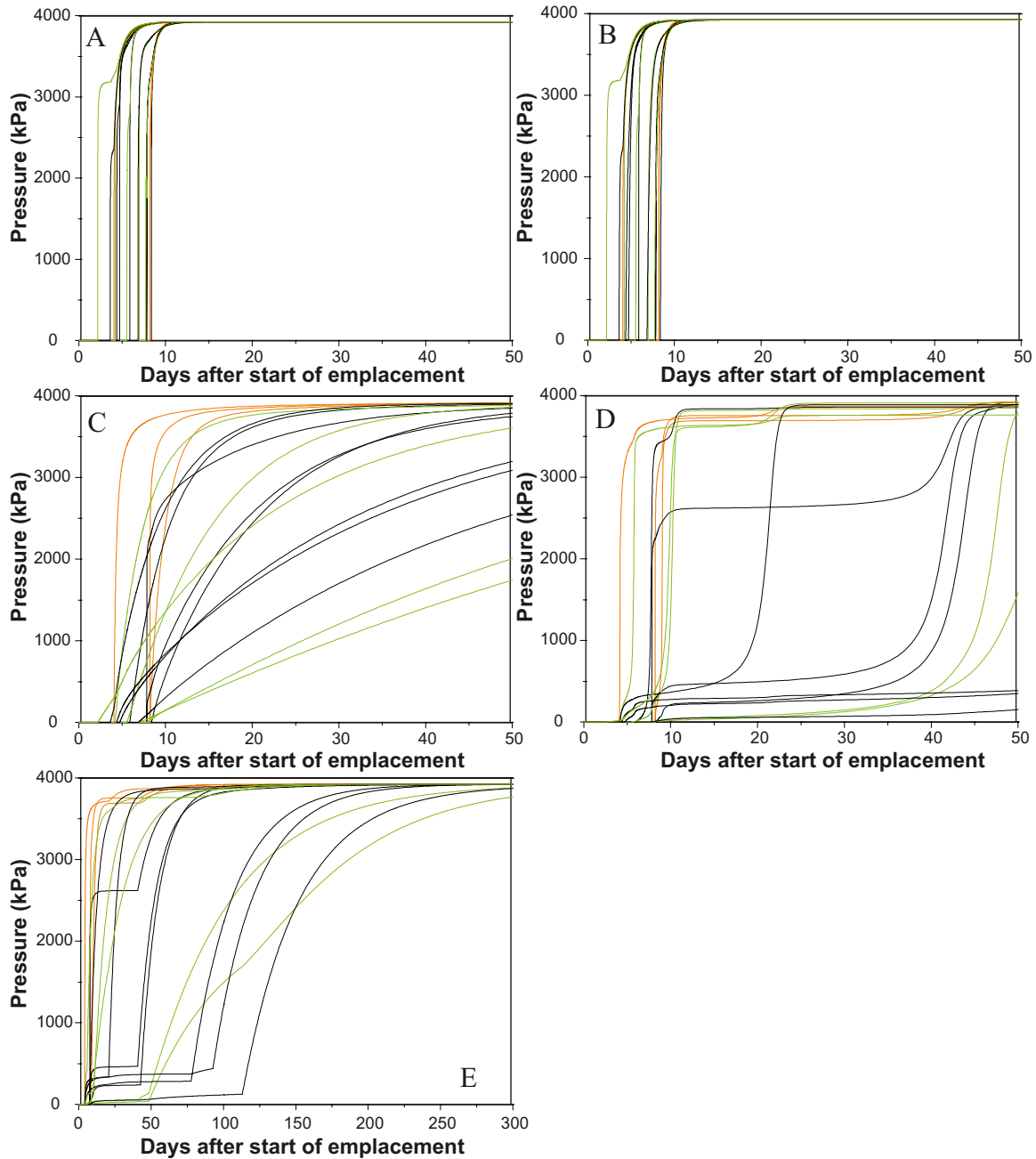
Figure 5-9. *Pressure at feature intersections after emplacement for different models. Plots follow standard convention: lines for super containers in black, distance blocks in green, blanks zones in orange and compartment plugs in red.*
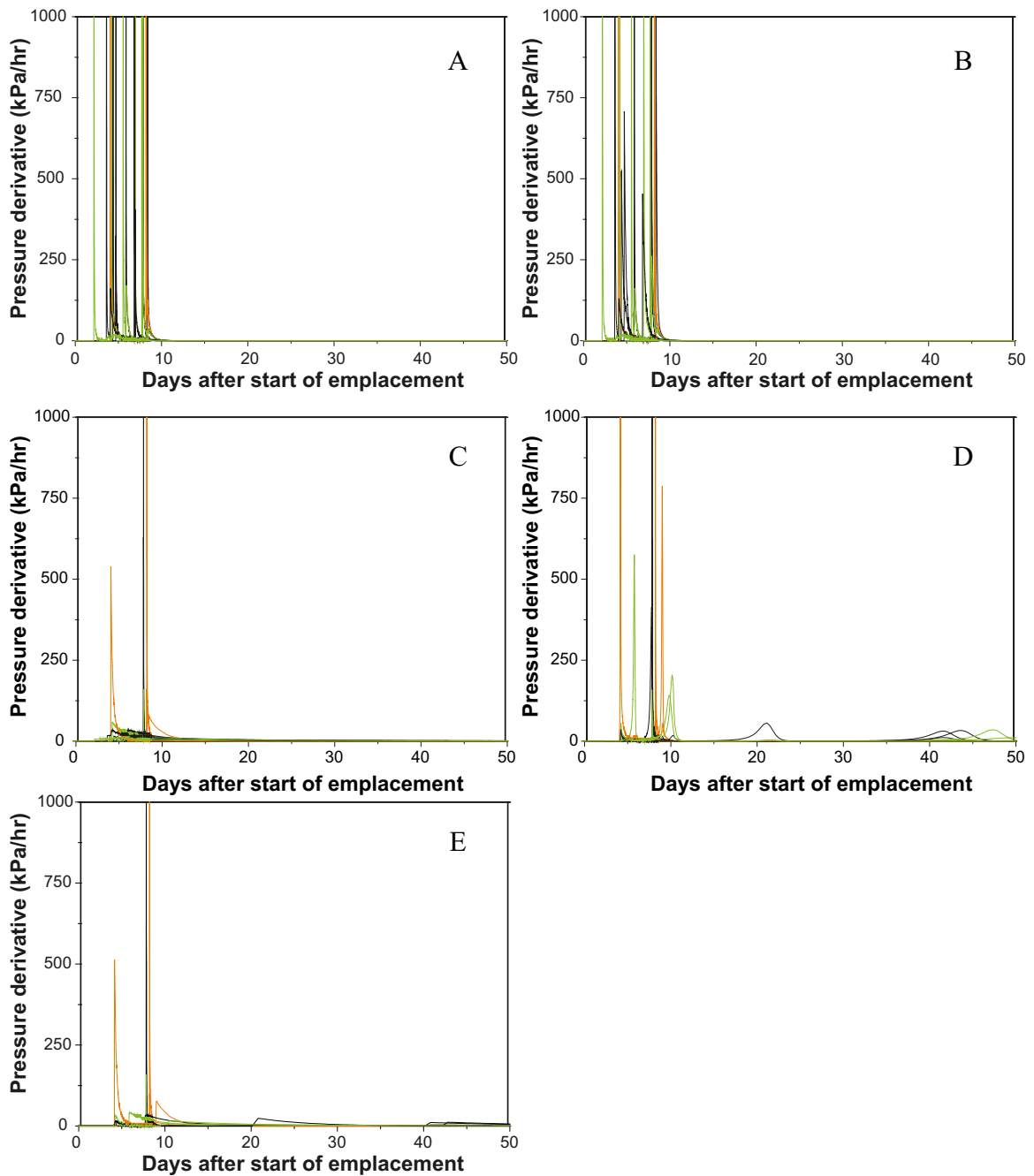
Figure 5-10. *Pressure derivative (kPa/hr) at feature intersections after emplacement for different storage models. Plots follow standard convention: lines for super containers in black, distance blocks in green, blanks zones in orange and compartment plugs in red.*

The values of pressure derivative are controlled by the storage coefficient and inflow rate. High values > 1,000 kPa/hr occur for low or zero storage drift elements and high inflow rates. Typically these occur early in the emplacement period in all the models as high inflow rates result in rapid filling of any accessible pore volume. Pressure derivatives greater than 100 kPa/hr do not occur after about 10 days from the start of emplacement.

Figure 5-11 shows the inflow to drift elements intersecting features for the different storage models for drift W01T01. All models show slight increases in inflow prior to closure as flow is diverted from other drift sections that are becoming pressurized, typically this results in at most a factor two increase in flow. The storage models with zero (model A) or low (model B) storage values show an immediate drop in inflow on closure. Model C shows a decline in flow as pressure rises. In models D and E the effect of the fill volume is seen as a delay in pressurization.
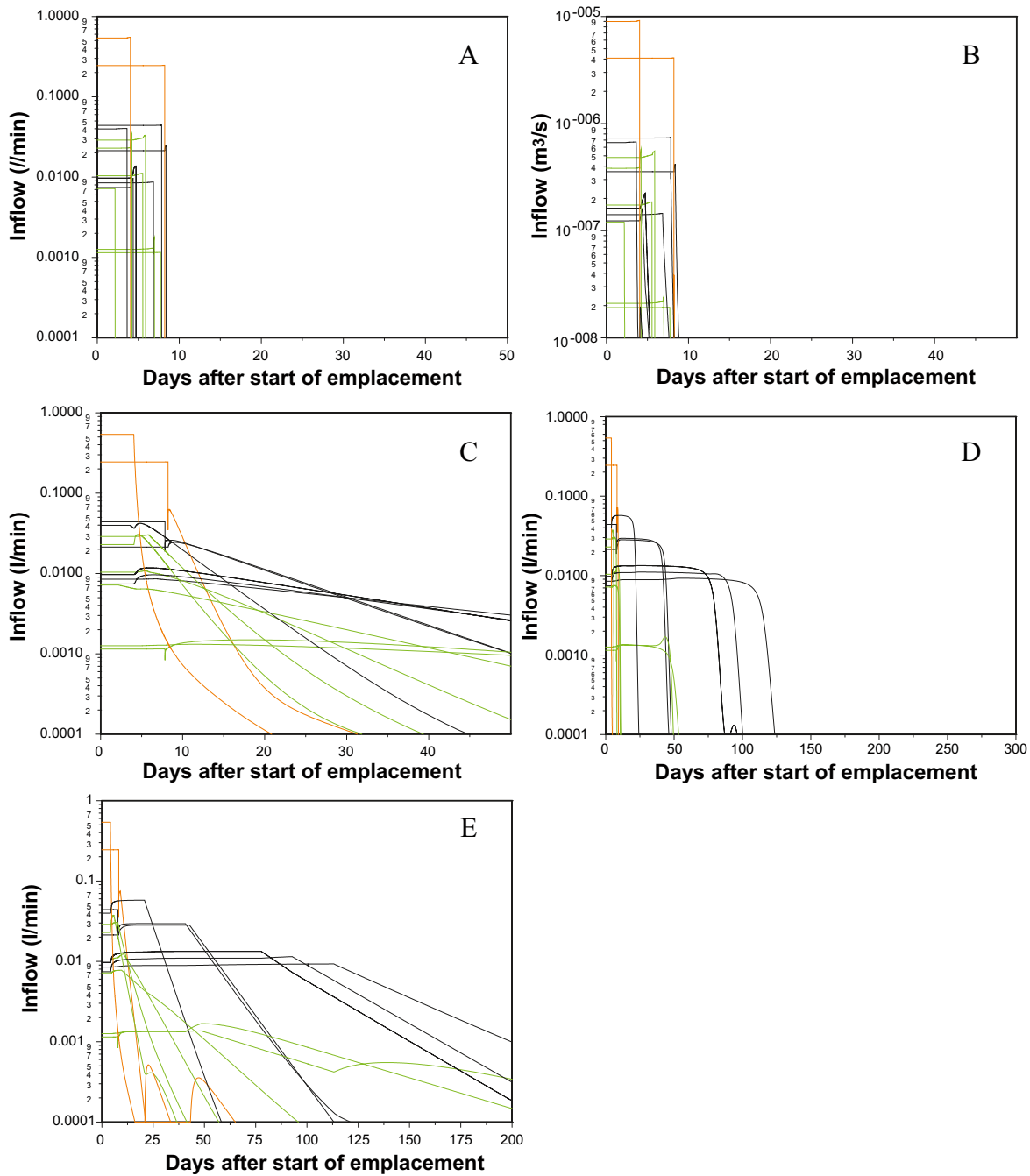
Figure 5-11. *Inflow (l/min) to drift elements for different models (all for drift W01T01).*

The inflow for model E shows some minor oscillations in inflow ($> 10^{-3}$ l/min) in late time due to changes in time steps, these are not evident in the other models as time-step changes were synchronised with changes in the model boundary conditions. This was not possible with the model E where there is a delay due to the time required to fill the accessible pore volume.

It is important to note that the figures above show only the response in drift sections intersected by transmissive features. The majority of sections intersect only low transmissivity features. In such drift sections any water inflow will be taken up by the bentonite and no pore pressure will develop until the gap volume is sealed by the swelling bentonite. To illustrate this Figure 5-12 shows the maximum pressure within a drift element for the Storage Model D runs for W01T01, W01T12, W01T22 and W01T23.
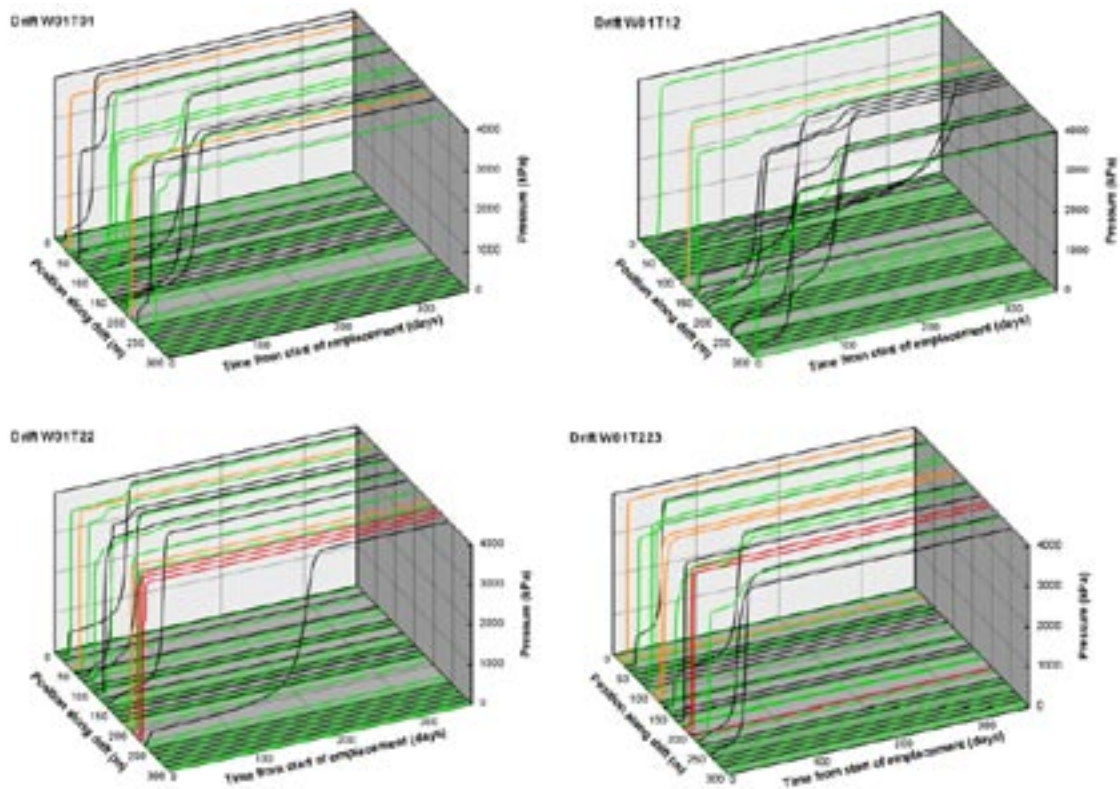
Figure 5-12. *Maximum pressure in drift elements versus time for the four model drifts using Storage Model D – Transmissivity cutoff of 10^{-10} m^2/s.*

Effect of including lower transmissivity features

The base models have considered only feature within the geosphere representation that have transmissivity > 10^{-10} m^2/s. This threshold has been used to limit the numerical cost of simulation. The inclusion of features with transmissivity between 10^{-11} and 10^{-10} m^2/s results in a threefold increase in fracture elements within each drift model from about (6,500 to over 20,000) and a factor 10 increase in computation time. Additional low transmissivity features may influence the numerical performance of the code, by showing instability at short time steps and requiring higher discretisations (due to the assumption of piecewise linear pressure behaviour along fracture intersections).

A small number of model runs have been performed including the low transmissivity fractures to check that they do not significantly alter the results. Figure 5-13 shows the calculated inflows to drift elements for models with and without features with transmissivity between 10^{-11} and 10^{-10} m^2/s. There is no significant difference in the behaviour of the higher inflows caused by inclusion of the low transmissivity features.

Figure 5-14 shows the maximum pressure for the different drift sections for W01T01 model C.
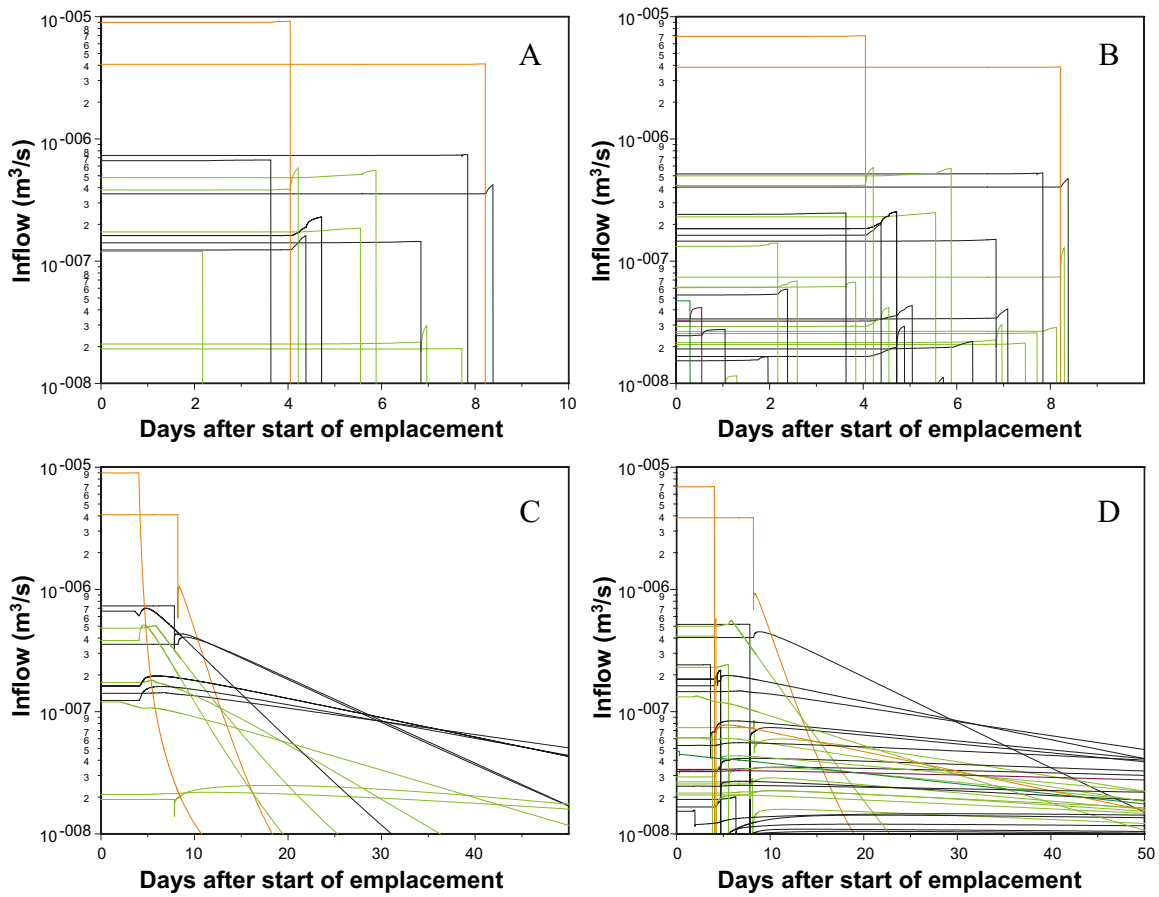
Figure 5-13. *Calculated inflow during emplacement for drift W01T01 for storage models A and C for cases without and including low transmissivity features. a) storage model A without low transmissivity fractures, b) storage model A including fractures with T between 10^{-11} and 10^{-10} m²/s, c) storage model C without low transmissivity fractures, d Storage model C including fractures with T between 10^{-11} and 10^{-10} m²/s.*
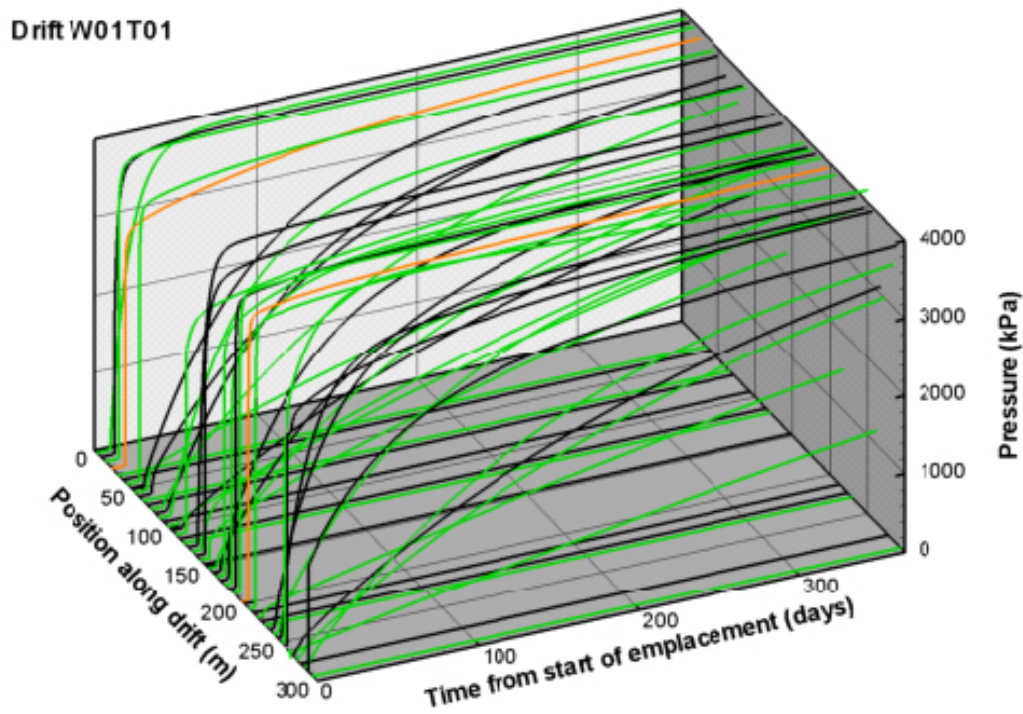
Figure 5-14. *Maximum pressure in drift elements versus time for the W01T01 using Storage Model C, minimum transmissivity 10^{-11} m²/s.*

5.2.3 Basic design: Drifts with two compartments

The models for W01T22 and W01T23 show the response for drifts with two compartments. Figures 5-15 to 5-17 show the pressure, pressure derivative and inflow to drift elements for the different storage models. The major differences relate to the choice of storage model. There is no significantly greater deflection of flow into the compartments due to the presence of the high transmissivity feature and associated compartment plug. Pressures show a more step like behaviour (particularly in storage model A) perhaps due to the longer plug emplacement period and the influence of the high transmissivity feature.
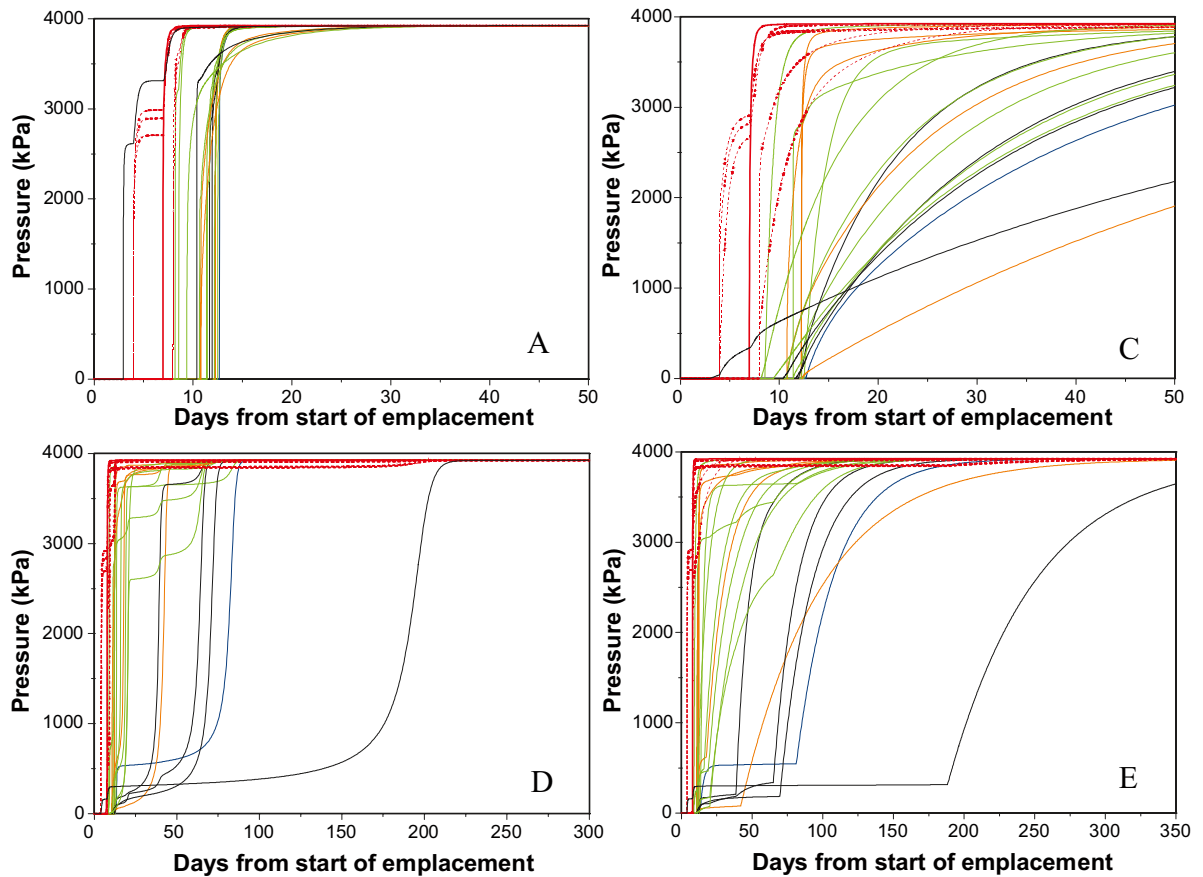
Figure 5-15. *Pressure response during emplacement for different storage models (A,C,D,E) for drift W01T22.*
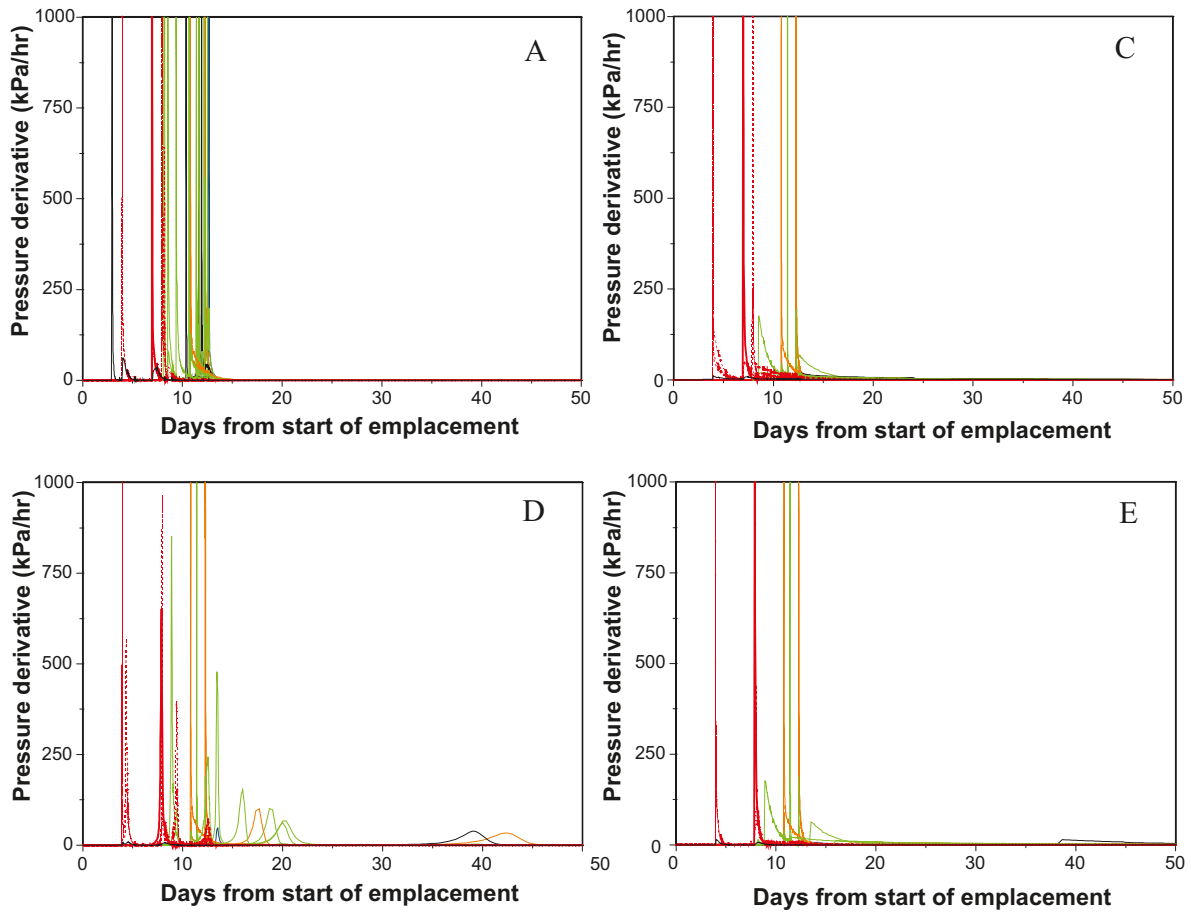
Figure 5-16. *Pressure derivative (kPa/hr) during emplacement for different storage models for drift W01T22.*

Pressure derivatives are again strongly influenced by storage model, but all models show very high derivatives in the compartment plugs, blank zones and some distance blocks. Inflows show some diversion of flow from the higher transmissivity feature after sealing into other drift elements but again this is small (maximum factor of 2).
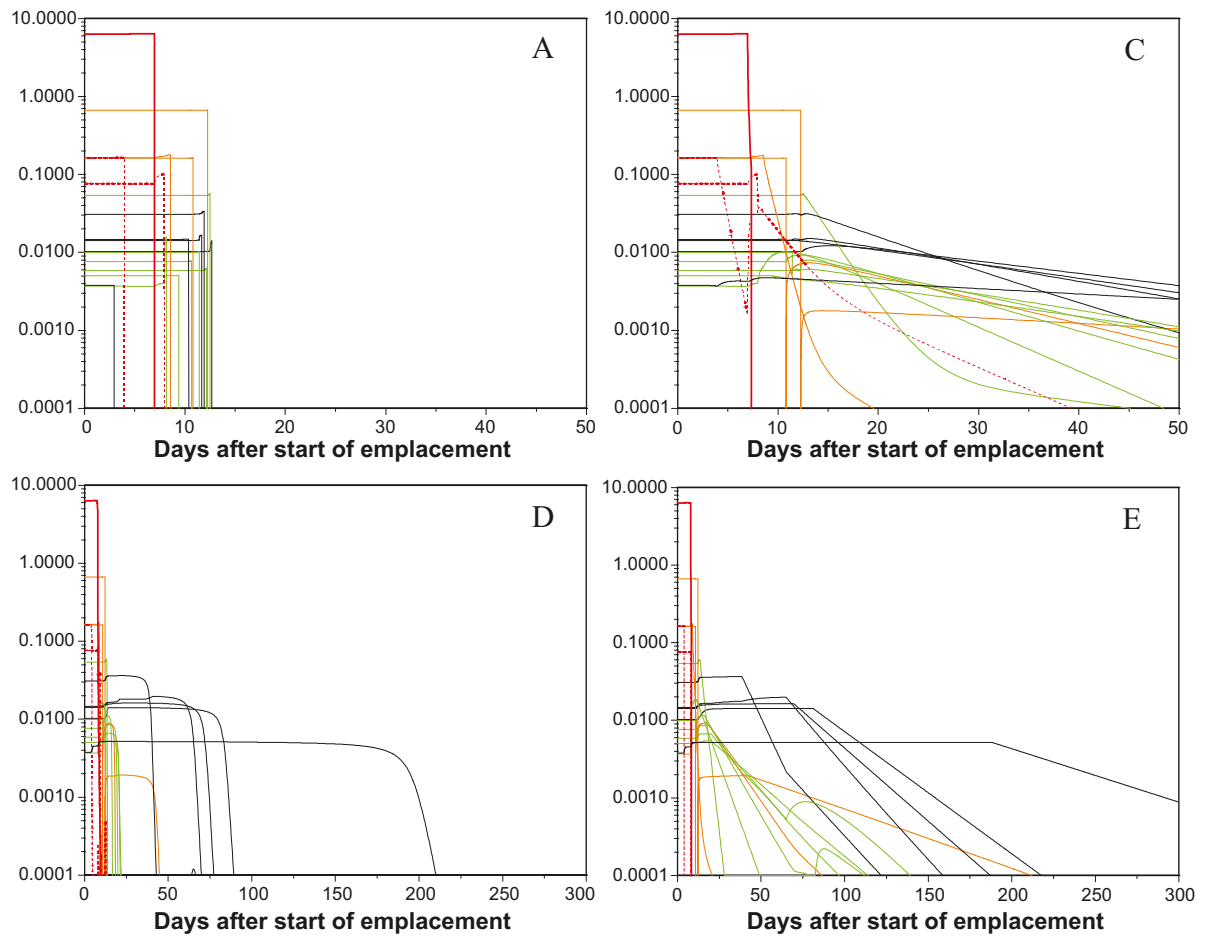
Figure 5-17. *Inflow (l/min) during emplacement for different storage models for drift W01T22.*

Figure 5-18 illustrates the pressure recovery around the drift after emplacement for W01T22 storage model D. The low pressure features remain around super-container sections 1, 4, 5, 9 and 14 due to the low inflow to these sections (the slowly reacting pressure in these sections can be seen in Figure 5-15). Sections shown in grey are not intersected by a fracture and hence do not have a head calculated for them. The pressure in these sections will also be low (no significant inflow).

a) 0 days

b) 5 days

c) 10 days

e) 55 days

Head (m)

0.0   100.0   200.0   300.0   400.0
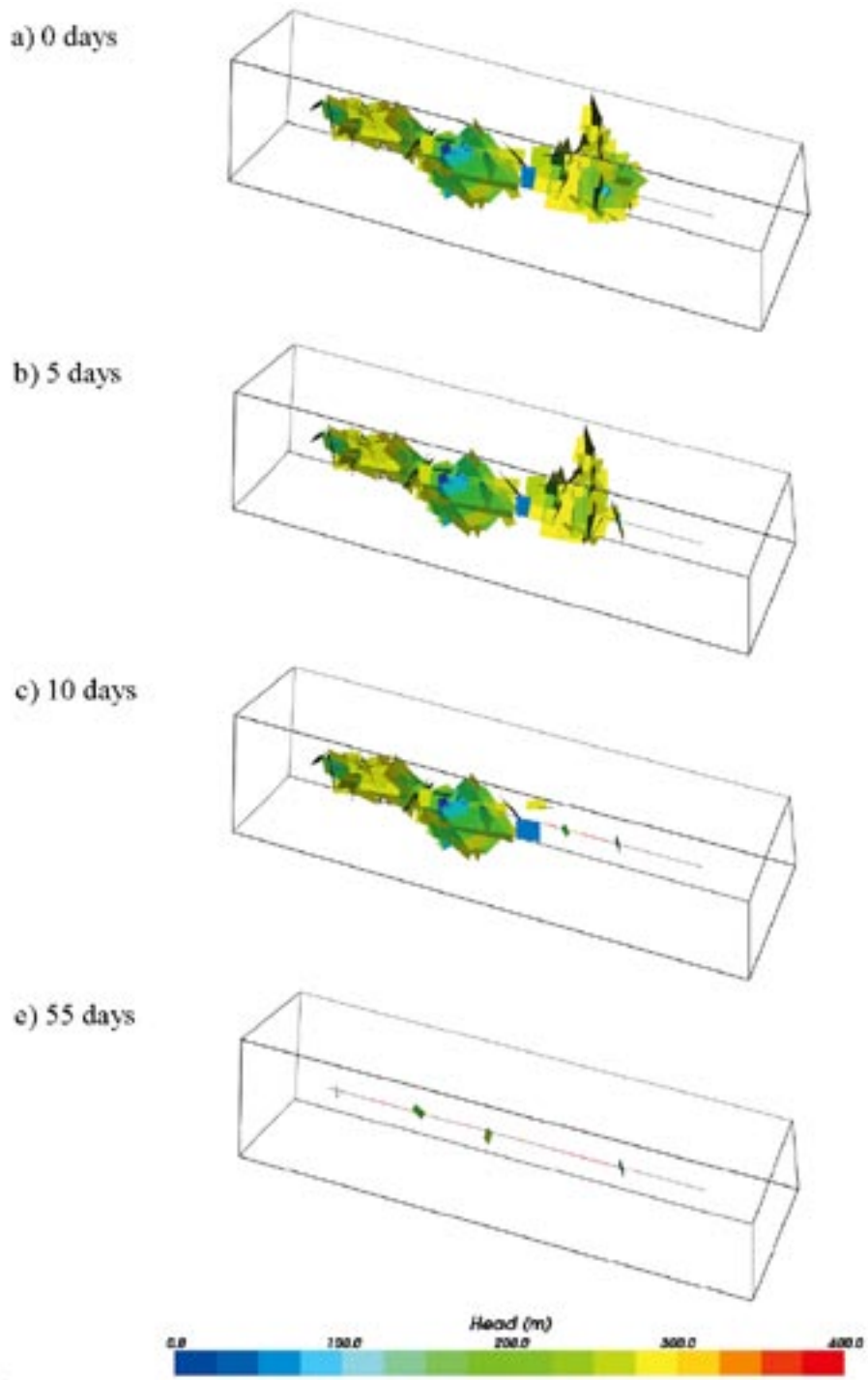
Figure 5-18. *Drawdown region around drift W01T22 storage model D. Only features with average head less than 300 m shown. Drift sections that do not intersect fractures shown as grey.*

74

5.2.4 Time to fill super-container gap volumes

One of the requested inputs was the time to fill the accessible pore volume around the super-containers. This has been calculated from the storage model E runs as models A–C assume that the gap volume is already filled and in model D there is always some remaining air. Only about 28% of the super-containers intersect features where transmissivity is greater than 10^{-10} m²/s. The remaining super-containers will saturate more slowly. Assuming the remaining super-containers are intersected by a 10^{-10} m²/s fracture we would expect the volume to fill in approximately 254 days (assuming radial flow to a hydrostatic boundary at 50 m radius from the drift).

Continuum two-phase flow calculations (see Figure 5-19) indicate that for geosphere hydraulic conductivity below 10^{-11} m/s (equivalent to a 5×10^{-11} m²/s fracture in a super-container section) the bentonite saturation time is a function of geosphere hydraulic conductivity. The time to fill the accessible pore volume for such low hydraulic conductivities is therefore a function of both water inflow and water uptake by the bentonite. For higher geosphere hydraulic conductivity, saturation time was independent of geosphere hydraulic conductivity and was controlled by the bentonite properties. Typical saturation times were 10 years for distance blocks and about 4 years for super-containers (smaller thickness of bentonite to saturate). Note that the saturation times shown in Figure 5-19, will be a function of the initial conditions of the bentonite material in particular initial water content and dry density.

Table 5-6. Days to fill accessible pore volume around super-containers in single drift models. All models use storage model E.

Drift	Number of super-containers	Number inter-sected by features in model	Days to fill accessible pore volume (1.38 m³) from start of emplacement		
			Minimum	Average	Maximum
W01T01	23	6	20	64	112
W01T12	25	9	50	157	365
W01T22	19	5	38	88	188
W01T23	17	4	44	56	89
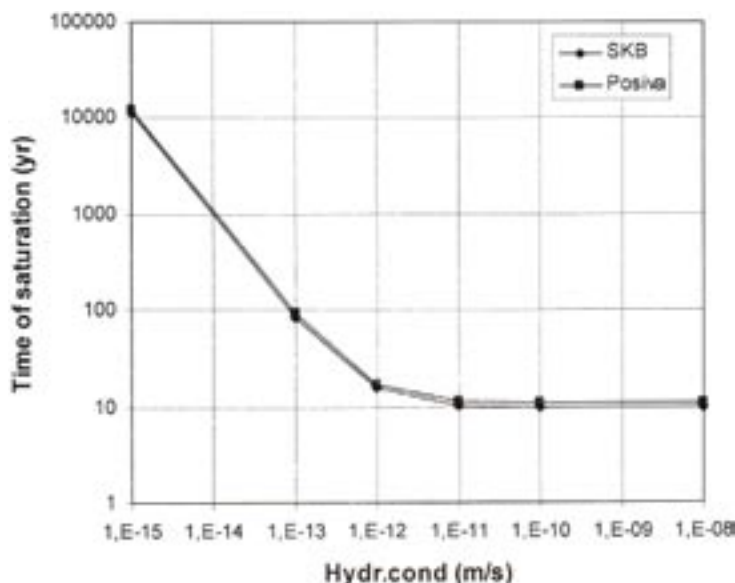
Figure 5-19. *Time to saturation versus hydraulic conductivities /from Börgesson et al. 2005/.*

5.2.5 DAWE concept

The main differences between simulations for the DAWE concept and the Basic Design are:

- Gap volumes are filled and air evacuated prior to closure (storage models D and E not appropriate for DAWE).

- Closure (shut-in) of compartment as a whole rather than closure after each distance block.

- Higher storage for distance blocks in storage model C.

Models were run using storage models A and C for drifts W01T01 (single compartment) W01T22 (two compartments) and the results are presented in Figure 5-20.

The major differences in response between the DAWE and Basic Design models are in the different timings of closure and hence of differential pressure between drift sections.

5.2.6 Two drift models

A specific request from the Process and Evolution report team was for models that considered the influence of excavation of a drift on a neighbouring drift where waste had been emplaced (see Figure 1-1). A model containing drifts W01T22 and W01T23 was developed as these two drift realisations are linked by a transmissive feature requiring a compartment plug in each drift. The fracture network around the two drifts is shown in Figure 5-21. Two scenarios were considered i) where waste has already been emplaced in W01T22 when drift W01T23 is excavated and ii) where W01T23 is excavated before emplacement and remains open while waste is emplaced in W01T22. The two scenarios are discussed in the following sections.
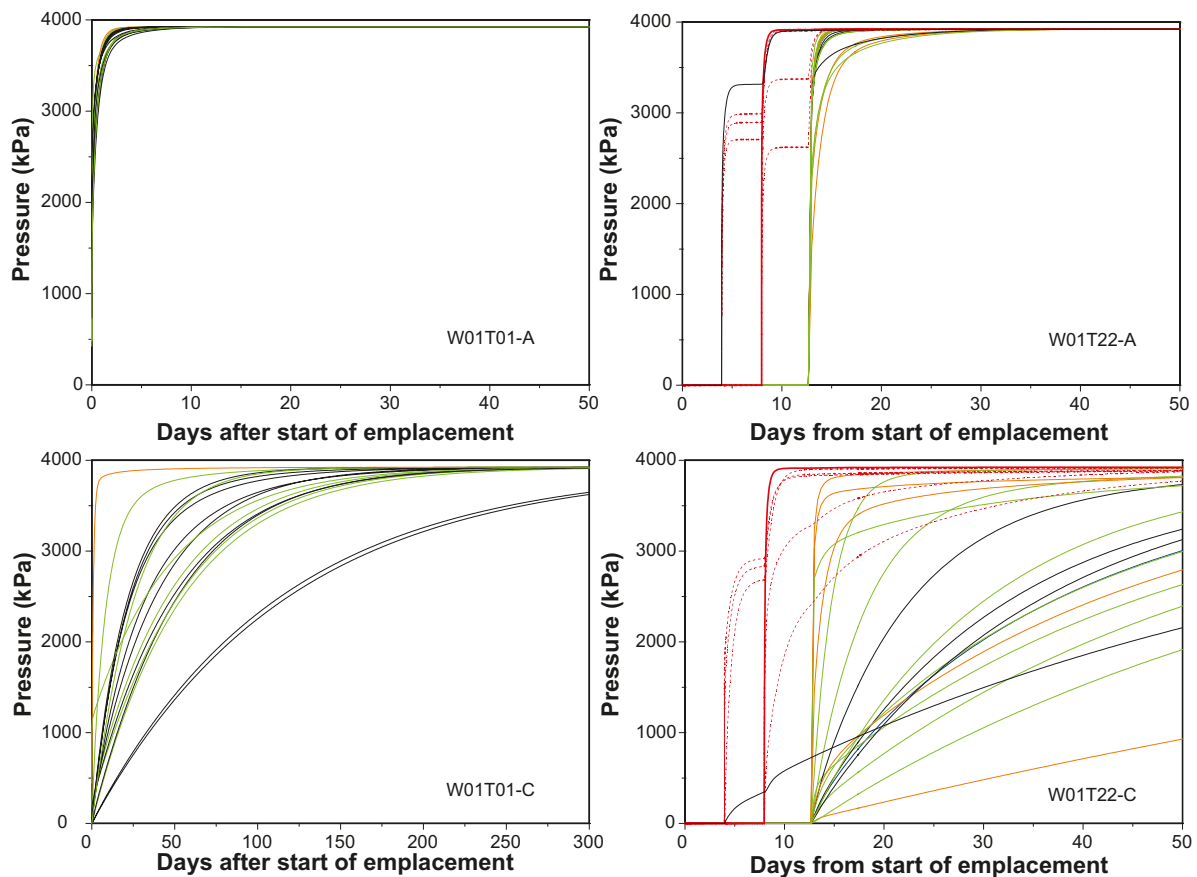
Figure 5-20. *Inflow (l/min) during emplacement for different storage models for drift W01T01 and W01T22.*
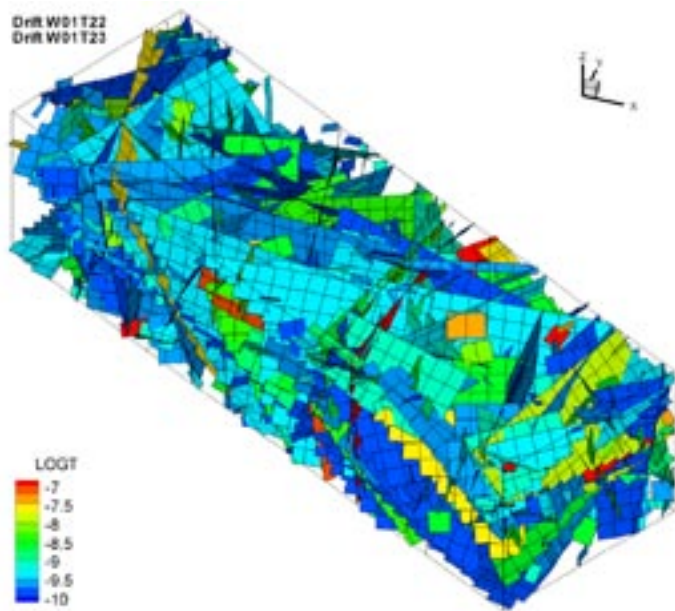
Figure 5-21. DFN realisation around drifts W01T22 and W01T23. Fractures coloured by log₁₀ transmissivity.

5.2.7 Effect of excavation of an adjacent drift on a closed drift

This section covers the models where waste has been emplaced in W01T22 when W01T23 is excavated. The simulations were performed for storage models A and C as it was assumed that the accessible pore volume had already been filled so that models D and E were not relevant. Figure 5-22 shows the pressure at feature intersections with W01T22 during the excavation of W01T23. There are fast pressure drops associated with the most permeable features (blank zones and compartment plugs) although some well connected features around distance blocks also undergo a significant pressure drop. The influence of the storage model is in the speed of pressure drop and the length of the associated transient.

Pressure derivatives are plotted in Figure 5-23 and the inflow during excavation to W01T23 is shown in Figure 5-24. The inflow is very similar to that shown in Figure 5-7 indicating that there is no significant change in response due to the different boundary conditions and presence of the adjacent drift.
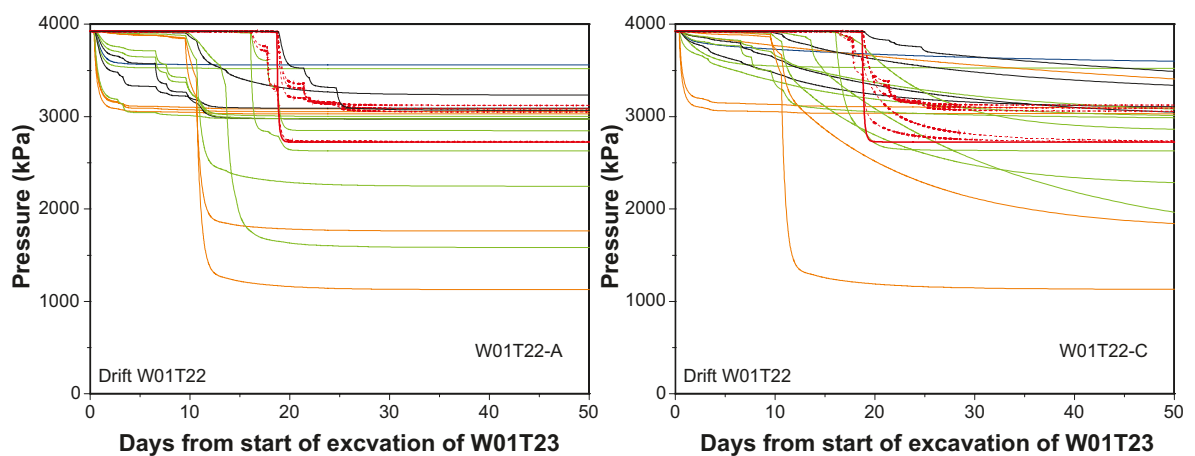
Figure 5-22. Pressure at feature intersections in W01T22 during excavation of W01T23 for storage models A and C.
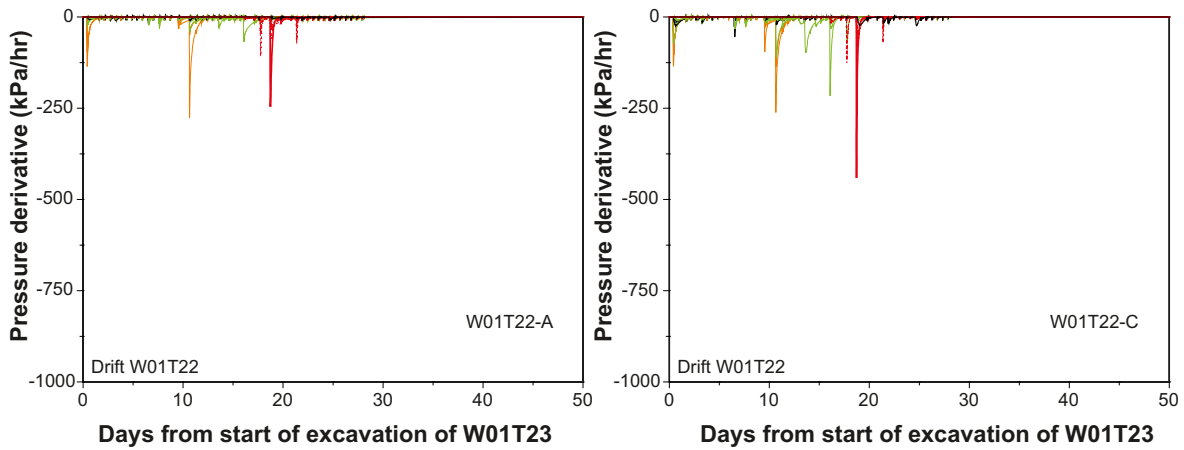
Figure 5-23. *Pressure derivative (kPa/hr) at feature intersections in W01T22 during excavation of W01T23 for storage models A and C.*
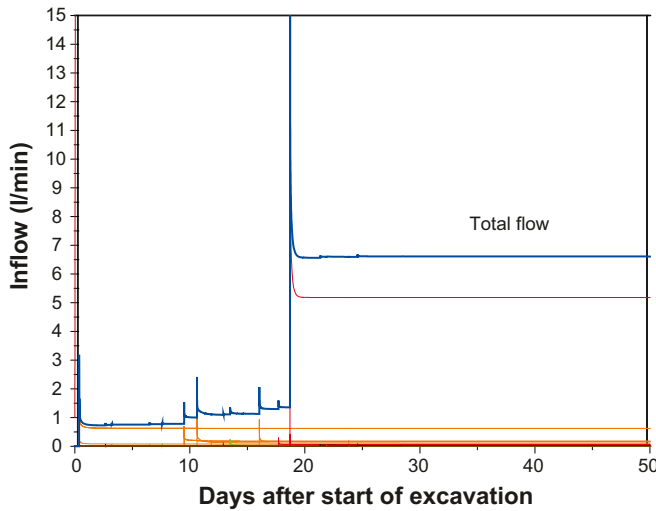
Figure 5-24. *Inflow to W01T23 during excavation can be compared with Figure 5-7.*

5.2.8 Effect of an adjacent open drift on excavation and emplacement

This section describes the models where W01T22 has been excavated and is open when W01T23 is excavated and W01T23 remains open while waste is emplaced in W01T22. Model runs have been performed using storage models A, C, D and E.

The motivation for the models are:

- The presence of an adjacent open drift during emplacement is likely to change the magnitude and rate of pressure change on closure.

- The closure of an adjacent drift may alter the inflow to an open drift.

Figure 5-25 shows the pressure recovery at feature intersections in W01T22 with W01T22 which can be compared with the pressure time histories shown in Figure 5-26 taken from equivalent single drift models. The rates of pressure increase and the levels at which pressure equilibrate are lower for most intersections. Figure 5-27 shows the inflows to W01T23 during emplacement in W01T22. Inflow increases by about 40% during emplacement in W01T22.

78
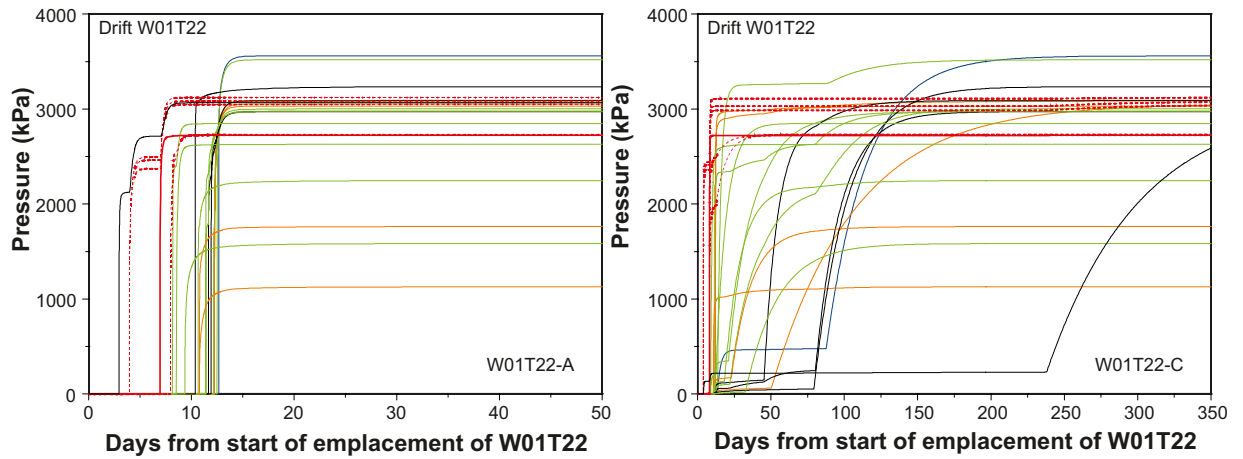
Figure 5-25. Pressure at feature intersections in W01T22 during emplacement with W01T23 open for storage models A and E.
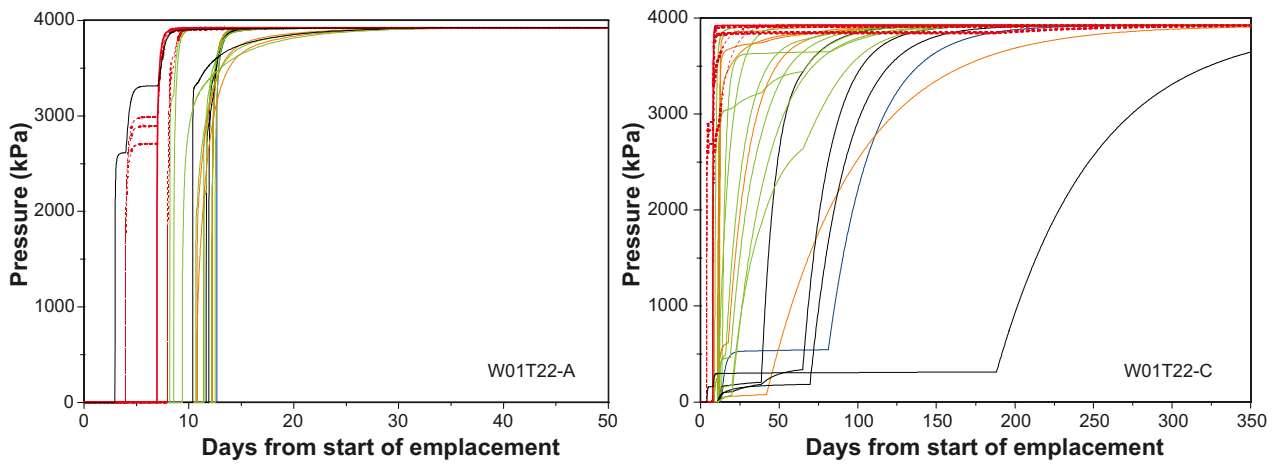
Figure 5-26. Pressure at feature intersections in W01T22 during emplacement for models without W01T23.
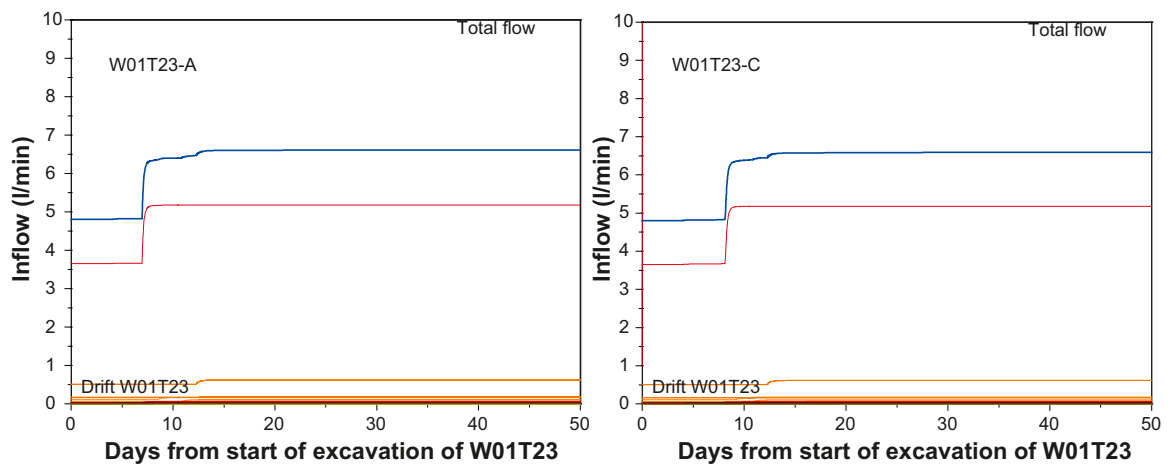
Figure 5-27. Inflow at feature intersections in W01T23 during emplacement in W01T22 with W01T23 open for storage models A and E.

6   Conclusions

6.1   Scope of the models

The transient and steady state flow models described in this report aim to provide input to the KBS-3H Process and Evolution reports. While they are quite detailed in their representation of the fractured rock and the excavation and emplacement sequence they are necessarily significant idealisations of the real system and do not include the following processes:

- Two phase flow within the Engineered Barrier System.
- Coupled mechanical processes associated with the swelling of the bentonite.
- Gas generation and migration due to corrosion of metal waste and packaging.

Geosphere model

The geosphere DFN model has been selected from a range of model variants developed within the study and includes relatively low transmissivity features however it is recognised that the real fracture system is likely to be more channelled. Data is however limited on the nature of the channelling expected at the site. In particular very small scale channelling (i.e. if flow is concentrated in metre-cm scale features) or flow concentrated in small fractures (< 10 m) might behave significantly differently from the models shown here.

Representation of drifts

Only very simple representations of the drifts have been used within the study and the emphasis has been on developing of understanding of the interaction between the geosphere and the drifts during the early evolution of the repository.

No account has been taken of the hydraulic action of the repository access tunnels and shafts. These will provide drainage features that will influence the hydraulic conditions around the deposition drifts.

The single drift models have not considered the action of nearby drifts and have assumed fixed head hydrostatic pressures on the boundaries of the model regions. In reality there will be some drawdown effect from the neighbouring drifts and other features, such that inflow and pressure gradients will be reduced. The two-drift models show quite large drawdowns due to the presence of an open adjacent drift.

6.2   Model results

The models appear to be satisfactorily simulating the changes in flow and pressure around drifts during excavation and emplacement.

Inflows reach steady state levels quickly after the end of excavation. Lower transmissivity fractures are likely to be of lower diffusivity resulting in longer transients, while pressure changes within the matrix are likely to be very slow indeed. However, given that the bulk of the inflow will be associated with more permeable fractures the models suggest that inflow will stabilise within 20 days of the end of excavation. Inflows will, however, be influenced by excavation activities in neighbouring drifts.

The dominant factor in pressure recovery in the super-container sections is the length of time required to fill up the gap volume prior to the start of pressure recovery. Once the gap volume is

filled transients associated with pressure recovery in the more transmissive parts of the fracture system are relatively swift and controlled by the accessible pore volume and storage associated with the drift elements. In matrix sections or sections containing very low transmissivity fractures (i.e. those sections not modelled within the DFN models) responses will be very slow.

Pressure responses are heterogeneous with the majority of super-containers not intersecting transmissive fractures. Within these sections no significant pressure rise is predicted within the first years as any water inflow is taken up by the bentonite.

Rate of pressure rise

The rate of pressure rise (pressure derivative in kPa/hr) is largely controlled by the geosphere inflow and the assumptions concerning the storage term associated with the super-containers and distance blocks. In models where no storage is associated with the drift sections, pressure rises very quickly with derivatives of greater than 1 MPa/hr. In the models containing greater storage either due to trapped air (model D) or the use of a larger storage term (model E) then the highest gradients are only associated with high transmissivity features located in blank or seal sections. Typically pressures rise faster around the distance blocks as these have been associated with smaller storage terms within models D and E. The effect of the storage term for a drift section intersecting a 0.1 l/min feature (transmissivity 2.65×10^{-9} m^2/s) is clearly seen in Figure 6-1 (see Chapter 4) where for storage term (CT value) greater than 8×10^{-8} m^3/Pa the pressure derivative is below 100 kPa/hr.

The most significant elements in the storage term are likely to be the uptake of water into the bentonite and the presence of any trapped air in the gap volume. It may be useful to model the uptake of water into the bentonite to determine an appropriate water loss term that could be used within any future models.
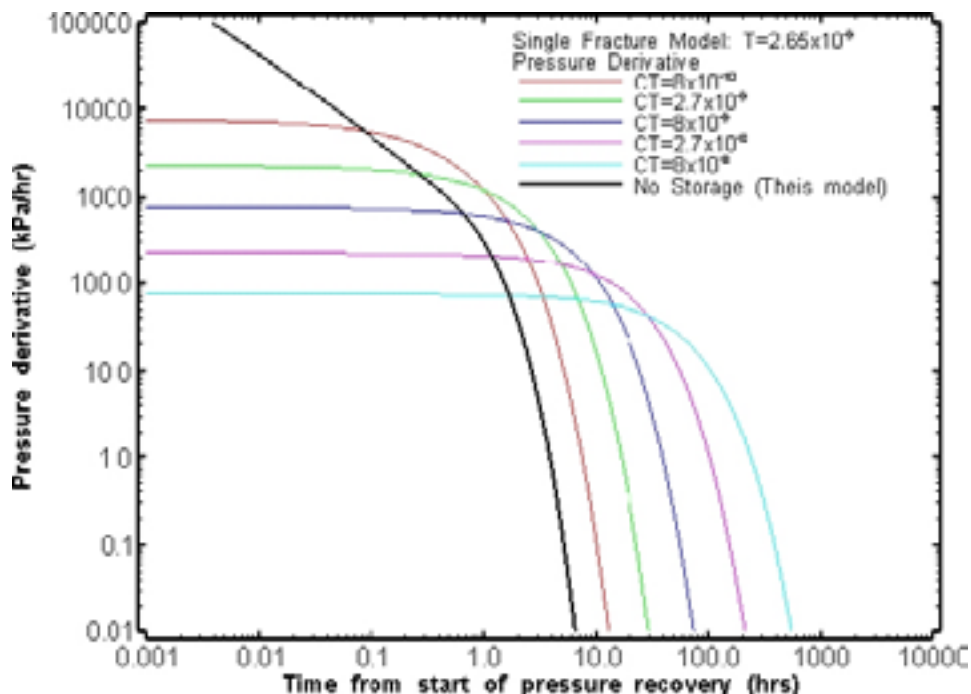
Figure 6-1. *Pressure derivative (increase rate kPa/hr) for fracture T = 2.65×10⁻⁹ m²/s (0.1 l/min) and varying storage term (CT in m³/Pa) from nSights models.*

82

Time to fill gap volume

The models suggest that some of the super-container gap volumes will be filled within 10–20 days after the start of emplacement. The controlling factor is the transmissivity of any features intersecting the super-container section. Sections where the transmissivity of any features is below 10^{-10} m^2/s will take ~200 days or more. In matrix sections considerably longer time will be needed.

Differential pressure between super container sections

The models indicate that pressure recovery will be heterogeneous with only a fraction of the super containers becoming pressurised during the first year of operation. Significant differential forces will develop across the distance blocks separating a pressurised super container section where the bentonite is likely to have swollen from the adjacent potentially dry super container section. This is illustrated in Figure 6-2 where un-pressurised sections of drift are interspersed between the pressurised sections.

Influence of excavation of adjacent drifts

The models suggest that pressure disturbances due to the excavation of adjacent drifts maybe large (~2 MPa) and fast (depending on the storage). Typically the most transmissive features react most quickly, but drawdowns are seen in almost all intervals intersected by transmissive features.

Recommendations

The pressure behaviour during emplacement within the models is controlled largely by storage term associated with the drift elements. It may be useful to revisit the coupled models of buffer saturation /Börgesson et al. 2005/ to determine whether reliable estimates of the water uptake by the bentonite and better understanding of inflow and pressure during saturation can be taken from the modelling or other related work.
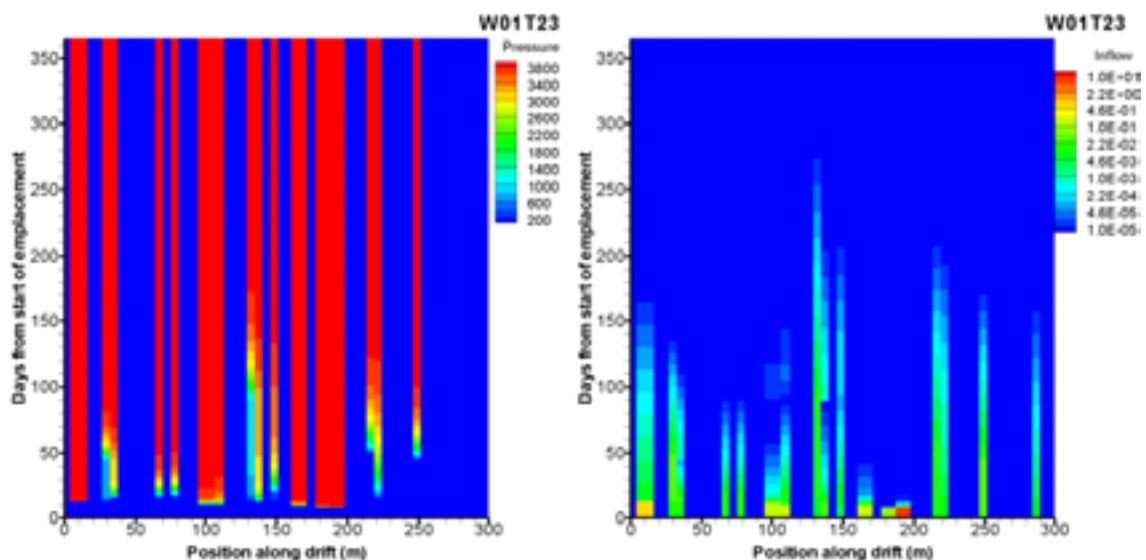
Figure 6-2. *Pressure and inflow as a function of time and position along drift for W01T023 for storage model E.*

6.3 Conclusions

Within the DFN modelling study the following tasks have been accomplished:

1) Construction of a set of DFN model variants of the fault and fracture system in the repository consistent with hydraulic data from the site.

2) Calculation of geometric properties of fracture intersections with the repository deposition drifts for four model variants, and multiple realisations (50–100).

3) Calculation of effective hydraulic properties at different scales (100 m and 250 m cubes) for model variants.

4) Development of a model of the hydraulic response of an isolated single fracture to excavation and drift closure (including effects of grouting and "storage term").

5) Development of transient flow models of single and dual drift systems and their response to excavation and drift closure.

6) Estimation of fluxes and transport parameters of the flow field around a single drift after saturation of the EBS.

Although these tasks were performed within the context of the Process and Evolution Reports, they may have wider application within the KBS-3H project as a whole, and more generally for understanding of the hydrogeological conditions at the Olkiluoto site. In order to meet the needs of the project teams, the work was performed between September 2005 and April 2006 and it was necessary to build the models on the basis of existing data and interpretations. It is expected that representations of the geosphere and of the performance of the Engineered Barrier System will continue to be developed during the remainder of the KBS-3H project. During the DFN study the detailed design of the disposal system was evolving and it is likely that parameters used within the models (e.g. compartment plug dimensions) may change in the future.

DFN models of the fault and fracture system in the repository volume

The DFN models presented here have been developed to provide estimates of the likely inflows to repository tunnels using the currently available data and interpretations. They have been calibrated to the average frequency and transmissivity measured in boreholes within the repository volume. They provide a baseline interpretation of the fault and fracture system, which can be developed as new information is acquired from the site. In addition, they can be tested against other types of existing data.

Repository layout

The geometric simulations indicate a consistent layout across all the geosphere model variants and realisations. Typically each 300 m drift is divided into 2 compartments by a single seal. Each drift on average contains 23 super-containers with 3–4 blank sections. Total average inflows to the compartments (prior to grouting) within a drift are about 1.5 l/min. Inflows to a single compartment are below 1.0 l/min. These inflow values are consistent between the geometric simulations and the single and dual drift transient flow models.

The cumulative distribution of total inflow to a single drift (as estimated by the method described in Chapter 3) for 100 realisations of the extended reference case is shown in Figure 6-3. Approximately 18% of drifts exceed the suggested 30 l/min limit without grouting. If grouting can be successfully performed (reduction to $10^{-8}\,\mathrm{m^2/s}$) the maximum inflow in all realisations is reduced to about 15 l/min with less than 1% of drifts exceeding 10 l/min. These values vary only slightly between the different model variants (the highest percentage of drifts exceeding 30 l/min inflow is 23% in the channelled model variant). It should be remembered that the inflow estimate is likely to be conservative for the reasons listed in the discussion on inflow estimation in Section 3.2.
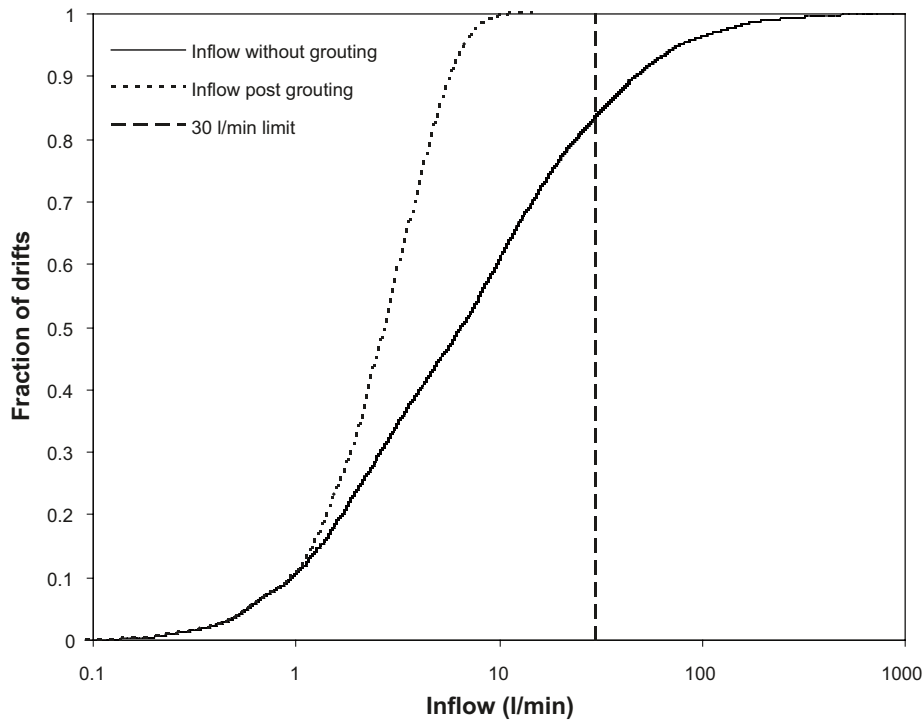
Figure 6-3. *Cumulative drift inflow distribution for 100 realisations of Extended Reference Case model variant with transmissivity cut-off at 10^{-11} m²/s.*

High drift inflows relate to intersections with individual high transmissivity WCFs or LFZs and as long as these features can be successfully sealed by grouting or by the installation of compartment plugs, the inflows to compartments themselves are typically very low.

Response to excavation and closure

The models suggest that pressure transients associated with the excavation of a single drift will be relatively short-lived (~30 days) in the permeable parts of the fracture system. The pressure transients in the matrix and very low transmissivity fractures ($< 10^{-10}$ m²/s) will last much longer. Inflow is expected to reduce and stabilise to a lower rate soon after excavation. Transients in inflow to a particular drift will be caused by the excavation and closure of adjacent drifts and other tunnels, although the dual drift flow model indicates that the variation in inflow due to operations in adjacent drifts will be of limited magnitude.

The single fracture model and transient drift-scale flow models demonstrate the importance of the "storage" associated with the EBS in controlling the rate of pressure recovery on closure and the potential for developing conditions where piping may occur. High rates of pressure derivative (over 1 MPa/hr) are possible if the storage is small. The models also show that pressure recovery is likely to be highly heterogeneous and dominated by the time taken to fill the void volumes around the super-containers. In very low permeability drift intervals no pressure rise is expected for a significant period (decades or longer).

The models also show that changes in inflow during emplacement of the super-containers and distance blocks are likely to be of limited magnitude.

Input to the Process and Evolution Reports

The DFN study has provided the following inputs to the Process and Evolution reports:

- Models of the fault and fracture system.

- Database and summary statistics for the likely distribution of inflows to deposition drifts.

- A single fracture model illustrating the likely geosphere pressure and flow in a single super-container or distance block section during excavation and emplacement.

- Transient models of excavation and emplacement illustrating the possible evolution of pressure and flow in the geosphere during the early evolution of the disposal system.

- Database of sample post-saturation fluxes and transport properties for flow around deposition drifts.

6.4   Open questions and uncertainties

Geosphere

The models have shown that there is relatively little variation in the expected inflows between the different model variants considered. The choice of model variants, however, has concentrated on the interpretation of the transmissivity and frequency of the water conducting features (WCFs) in the background rock. The following features of the fault and fracture system could have a significant impact on the prediction of likely inflows and pressure responses to excavation and drift closure:

- Clustering of WCFs and Local Fracture Zones (LFZs), creating zones of more intense fracturing and large un-fractured regions.

- Depth trends in the fracture system such that the properties derived by averaging over the 300–750 m depth horizon are not representative of 400 m depth (e.g. a significant drop in fracture density below 500 m).

- Different interpretations of LFZ orientation and distributions (currently assumed to mimic the orientation distribution derived from outcrop maps).

- Very small scale channelling at sub-metre scales. The channel variant includes transmissivity variation across WCFs at 1/10 the size of the WCF i.e. from 1 to 50 m. Given that most intersections are with the largest structures, there is little difference between the intersection statistics of a 100 mm diameter borehole and a 1.85 m tunnel. If channels occur at small scales e.g. cm or dm, however, then intersection statistics for tunnels might be significantly different than for boreholes.

- Flow concentrated in small fractures. The models have only considered fractures > 10 m in length as contributing to significant flow.

- Any bias in the measurement of transmissivity during flow logging.

- Action of near tunnel-wall processes in changing inflows (e.g. ventilation, EDZ, two-phase flow).

Engineered Barrier System

The major uncertainty here relates to the appropriate representation of the "storage" associated with super-containers and distance blocks. In this context storage is a "lumped term" incorporating multiple effects (e.g. inflow into the compacted bentonite; compressibility of gel/water mix in the gap volume, effect of trapped air and compressibility of the rock and compacted bentonite), which will change with time as the bentonite swells and homogenises. Our interest is in the early time, however, when inflows may cause the pressure to rise rapidly and piping is possible.

6.5   Recommendations

Geosphere

Work on the interpretation and modelling of the LFZs may be useful in improving the understanding of their extent orientation and hydraulic properties. Within the models presented here, it has been assumed that they follow the same structural trends as individual fractures and that they are uniformly distributed within the repository volume.

In addition, it may be useful to improve understanding about the clustering/larger scale organisation of the fracture system in the repository volume. The models presented here suggest that either:

- The fault and fracture system is more highly clustered than the models.

- The borehole intervals include highly fractured intervals related to unidentified structures (see comments about. KR03 and KR08).

Engineered Barrier System

More sophisticated models of the EBS geosphere interaction during saturation could be implemented within the DFN models. Input for these models could come from existing coupled hydromechanical models (e.g. those discussed in /Börgesson et al. 2005/) or from analysis of the current laboratory testing programme (again see Börgesson et al. op cit). One option would be to explicitly account for the uptake of water by the bentonite within the storage term.

It may also be useful to consider the influence of nearby drifts, access tunnels etcon flow into the deposition drifts, within the current models. The presence of additional open voids is expected to reduce the pressure magnitude, pressure gradient and inflows to any single drift. The models presented here have only considered a relatively small number of realisations and scenarios.

7   References

Ahokas H, Hellä P, Ahokas T, Hansen J, Koskinen K, Lehtinen A, Koskinen L, Löfman J, Meszàros F, Partamies S, Pitkänen P, Sievänen U, Marcos N, Snellman M, Vieno T, 2006. Control of Water Inflow and Use of Cement in ONKALO after Penetration of Fracture Zone R19. Working Report 2006-45. Posiva Oy, Olkiluoto.

Autio J, 2006. KBS-3H Design Description 2005. Working Report 2006-xx. Posiva Oy, Olkiluoto, (in preparation).

Black J H, Kipp K L Jr, 1977. Observation well response time and its effect on aquifer test results. Journal of Hydrology, Vol. 34, pp. 297–306.

Börgesson L, Sandén T, Fälth B, Åkesson M, Lindgren E, 2005. Studies of buffers behaviour in KBS-3H concept. Work during 2002–2004. SKB R-05-50, Svensk Kärnbränslehantering AB.

Dershowitz W S, 1984. Rick Joint Systems. MIT PhD Thesis MIT, Cambridge, MA.

Dershowitz W, Eiben T, Follin S, Andersson A, 1999. SKB R-99-43, Svensk Kärnbränslehantering AB.

Doe T, Geier J, 1990. Interpretation of fracture system geometry using well test data. Stripa Project Technical Report TR 91-03, Svensk Kärnbränslehantering AB.

Domenico P A, Schwartz F, 1997. Physical and Chemical Hydrogeology (2nd ed). John Wiley and Son.

Hellä P, Ahokas H, Palmén J, Tammisto E, 2006. Analysis of geohydrological data for assessment of the alternative repository layout KBS-3H. Working Report 2005-16. Posiva Oy, Olkiluoto.

Holton D, Milický M, 1997. Simulating the LPT2 and Tunnel Drawdown Experiment at Äspö using a Coupled Continuum-Fracture Network Approach. SKB ICR 97-05, Svensk Kärnbränslehantering AB.

Holton D, Hartley L, Hautojärvi A, Marschall P, Selroos J-O, 2003. iCONNECT Club: integrated CONtinuum and NEtwork approach to groundwater flow and Contaminant Transport. Materials Research Society Symposium Proceedings Volume 807, Scientific Basis for Nuclear Waste Management XXVII.

Hämäläinen H, 1997a. Measurements of hydraulic conductivity at Olkiluoto in Eurajoki, borehole OL-KR1. Working Report 97-03. Posiva Oy, Helsinki. 476 p. (Vol. 1 and 2) (in Finnish).

Hämäläinen H, 1997b. Measurements of hydraulic conductivity at Olkiluoto in Eurajoki, borehole OL-KR2. Working Report 97-21. Posiva Oy, Helsinki. 820 p. (Vol. 1 and 2) (in Finnish).

Hämäläinen H, 1997c. Measurements of hydraulic conductivity at Olkiluoto in Eurajoki, borehole OL-KR4. Working Report 97-45. Posiva Oy, Helsinki. 1079 p. (Vol. 1, 2 and 3) (in Finnish).

Hämäläinen H, 1997d. Measurements of hydraulic conductivity at Olkiluoto in Eurajoki, borehole OL-KR8. Working Report 97-46. Posiva Oy, Helsinki. 333 p (in Finnish).

Hämäläinen H, 1997e. Measurements of hydraulic conductivity at Olkiluoto in Eurajoki, borehole OL-KR10. Working Report 97-47. Posiva Oy, Helsinki. 243 p (in Finnish).

Hämäläinen H, 2003a. Complementary hydraulic conductivity measurements at Eurajoki, Olkiluoto, borehole OL-KR1. Working Report 2003-27. Posiva Oy, Olkiluoto. (Vol. 1 and 2) (in Finnish with an English abstract).

Hämäläinen H, 2003b. Complementary hydraulic conductivity measurements at Eurajoki, Olkiluoto, borehole OL-KR7. Working Report 2003-47. Posiva Oy, Olkiluoto. (Vol. 1 and 2) (in Finnish with an English abstract).

Hämäläinen H, 2003c. Complementary hydraulic conductivity measurements at Eurajoki, Olkiluoto, borehole OL-KR10. Working Report 2003-54. Posiva Oy, Olkiluoto. (Vol. 1 and 2) (in Finnish with an English abstract).

Hämäläinen H, 2004a. Complementary hydraulic conductivity measurements at Eurajoki, Olkiluoto, borehole OL-KR12. Working Report 2004-14. Posiva Oy, Olkiluoto. (Vol. 1 and 2) (in Finnish with an English abstract).

Hämäläinen H, 2004b. Hydraulic conductivity measurements with HTU at Eurajoki Olkiluoto, borehole OL-KR13. Working Report 2004-40. Posiva Oy, Olkiluoto. (Vol. 1 and 2).

Hämäläinen H, 2005. Hydraulic conductivity measurements with HTU at Eurajoki Olkiluoto, borehole OL-KR14. Working Report 2004-42. Posiva Oy, Olkiluoto. (Vol. 1 and 2).

Hämäläinen H, 2006a. Hydraulic conductivity measurements with HTU at Eurajoki Olkiluoto, borehole OL-KR2. Working Report 2006-10. Posiva Oy, Olkiluoto. (Vol. 1 and 2).

Hämäläinen H, 2006b. Hydraulic conductivity measurements with HTU at Eurajoki Olkiluoto, borehole OL-KR4. Working Report 2006-24. Posiva Oy, Olkiluoto. (Vol. 1 and 2).

Johansson E, Äikäs K, Autio J, Hagros A, Malmlund H, Rautakorpi J, Sievänen U, Wanne T, Anttila P, Raiko H, 2002. Preliminary KBS-3H layout adaptation for the Olkiluoto site – Analysis of rock factors affecting the orientation of a KBS-3H deposition hole. Working Report 2002-57. Posiva Oy, Olkiluoto.

Johnson L, Marschall P, Wersin P, Gribi P, 2005. HMCBG processes related to the steel components in the KBS-3H disposal concept. Working Report 2005-09. Posiva Oy, Olkiluoto.

LaPointe P, Hermanson J, 2002. Estimation of rock movements due to future earthquakes at four Finnish candidate repository sites. POSIVA 2002-02. Posiva Oy, Helsinki. 89 p. ISBN 951-652-109-6.

Posiva, 2005. Olkiluoto Site Description 2004. POSIVA 2005-03. Posiva Oy, Olkiluoto.

Poteri A, 2001. Estimation of the orientation distributions for fractures at Hästholmen, Kivetty, Olkiluoto and Romuvaara. Working Report 2001-10. Posiva Oy, Helsinki. 14 p.

Roberts R M, Beauheim R L , Avis J D, 2002. (Quantifying Parameter Uncertainty in Well Test Analysis, In Proceedings of International Groundwater Symposium, pg 238–239, Lawrence Berkeley National Laboratory, Berkeley, CA, March 25-28, 2002).

Serco Assurance, 2002. www.connectflow.com.

Thorsager P, Lindgren E, 2004. KBS-3H Summary report of work done during Basic Design. SKB R-04-42, Svensk Kärnbränslehantering AB.

Vaittinen T, Ahokas H, Heikkinen E, Hellä P, Nummela J, Saksa P, Tammisto E, Paulamäki S, Paananen M, Front K, Kärki A, 2003. Bedrock model of the Olkiluoto site, version 2003/1. Working Report 2003-43. Posiva Oy, Olkiluoto. 266 p.

Vieno T, Lehikoinen J, Löfman J, Nordman H, Mészáros F, 2003. Assessment of Disturbances Caused by Construction and Operation of ONKALO. POSIVA 2003-06. Posiva Oy, Olkiluoto.

Statistical summaries from geometric simulations

Table A-1. Summary of selected drift measures for the different model variants.

Property	Number of compartments					Number of seals					Number of super-containers				
Name	RC	RE-10	RE-11	LT	Chan	RC	RE-10	RE-11	LT	Chan	RC	RE-10	RE-11	LT	Chan
Arithmetic mean	2.2	2.1	8,5	2.0	2.3	1.5	1.3	1.3	1.2	1.6	22.5	23.1	23.1	22.4	22.7
Median	2.0	2.0	2.0	2.0	2.0	1.0	1.0	1.0	1.0	1.0	23.0	23.0	23.0	23.0	23.0
Standard Dev	1.0	1.0	1.0	0.9	1.0	1.1	1.1	1.1	1.0	1.1	2.4	2.4	2.4	2.5	2.5
Minimum	1	1	1	1	1	0	0	0	0	0	0	9	9	0	0
1% percentile	1	1	1	1	1	0	0	0	0	0	15	17	17	15	15
5% percentile	1	1	1	1	1	0	0	0	0	0	18	19	19	18	18
25% percentile	1	1	1	1	2	1	0	0	0	1	21	22	22	21	21
50% percentile	2	2	2	2	2	1	1	1	1	1	23	23	23	23	23
75% percentile	3	3	3	3	3	2	2	2	2	2	24	25	25	24	24
95% percentile	4	4	4	4	4	3	3	3	3	4	26	26	26	26	26
99% percentile	5	5	5	5	5	4	4	4	4	5	27	27	27	27	27
Maximum	7	7	7	7	7	6	6	6	6	8	27	27	27	27	27

Table A-2. Summary of selected compartment measures for the different model variants.

Property	Number of super-containers					Length of compartment					Inflow (l/min)				
Name	RC	RE-10	RE-11	LT	Chan	RC	RE-10	RE-11	LT	Chan	RC	RE-10	RE-11	LT	Chan
Arithmetic m an	10.1	10.9	10.9	11.0	9.8	128.3	137.0	137.0	142.0	123.4	0.7	0.7	0.7	0.9	0.6
Median	8.0	9.0	9.0	9.0	8.0	103.4	110.9	110.9	122.7	99.8	0.5	0.5	0.5	0.7	0.4
Standard Dev	7.5	8.1	8.1	7.8	7.4	89.4	94.4	94.4	93.4	86.4	0.7	0.7	0.7	0.8	0.7
Minimum	0	0	0	0	0	16	16	16	16	16	0.0	0.0	0.0	0.0	0.0
1% percentile	0	0	0	0	0	17	17	17	17	17	0.0	0.0	0.0	0.0	0.0
5% percentile	1	1	1	1	1	22	22	22	23	22	0.0	0.0	0.0	0.0	0.0
25% percentile	4	4	4	4	4	52	55	55	60	51	0.1	0.2	0.2	0.2	0.1
50% percentile	8	9	9	9	8	103	111	111	123	100	0.5	0.5	0.5	0.7	0.4
75% percentile	15	17	17	17	15	192	213	213	216	179	1.0	1.1	1.1	1.3	0.9
95% percentile	25	26	26	25	25	300	300	300	300	300	2.1	2.2	2.2	2.5	2.0
99% percentile	26	27	27	26	26	300	300	300	300	300	3.1	3.0	3.1	3.5	2.9
Maximum	27	27	27	27	27	300	300	300	300	300	6.0	5.3	5.4	7.4	5.4

Table A-3. Summary of selected seal measures for the different model variants.

Property	Seal zone length					Inflow (l/min)					Inflow post grouting (l/min)				
Name	RC	RE-10	RE-11	LT	Chan	RC	RE-10	RE-11	LT	Chan	RC	RE-10	RE-11	LT	Chan
Arithmetic mean	8.4	8.3	8.3	8.6	8.5	13.1	14.3	14.3	18.0	22.6	1.2	1.2	1.2	1.3	1.2
Median	4.8	4.8	4.8	5.0	4.9	3.7	4.0	4.0	3.9	4.7	0.8	0.8	0.8	0.8	0.8
Standard Dev	8.6	8.6	8.6	9.0	8.8	46.3	40.0	39.7	68.2	181.7	0.8	0.8	0.8	0.9	0.8
Minimum	1	1	1	1	1	1	1	1	1	1	0.8	0.8	0.8	0.8	0.8
1% percentile	2	2	2	2	2	1	1	1	1	1	0.8	0.8	0.8	0.8	0.8
5% percentile	2	2	2	2	2	1	1	1	1	1	0.8	0.8	0.8	0.8	0.8
25% percentile	3	3	3	3	3	2	2	2	2	2	0.8	0.8	0.8	0.8	0.8
50% percentile	5	5	5	5	5	4	4	4	4	5	0.8	0.8	0.8	0.8	0.8
75% percentile	11	11	11	11	11	10	11	11	13	14	1.5	1.5	1.5	1.5	1.5
95% percentile	25	25	26	25	25	49	56	56	69	77	3.0	2.9	2.9	3.1	2.9
99% percentile	41	39	39	42	41	142	165	165	221	257	4.4	4.2	4.2	4.5	4.3
Maximum	103	124	124	195	103	1,784	1,010	1,010	3,080	13,850	9.8	10.1	10.1	11.1	9.1

Table A-4. Summary of selected WCF measures for the different model variants.

Property	Log_{10} Transmissivity					Inflow (l/min)					Trace Length (m)				
Name	RC	RE-10	RE-11	LT	Chan	RC	RE-10	RE-11	LT	Chan	RC	RE-10	RE-11	LT	Chan
Arithmetic mean	−8.4	−9.1	−10.0	−8.4	−8.6	1.9	0.8	0.3	2.0	3.2	8.8	8.8	8.8	8.9	8.2
Median	−8.4	−9.3	−10.3	−8.4	−8.7	0.1	0.0	0.0	0.2	0.1	7.2	7.2	7.2	7.2	7.0
Standard Dev	0.9	0.9	0.9	1.0	1.0	17.8	7.7	3.8	19.2	91.1	8.1	7.3	7.1	9.1	7.6
Minimum	−11.8	−11.1	−11.0	−13.0	−11.6	0.00	0.00	0.00	0.00	0.00	0.0	0.0	0.0	0.0	0.0
1% percentile	−10.3	−10.0	−11.0	−11.1	−10.0	0.00	0.00	0.00	0.00	0.00	0.9	0.9	0.8	0.9	0.5
5% percentile	−9.8	−10.0	−11.0	−10.2	−9.8	0.01	0.00	0.00	0.00	0.01	2.6	2.6	2.7	2.6	1.8
25% percentile	−9.0	−9.7	−10.7	−9.0	−9.3	0.04	0.01	0.00	0.04	0.02	6.3	6.3	6.3	6.3	6.0
50% percentile	−8.4	−9.3	−10.3	−8.4	−8.7	0.14	0.02	0.00	0.16	0.07	7.2	7.2	7.2	7.2	7.0
75% percentile	−7.8	−8.6	−9.6	−7.9	−8.0	0.59	0.09	0.01	0.52	0.42	9.1	9.1	9.2	9.2	8.8
95% percentile	−6.8	−7.3	−8.0	−6.9	−6.8	5.7	2.0	0.4	5.0	6.3	18.7	18.6	18.5	18.7	17.0
99% percentile	−6.1	−6.4	−6.9	−6.1	−6.0	31.2	13.6	5.3	33.2	41.2	40.1	36.3	36.3	38.2	37.4
Maximum	−4.4	−4.8	−5.0	−4.4	−3.4	1,648	647	371	1,458	13,850	524.0	227.4	238.5	503.4	243.6

Model variants: RC: Reference Case; RE-10: Reference Extended cutoff at T 10^{-10} m²/s; RE-11: Reference Extended cutoff at T 10^{-11} m²/s; LT: LT Correlation variant; Chan: Channel variant (cutoff at T 10^{-10} m²).

Steady state flow models

Amongst the outputs requested by the project team were travel paths, transport parameters and flow rates around the drifts after stabilisation. It is assumed that the system has recovered from the hydraulic disturbances from excavation and emplacement to close to hydrostatic pressure. No account has been taken of any pressure disturbance caused by gas generation from the waste and packaging.

B.1   Particle tracking models

Demonstration particle tracking calculations were requested for a small number of drifts. The models used the four drifts considered within Chapter 5. The geosphere representation used was that for the Extended Reference Case with a transmissivity cut-off of 10^{-11} m^2/s. The lower transmissivity fractures were included so that more super-container sections were intersected by model features (only about 40% of super-containers intersect fractures with transmissivity $>10^{-10}$ m^2/s).

The transport aperture b (m) was assumed to be a function of the feature transmissivity T (m^2/s) such that $b = \dfrac{T^{0.5}}{2}$ (see /Holton et al. 2003/ and /Dershowitz et al. 1999/). Alternative transport aperture models are available in CONNECTFLOW but this simple model was used for the demonstration calculations. Note that the models did not consider small-scale heterogeneity within flowing features as there was only very limited information available on channel properties for the repository volume at the time of the study. A unit vertical pressure gradient of 0.01 m/m (see Appendix F) has been applied to the outer model boundaries. The gradient results in an overall downward flow.

Particles were started at the intersection of fracture sub-planes with the 1-D super-container drift elements. The particle starting points were distributed across each drift element randomly weighted by the outflow from that node. The particles were then tracked within the detailed pressure field from the steady state solution (using the CONNECTFLOW "Exact Particle Tracking" option). Particle tracking requires a more highly refined pressure solution than was needed for the transient flow solutions, with higher mesh refinement on each sub-plane and along each intersection. Even with this higher refinement about 3% of particles were lost to local "sinks" on fracture planes. In some cases, local sinks affected a large percentage of particles (maximum 21%) from a single super-container.

1,000 particles were tracked from each 1-D element representing a super-container that inter-sected a feature. In all 65 out of a total of 84 super-containers in the four drifts were considered (about 10% of the super-container sections intersect features if modelled as volumes but do not intersect the 1-D elements). The advective travel time (years) and F quotient (years/m) were calculated for each particle. Figure B-1 shows sample particle tracks (100 from each super-container drift element) for W01T01. Where transmissive features exist close to the drift particles are typically diverted into them (see for example path along edge of steep vertical feature in the centre of the model).
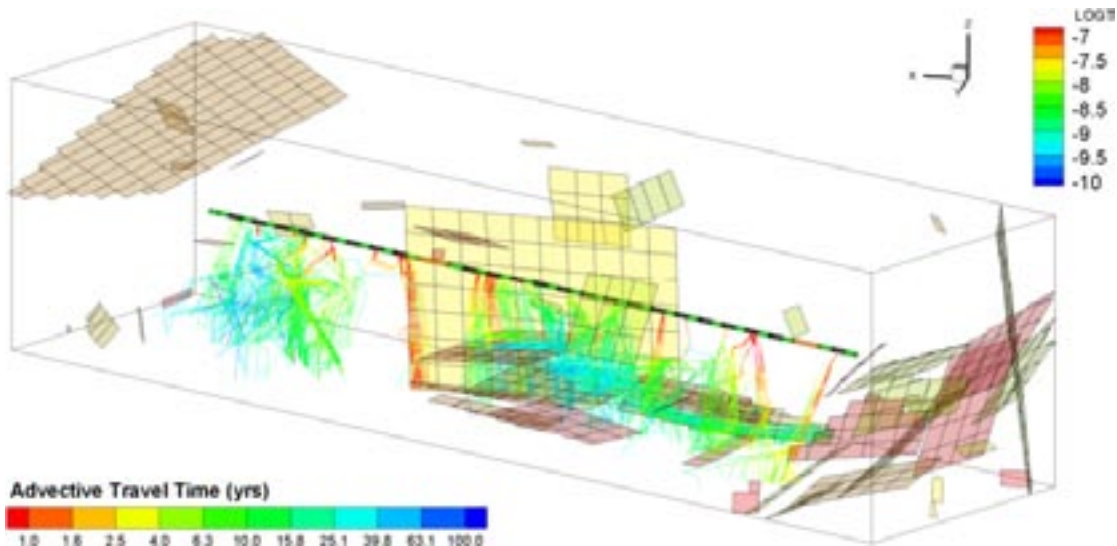
Figure B-1. *Particle tracks from super-container drift elements for W01T01. Tracks coloured by travel time. Features coloured by log transmissivity, only features with transmissivity greater than 10^{-8} m²/s are shown.*

Histograms of advective travel time and $\log_{10}$ F quotient for each super-container intersected by a feature in the four drifts are shown in Figures B-2 and B-3. A statistical summary of travel time to the model boundaries (50 m), mean advective velocity (over path) and F quotient are given in Table B-2 at the end of this appendix.

B.2   Flow calculations

In addition to the particle tracking outputs, the flow past a super-container is also of interest for the evaluation of long-term safety. Within this study two approaches to estimating the flow have been used:

- Geometric approach using the results of the geometric simulations described in Chapter 3.

- Detailed flow modelling for a small number of drifts.

B.2.1   Geometric estimates of flow past a super-container

The geometric estimates are based on the trace-map analyses described in Chapter 3. Two methods of estimating the flow past a super-container tunnel-section were used:

$$\text{Method1}: Q = \sum_{\text{int} er \sec tions} \frac{TLfi}{2} \qquad \text{Method2}: Q = \sum_{\text{int} ersctions} \frac{TLi}{2}$$

$$\text{for super - containers not intersceted by a WCF}: Q = KDli$$

where T is transmissivity of WCF (m²/s) intersecting the tunnel section occupied by the super-container; L is the trace-length (m) of the intersection with the tunnel; f is the fraction of the WCF trace within the super-container tunnel section (0-1); i is the regional gradient taken as 0.01 m/m (Appendix F). The summation is made over all fractures intersecting the super-container section.

The difference between the two methods is that in method 2 all the trace-length of any feature intersecting the super-container section is assumed to contribute to flow past the super-container section, while in method 1 only the fraction of the trace within the 5.56 m length of the super-container is used.

96
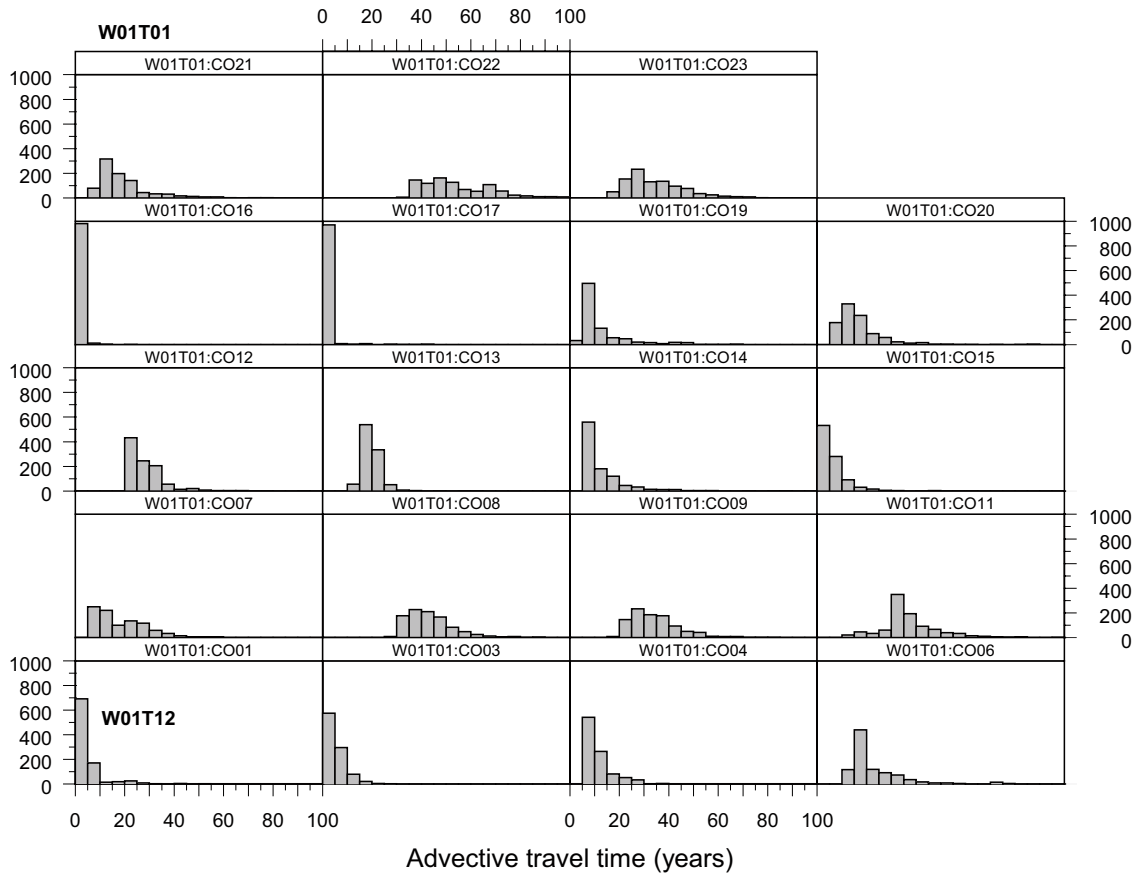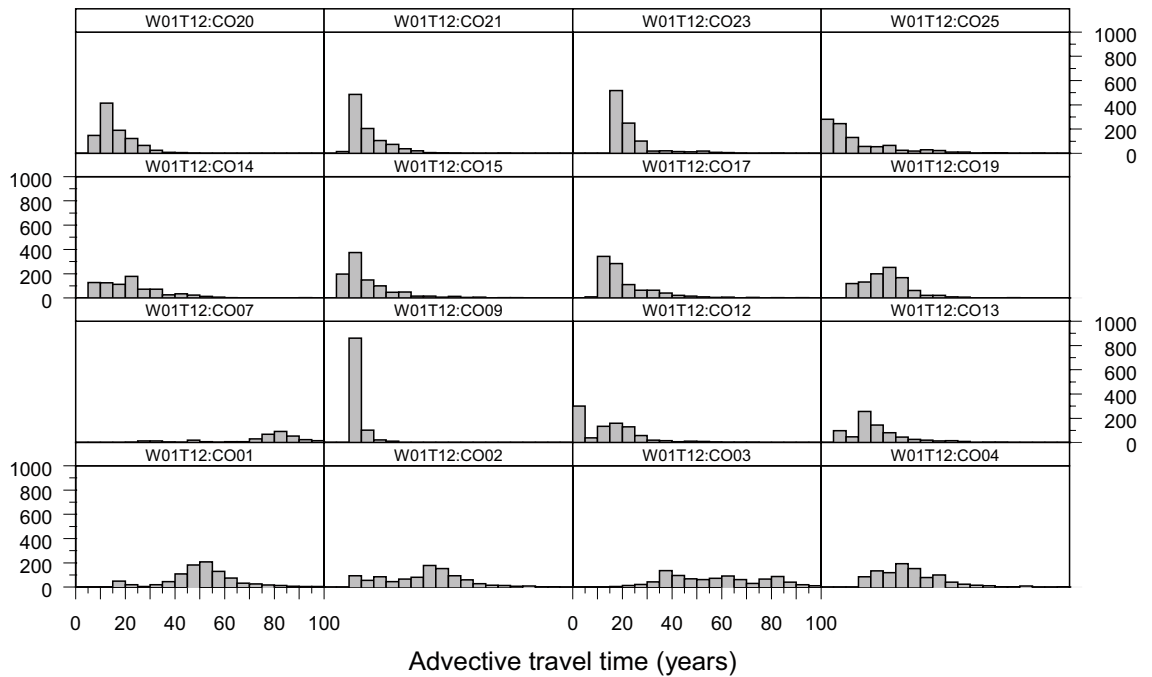
Figure B-2. *Histograms of advective travel time from particles released at the different super-container elements for W01T01, W01T12, W01T22 and W01T23.*

W01T22

W01T23

c)

Advective travel time (years)
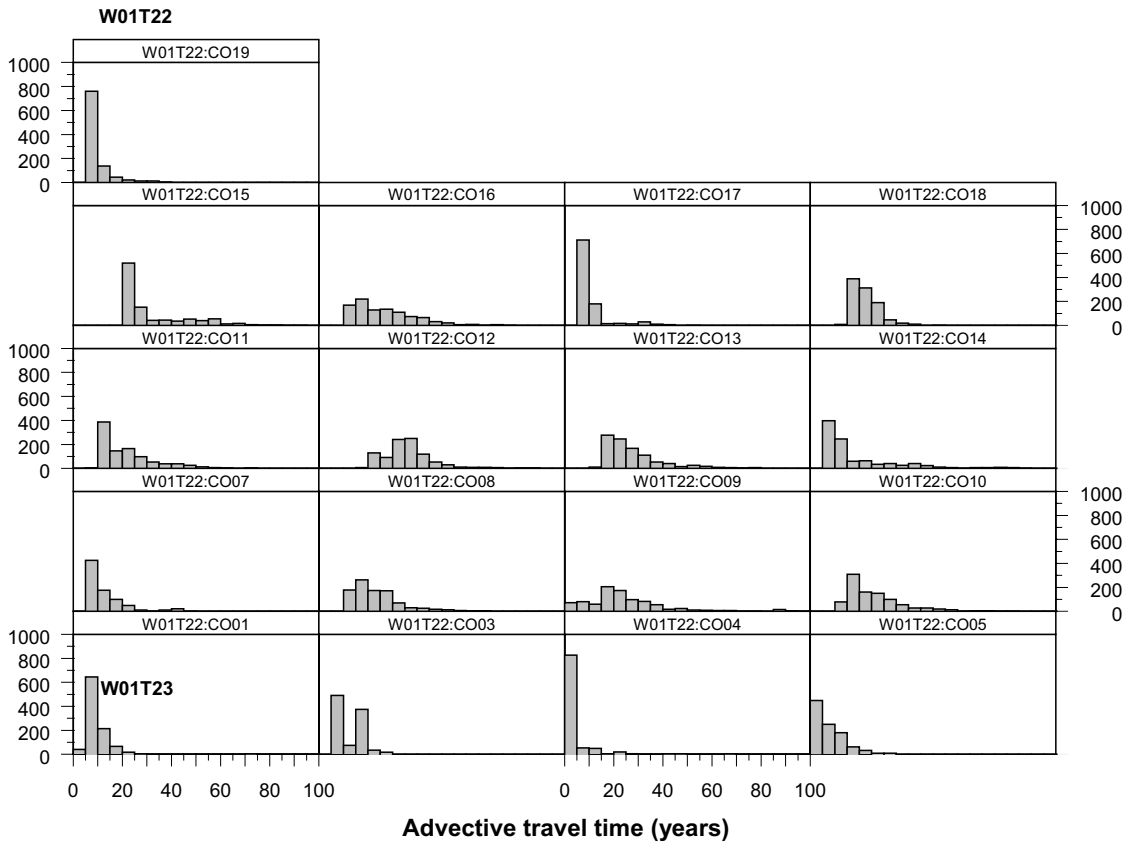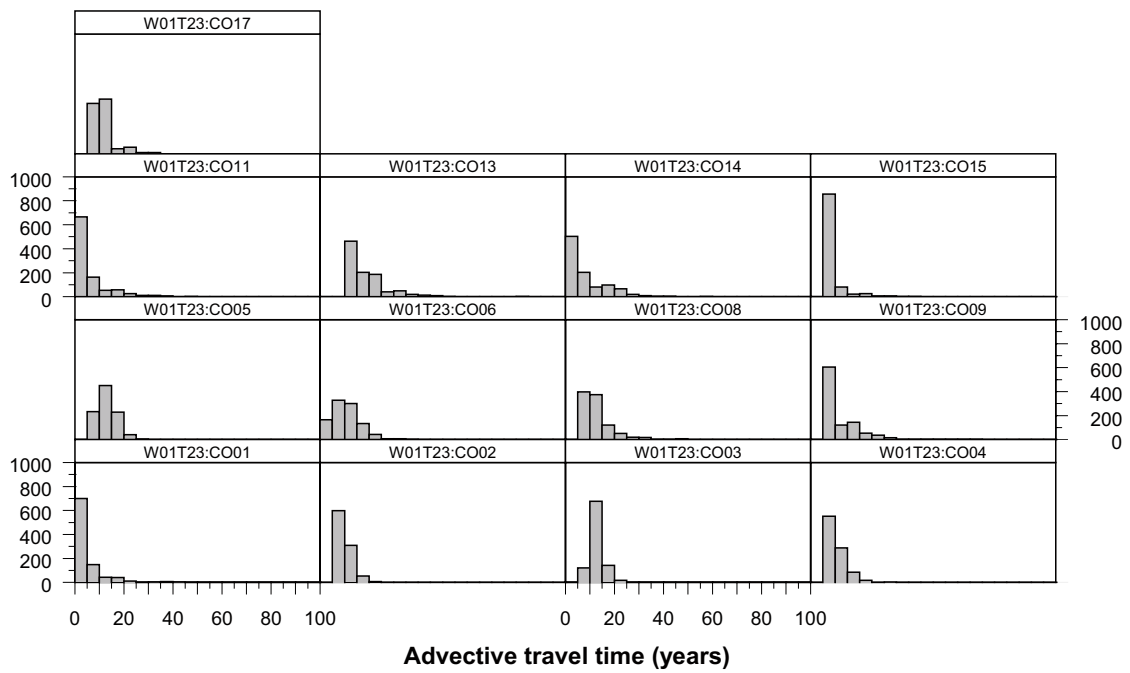
d)

Figure B-2. *Continued.*

98
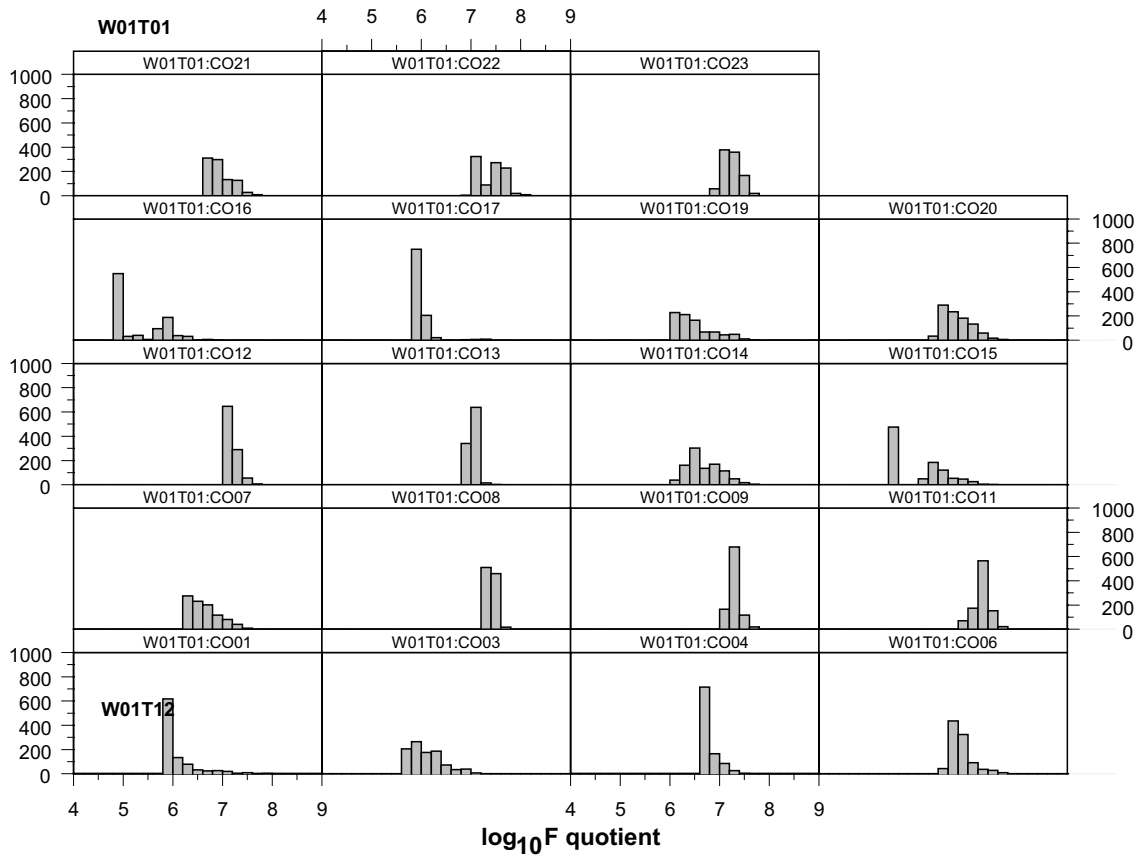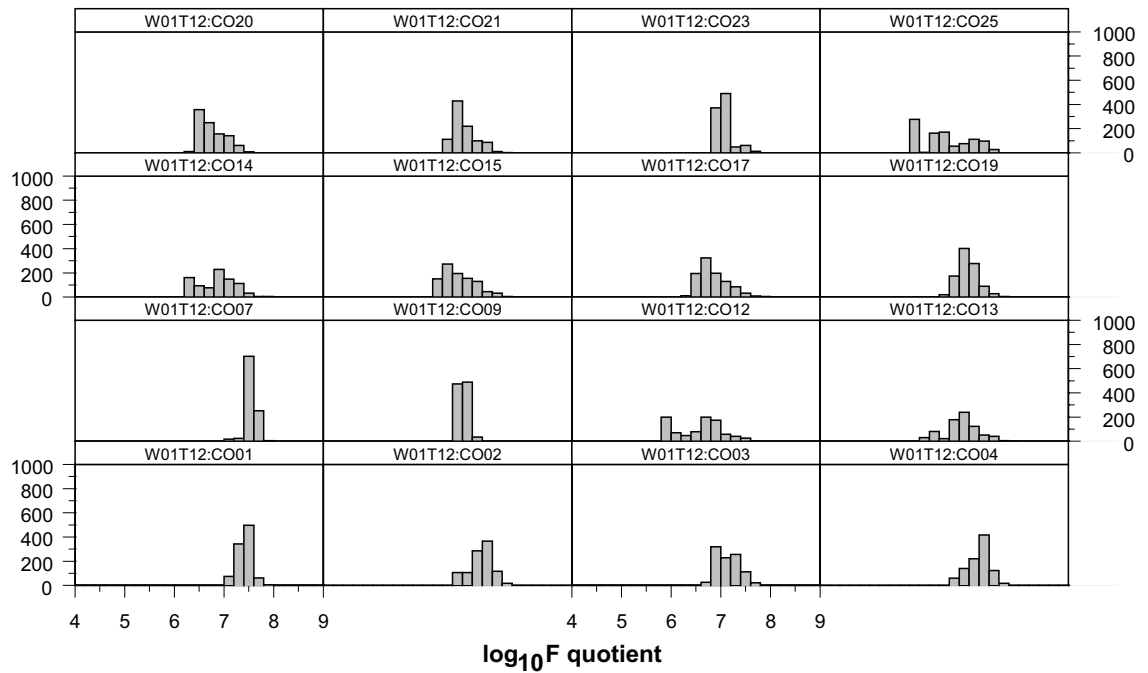
Figure B-3. *Histograms of $\log_{10}$ F quotient from particles released at the different super-container elements for W01T01, W01T12, W01T22 and W01T23.*
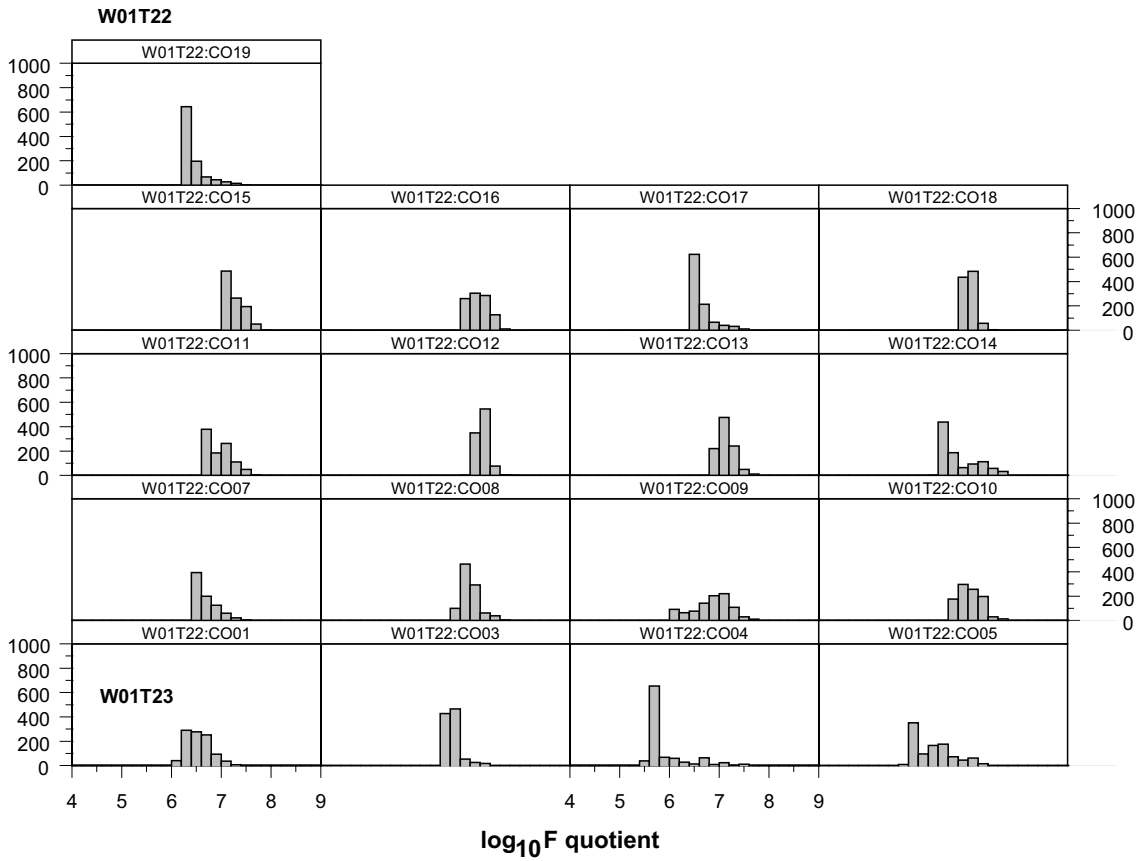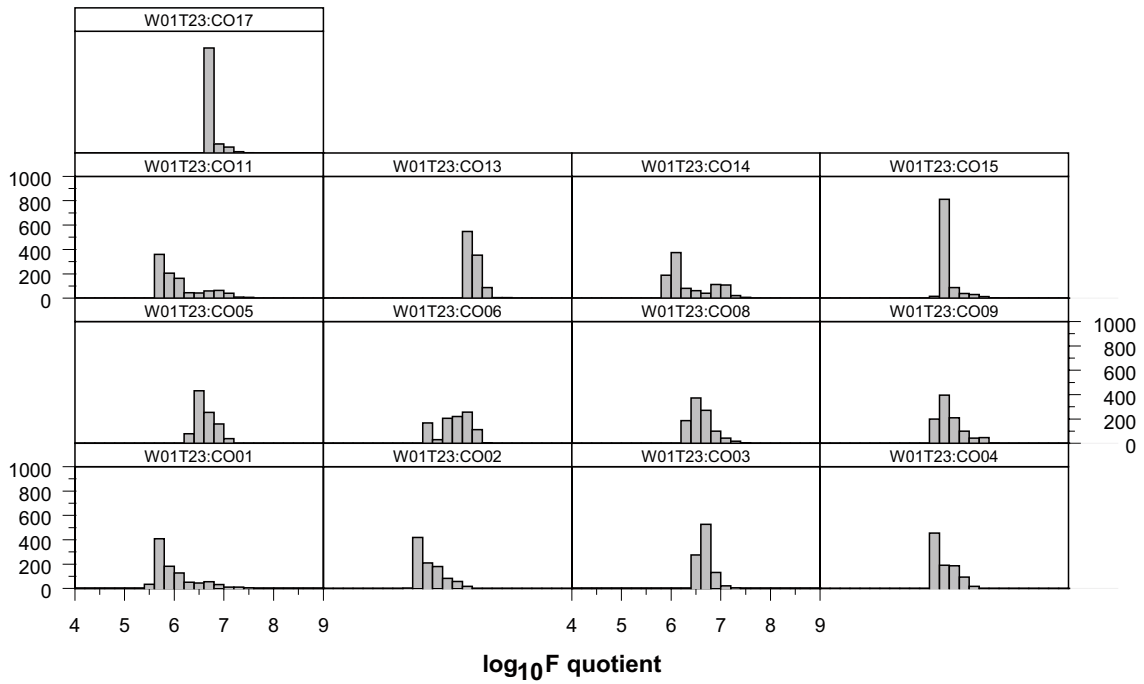
Figure B-3. *Continued.*

Calculations were performed for 10 realisations of the repository layout used in Chapter 3 for the Extended Reference Case model with transmissivity cut-offs at 10^{-10} and 10^{-11} m²/s. Figure B-4 shows the cumulative distribution for the two methods and transmissivity cut-offs.

Method 2 results in higher flow estimates as all the flow from any WCF intersection that cuts the super-container section is included in the sum. The flow estimated using Method 2 is on average about a factor of 2 higher than that calculated using Method 1. The highest value for method 1 are approximately 1.5E–10 m³/s which corresponds to the highest transmissivity features (2.69E–9 m²/s) that are allowed within a super-container section within the layout adaptation.

In the case with a transmissivity cut-off at 10^{-10} m²/s about 40% of super-container sections are interested by a WCF while with the lower cut-off about 80% are intersected. The distributions are essentially identical for the higher transmissivity fractures with $\log_{10} Q$ values above –10.5.

B.2.2   Flow model estimates of flow past a super-container

It was possible to include a more detailed representation of the drift elements within the steady state calculations for flow estimation than was used in the other models. A hybrid DFN/CPM model was used where the drift elements were represented as a CPM mesh. The fracture network model geosphere representation used was the same as that used in the transient calculations in Chapter 5. Only results from drifts W01T01 and W01T02 for one realisation are presented and they are compared with the estimates from the geometric method descried in the previous section.

Flows were measured across a cylindrical boundary positioned around the drift at 0.5 m distance from the drift wall (1.425 m from drift centre line). The flow in and out of the cylinder are calculated using the CONNECTFLOW particle tracking facility and are then allocated to individual super-containers according to the position along the cylinder. Figure B-5 shows major flow paths and particle tracks for a $100\times100\times400$ m block. Calculations have been performed for the case with minimum transmissivity of 10^{-10} m²/s and the denser fracture network where features down to 10^{-11} m²/s are included.
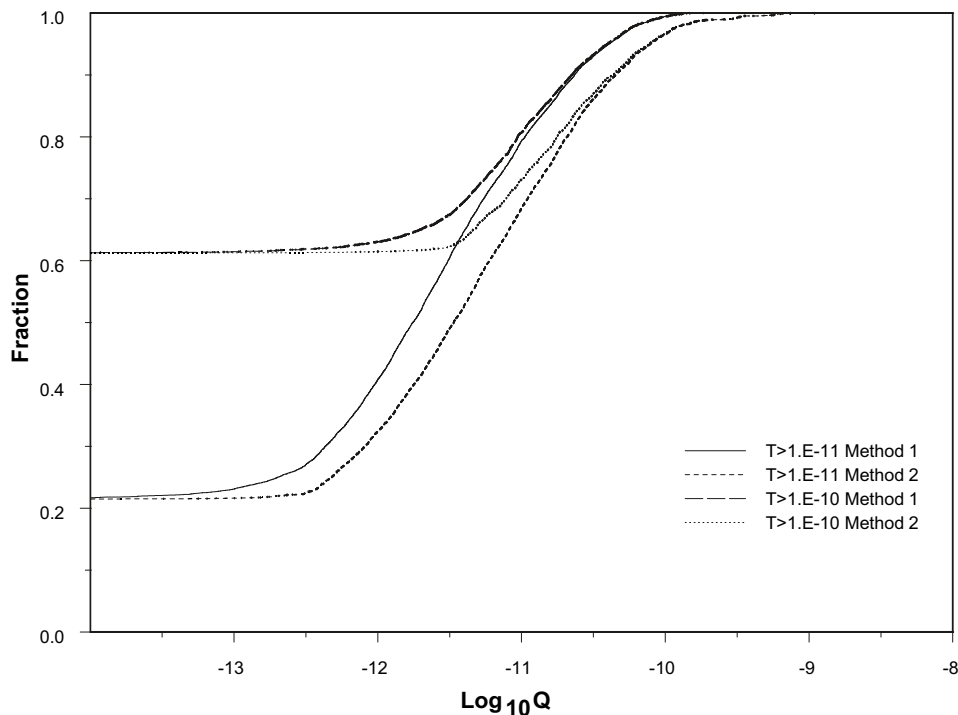
Figure B-4. *Cumulative distribution of $\log_{10}Q$ as calculated for methods 1 and 2 with transmissivity cut-offs at 10^{-10} and 10^{-11} m²/s.*
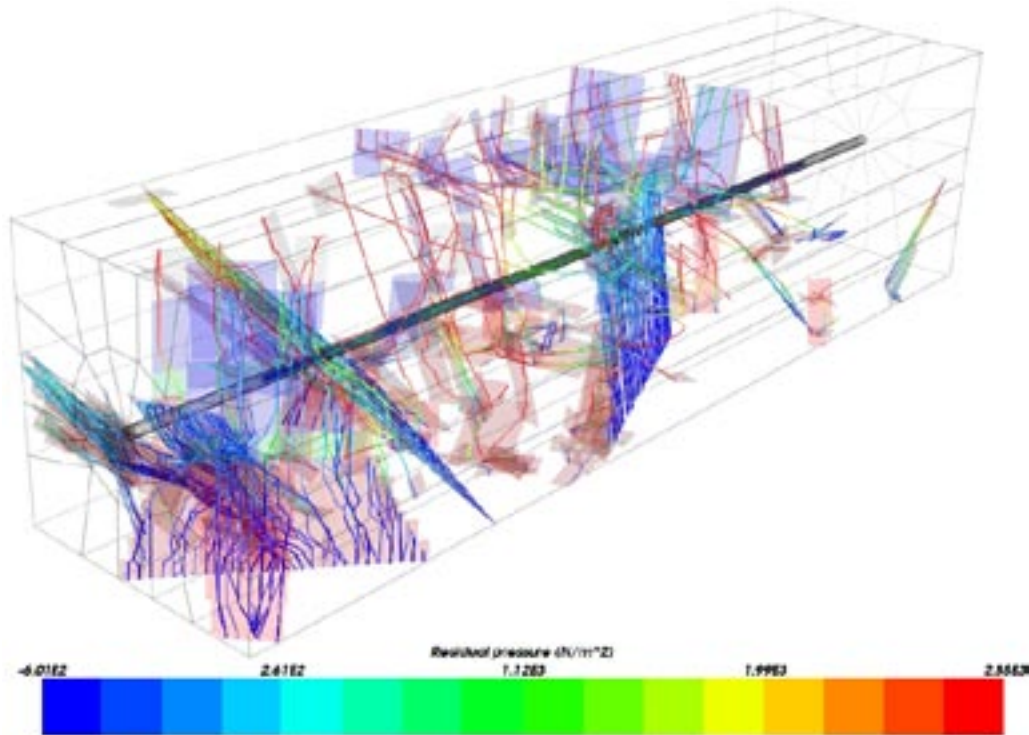
Figure B-5. *100×100x400 m block showing major flow paths and particle tracks. Fracture planes coloured by pressure and particle tracks coloured by time.*

The EBS has been represented as having a uniform permeability of 10^{-20} m^2 and no account has been taken for any differences between super-container and distance block sections (it is assumed that the bentonite has swelled and homogenised).

Table B-1 provides statistics for the flows across the super-container sections for drifts W01T01 and W01T02. Inclusion of lower transmissivity features results in a larger spread in flows as would be expected. The intersections with the measurement boundary around W01T01 are shown in Figure B-6.

A typical flow can be calculated as the gradient×transmissivity×width of the integration region. Assuming a fracture of 10^{-9} m^2/s, gradient of 0.01 and width of approximately 3 m this results in a value of 3×10^{-11} m^3/s which is in reasonable agreement with the observed values.

Table B-1. Flows across super-containers calculated from steady state flow models for drift W01T01 and W01T02.

Drift	Model Transmissivity Cutoff (m^2/s)	Super-containers not intersected	Average flow (m^3/s)	Maximum flow (m^3/s)	Mean log flow log$_{10}$(m^3/s)	Standard deviation log flow log$_{10}$(m^3/s)
W01T01	10^{-10}	15	1.5×10^{-11}	4×10^{-11}	−11.1	0.5
W01T01	10^{-11}	1	0.6×10^{-11}	4×10^{-11}	−12.0	0.9
W01T02	10^{-10}	14	0.2×10^{-11}	5×10^{-12}	−12.1	0.9
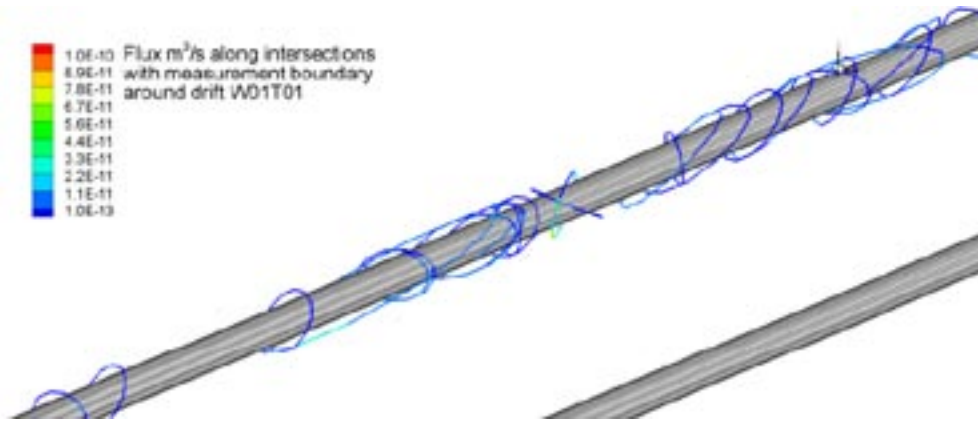
Figure B-6. *Flow on intersections with measurement boundary around drift W01T01 (model containing features $> 10^{-11}$ m²/s).*

Figure B-7 shows a comparison for W01T01 of the flow estimated from the geometric method 1 and 2 with the results from the flow models The geometric method typically over-estimates flow because the fracture intersections are calculated on a larger cylinder (2.85 diameter) and it does not account for:

- The dip of the WCF relative to the gradient.

- The connectivity of WCFs (e.g. disconnected or poorly connected features).

In poorly connected networks the local hydraulic gradient may be highly heterogeneous with very high gradients through the bottlenecks within the network. It can be seen from Figure B-7 that the geometric and flow model estimates are in good agreement. This is probably due to the well-connected nature of the fracture network, resulting in relatively uniform gradients within the fracture networks and few disconnected or poorly connected features. Geometric method 2 results in higher flows as would be expected.

B.2.3 Conclusions with regard to flow estimates

Estimates of flow across super-container sections can be calculated using either approach but the geometric approach can consider a large number of realisations and is likely to be more robust to poorly known model parameters. Open issues associated with the flow estimates are:

- Choice of gradient: a "regional gradient" has been used here, but the scale of interest for flow measurements is relatively small.

- Uncertainty on DFN parameters: as discussed previously the DFN models here are typically well-connected and models with smaller hydraulic feature sizes or very highly channelled systems might behave differently.

The good agreement between the two approaches suggests that the distribution of flows derived from the geometric approach as shown in Figure B-4 could be used as the basis for further studies of nuclide transport from super-containers although they should be considered as realistic values rather than as bounds on possible flow.
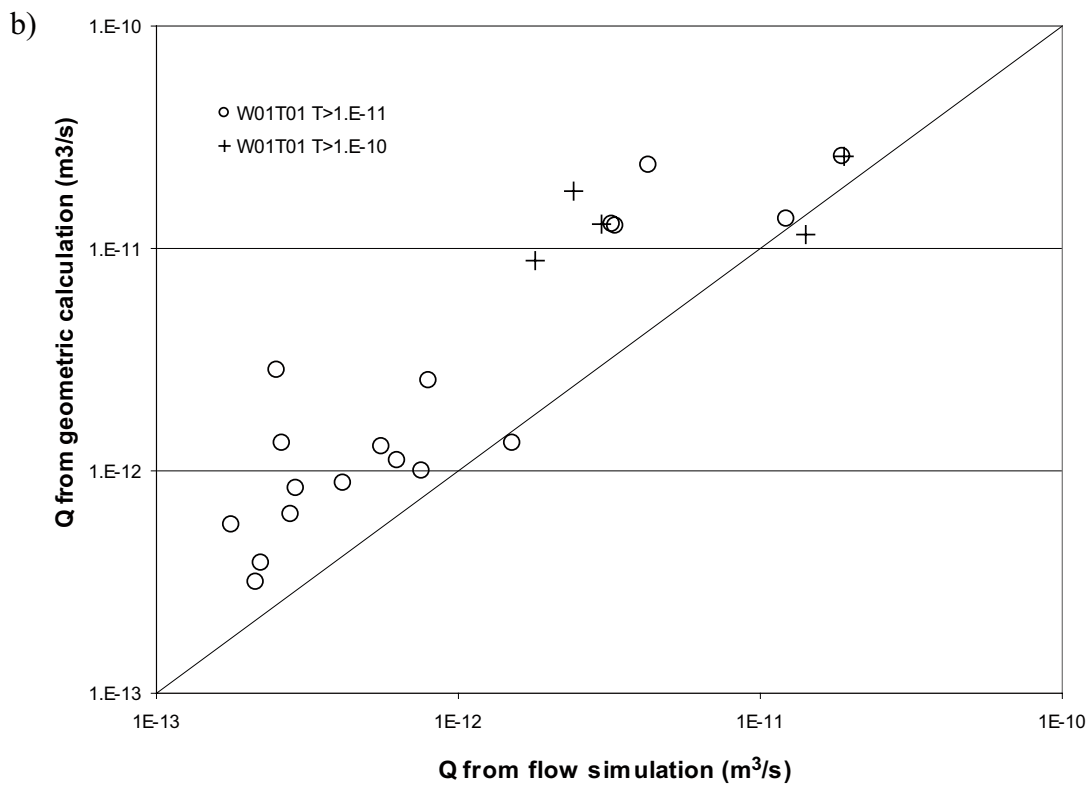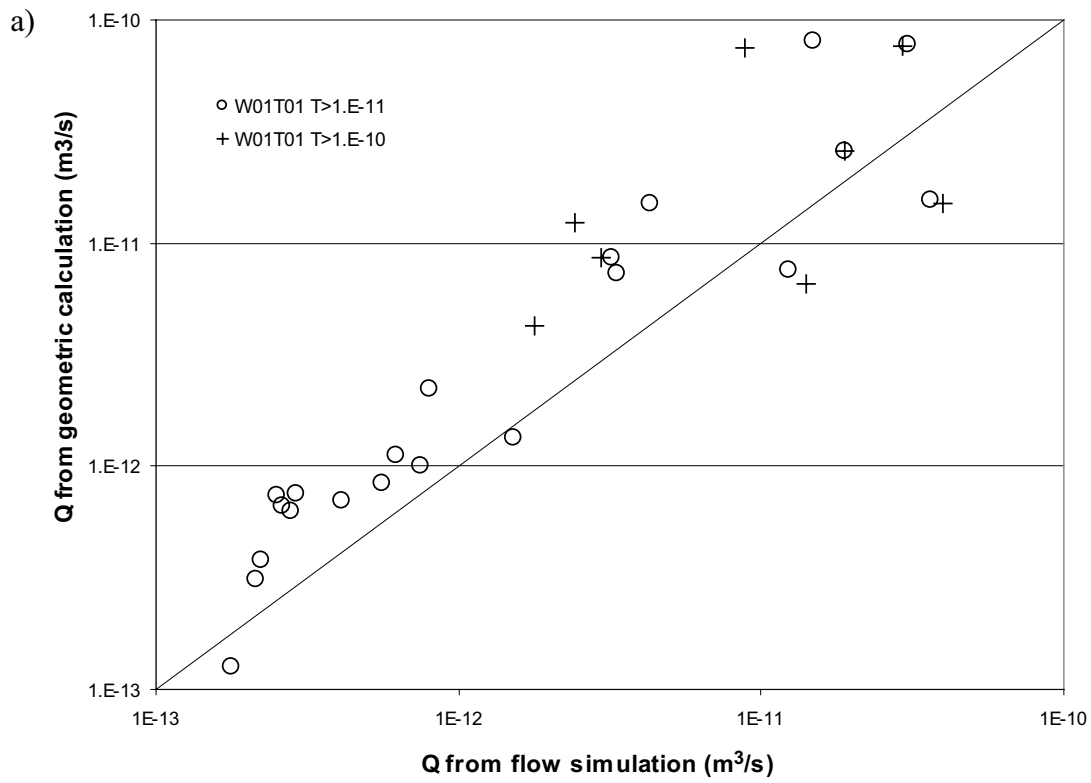
Figure B-7. *Comparison of geometric and flow model estimates of flow past a super-container for a) geometric method 1, b) geometric method 2.*

Table B-2. Particle tracking statistical summaries.

Name	Inter-section count[1]	Transmissivity (m²/s)	Lost %	Particles	Advective travel time (yrs)			Mean pore velocity (m/s)			F Quotient (yrsm)		
					Min	Mean	Max	Min	Mean	Max	Min	Mean	Max
01CO01	2	1.1E–09	4.8%	952	2.9	6.1	168.3	1.7E-08	4.4E-07	5.6E-07	6.6E+05	2.3E+06	9.4E+07
01CO03	5	3.3E–09	0.9%	991	2.5	58.9	5,885.1	3.2E-10	4.5E-07	9.2E-07	4.4E+05	1.8E+06	2.1E+07
01CO04	1	1.0E–11	0.6%	994	7.3	12.2	143.62	2.1E-08	1.8E-07	2.6E-07	4.4E+06	6.5E+06	2.8E+07
01CO05	0												
01CO06	1	3.5E–11	3.0%	970	12.3	25.3	249.79	1.9E-08	1.6E-07	2.5E-07	3.8E+06	8.3E+06	5.0E+07
01CO07	3	4.0E–10	4.4%	956	7.2	19.3	150.91	2.3E-08	2.1E-07	3.5E-07	1.6E+06	5.5E+06	3.5E+07
01CO08	1	2.0E–11	1.1%	989	28.4	43.8	139.05	1.7E-08	6.4E-08	1.1E-07	1.8E+07	2.6E+07	1.1E+08
01CO09	3	3.8E–11	1.9%	981	19.0	1.9E+06	6.07E+08	3.1E-15	7.8E-08	1.3E-07	1.3E+07	2.1E+07	6.1E+07
01CO10	0												
01CO11	1	1.3E–11	1.5%	985	13.3	37.4	118.24	2.4E-08	8.0E-08	1.7E-07	8.1E+06	2.0E+07	6.6E+07
01CO12	1	1.2E–11	0.0%	1,000	21.3	29.1	218.08	1.4E–08	9.0E–08	1.1E–07	1.2E+07	1.7E+07	1.1E+08
01CO13	1	3.2E–11	0.1%	999	12.4	20.2	63.76	3.8E–08	1.1E–07	1.5E–07	7.0E+06	1.1E+07	3.1E+07
01CO14	5	3.0E–10	0.6%	994	5.5	13.0	140.25	1.7E–08	1.9E–07	3.3E–07	1.3E+06	6.6E+06	1.0E+08
01CO15	3	2.3E–10	3.2%	968	1.3	5.6	61.903	3.0E–08	7.1E–07	1.3E–06	3.1E+05	2.2E+06	4.1E+07
01CO16	3	1.5E–09	0.1%	999	0.6	396.6	2.0E+05	8.5E–12	2.0E–06	2.9E–06	6.4E+04	5.4E+05	9.0E+07
01CO17	2	1.3E–09	0.1%	999	2.4	3.3	42.48	5.0E–08	8.3E–07	9.3E–07	8.6E+05	1.3E+06	2.5E+07
01CO18	0												
01CO19	1	4.4E–11	15.0%	850	4.7	12.5	117.55	2.3E–08	2.9E–07	5.0E–07	1.2E+06	4.9E+06	8.3E+07
01CO20	7	3.9E–10	3.9%	961	6.1	2.9E+04	1.4E+07	1.7E–13	1.7E–07	3.4E–07	1.7E+06	7.6E+06	1.0E+08
01CO21	3	5.2E–11	9.5%	905	8.8	19.9	111.67	2.6E–08	1.4E–07	2.4E–07	4.2E+06	1.0E+07	7.1E+07
01CO22	3	4.3E–11	5.3%	947	34.2	55.9	171.07	1.8E–08	5.1E–08	7.0E–08	9.9E+06	2.9E+07	1.3E+08
01CO23	2	7.1E–11	1.9%	981	19.1	34.6	94.473	3.0E–08	8.0E–08	1.3E–07	9.4E+06	1.9E+07	5.2E+07
12CO01	3	1.8E–10	1.5%	985	18.2	8.9E+04	4.4E+06	4.7E–13	5.3E–08	1.1E–07	1.1E+07	2.8E+07	1.6E+08
12CO02	2	2.3E–11	0.1%	999	10.0	40.0	158.21	2.0E–08	7.5E–08	1.8E–07	4.7E+06	1.7E+07	9.5E+07
12CO03	1	1.1E–10	2.9%	971	15.8	59.6	149.8	2.1E–08	5.2E–08	1.2E–07	5.6E+06	1.6E+07	1.0E+08
12CO04	2	1.4E–10	2.0%	980	15.9	35.8	116.9	3.0E–08	8.6E–08	1.7E–07	5.6E+06	1.7E+07	6.5E+07
12CO05	0												
12CO06	0												

Name	Inter-section count[1]	Transmissivity (m²/s)	Lost %	Particles	Advective travel time (yrs)			Mean pore velocity (m/s)			F Quotient (yrsm)		
					Min	Mean	Max	Min	Mean	Max	Min	Mean	Max
12CO07	3	7.5E–10	0.0%	1,000	24.1	99.1	137.28	2.0E–08	3.0E–08	1.0E–07	1.4E+07	3.6E+07	7.4E+07
12CO08	0												
12CO09	4	9.9E–11	0.1%	999	10.1	13.0	64.696	3.1E–08	1.5E–07	2.0E–07	4.3E+06	6.6E+06	4.8E+07
12CO10	1	8.1E–11	Not intersected by 1-D element										
12CO11	4	1.1E–09	10.1%	899	2.4	2.2E+05	2.0E+08	1.0E–14	3.2E–07	8.1E–07	6.4E+05	6.0E+06	5.0E+07
12CO12	2	7.7E–10	22.7%	773	6.7	23.3	348.83	1.0E–08	1.6E–07	3.8E–07	1.0E+06	1.0E+07	2.8E+08
12CO13	2	1.6E–10	13.8%	862	7.0	4,253.4	57,961	4.0E–11	1.5E–07	3.8E–07	1.7E+06	9.8E+06	8.6E+07
12CO14	4	4.3E–10	1.0%	990	7.7	1.6E+05	5.2E+07	5.2E–14	1.8E–07	3.5E–07	1.6E+06	7.3E+06	7.3E+07
12CO15	2	4.3E–11	1.1%	989	9.4	22.0	248.38	1.2E–08	1.4E–07	2.7E–07	2.3E+06	9.2E+06	1.9E+08
12CO16	0												
12CO17	1	1.5E–11	Not intersected by 1-D element										
12CO18	0												
12CO19	7	9.0E–10	0.5%	995	11.0	1.1E+05	1.1E+08	2.5E–14	1.2E–07	2.3E–07	3.5E+06	1.1E+07	5.9E+07
12CO20	3	6.3E–10	1.2%	988	7.6	16.3	91.58	2.7E–08	1.6E–07	2.6E–07	2.4E+06	7.1E+06	7.1E+07
12CO21	1	1.5E–11	3.2%	968	9.7	29.6	11,571	2.5E–10	1.5E–07	2.2E–07	3.0E+06	1.7E+07	8.6E+09
12CO22	1	1.8E–11	Not intersected by 1-D element										
12CO23	2	2.9E–11	1.4%	986	15.8	24.0	263.28	1.2E–08	1.2E–07	1.5E–07	9.1E+06	1.3E+07	7.3E+07
12CO24	1	1.8E–11	Not intersected by 1-D element										
12CO25	2	5.4E–10	1.4%	986	3.9	18.1	256.9	8.5E–09	2.4E–07	4.3E–07	8.8E+05	6.4E+06	4.1E+07
22CO01	5	1.7E–09	0.0%	1,000	4.5	1.8E+05	1.8E+08	9.2E–15	2.2E–07	3.6E–07	1.4E+06	5.6E+06	7.4E+08
22CO02	0												
22CO03	1	4.7E–11	0.7%	993	5.9	12.3	91.751	2.8E–08	2.0E–07	3.3E–07	2.9E+06	5.2E+06	5.4E+07
22CO04	4	1.4E–09	2.4%	976	1.8	1.1E+05	2.9E+07	5.5E–14	6.4E–07	9.3E–07	3.6E+05	1.7E+06	3.8E+07
22CO05	1	3.7E–10	0.1%	999	2.6	8.1	66.93	3.8E–08	4.0E–07	7.0E–07	6.3E+05	3.2E+06	5.4E+07
22CO06	1	2.6E–11	Not intersected by 1-D element										
22CO07	6	7.0E–10	19.3%	807	6.9	13.4	98.045	2.9E–08	2.0E–07	2.9E–07	2.7E+06	5.9E+06	7.5E+07
22CO08	1	2.8E–11	3.7%	963	9.6	23.4	78.482	3.7E–08	1.3E–07	2.1E–07	4.7E+06	1.1E+07	4.8E+07
22CO09	2	4.7E–10	5.0%	950	3.7	25.8	168.33	1.6E–08	1.4E–07	4.0E–07	1.1E+06	9.8E+06	5.7E+07

Name	Inter-section count[1]	Transmissivity (m²/s)	Lost %	Particles	Advective travel time (yrs)			Mean pore velocity (m/s)			F Quotient (yrsm)		
					Min	Mean	Max	Min	Mean	Max	Min	Mean	Max
22CO10	2	6.7E–11	2.9%	971	11.4	26.6	262.22	1.2E–08	1.0E–07	1.6E–07	4.7E+06	1.2E+07	7.0E+07
22CO11	1	1.9E–11	1.1%	989	9.7	22.3	274.06	9.1E–09	1.2E–07	1.9E–07	4.3E+06	1.1E+07	1.2E+08
22CO12	2	4.3E–11	2.1%	979	16.4	36.7	108.23	2.9E–08	7.5E–08	1.5E–07	9.7E+06	1.8E+07	7.7E+07
22CO13	3	9.1E–11	0.1%	999	14.3	27.9	150.22	2.0E–08	9.9E–08	1.8E–07	7.1E+06	1.5E+07	7.7E+07
22CO14	3	1.8E–10	1.3%	987	6.7	18.9	113.66	2.8E–08	1.8E–07	3.2E–07	2.3E+06	9.7E+06	7.6E+07
22CO15	2	2.2E–11	0.2%	998	21.6	32.3	116.32	2.5E–08	8.4E–08	1.1E–07	1.5E+07	2.1E+07	7.6E+07
22CO16	4	1.2E–10	0.9%	991	12.1	1.4E+06	4.6E+08	4.3E–15	8.9E–08	1.5E–07	6.3E+06	1.6E+07	7.1E+07
22CO17	2	2.0E–11	1.1%	989	7.7	11.1	67.198	3.8E–08	1.9E–07	2.2E–07	3.2E+06	5.3E+06	3.7E+07
22CO18	1	3.4E–11	1.7%	983	14.3	22.8	83.923	3.1E–08	9.0E–08	1.3E–07	6.3E+06	1.1E+07	4.9E+07
22CO19	1	1.7E–11	0.3%	997	6.8	9.5	95.094	2.7E–08	2.4E–07	2.8E–07	2.3E+06	3.6E+06	5.3E+07
23CO01	4	1.4E–09	3.4%	966	1.9	5.8	108.42	3.2E–08	5.8E–07	9.2E–07	3.5E+05	2.0E+06	5.1E+07
23CO02	4	8.7E–10	2.4%	976	6.2	6.3E+04	1.5E+07	1.7E–13	3.0E–07	3.8E–07	5.6E+05	1.7E+06	2.2E+07
23CO03	1	1.2E–11	3.6%	964	7.8	12.6	44.494	4.3E–08	2.0E–07	2.8E–07	2.8E+06	5.1E+06	2.4E+07
23CO04	2	4.5E–10	5.1%	949	6.3	10.5	78.507	3.9E–08	2.3E–07	3.0E–07	1.6E+06	3.7E+06	4.1E+07
23CO05	2	1.6E–10	3.9%	961	8.1	13.3	33.166	6.4E–08	1.9E–07	2.5E–07	2.3E+06	4.7E+06	1.7E+07
23CO06	3	1.2E–10	0.2%	998	3.7	2.8E+04	3.1E+06	4.8E–13	2.0E–07	4.5E–07	1.2E+06	5.5E+06	2.0E+07
23CO07	0												
23CO08	2	2.3E–10	0.5%	995	6.4	13.0	64.437	4.1E–08	2.1E–07	3.6E–07	1.7E+06	4.7E+06	3.6E+07
23CO09	2	1.0E–10	0.0%	1,000	6.3	12.4	163.51	1.8E–08	1.9E–07	2.7E–07	2.2E+06	5.0E+06	5.4E+07
23CO10	1	2.0E–10	Not intersected by 1-D element										
23CO11	1	3.7E–10	0.2%	998	3.3	7.0	48.26	5.2E–08	5.3E–07	7.9E–07	5.4E+05	2.5E+06	2.9E+07
23CO12	1	1.1E–10	Not intersected by 1-D element										
23CO13	2	2.7E–11	0.3%	997	13.1	19.3	91.741	2.4E–08	1.4E–07	1.8E–07	8.0E+06	1.1E+07	4.8E+07
23CO14	9	1.1E–09	0.4%	996	3.9	2.4E+04	2.1E+07	1.2E–13	3.1E–07	4.8E–07	9.0E+05	4.1E+06	4.0E+07
23CO15	2	3.9E–11	0.0%	1,000	6.3	9.0	54.533	4.5E–08	2.5E–07	3.2E–07	2.4E+06	4.0E+06	3.3E+07
23CO16	0												
23CO17	1	2.3E–11	0.2%	998	9.0	11.9	65.251	4.0E–08	1.9E–07	2.3E–07	4.0E+06	5.5E+06	3.2E+07

[1] Intersection count and transmissivity calculated from geometric models using volumetric representation of drifts. Particles tracking used 1-D model for drift elements.

Pressure history for the different storage models

Model and Drift Layout	W01T01	W01T12	W01T22	W01T23
Fracture Network Fractures coloured by log10 transmissivity. Fracture storativity calculated from power law baTS= a=0.25 and b=0.74.				
Excavation No dependence on drift element storage. Tunnel advance divided into drift sections (~5 m) with average 10 m/day.				
Emplacement: Storage Model A Zero storage associated with drift elements only storage in fractures. No account of time taken to fill accessible pore volume. Emplacement schedules based on Design Description for all drifts and storage models.				
Emplacement: Storage Model C Storage term for drift elements scaled up by factor 50 from Big Bertha experiments. No account of time taken to fill accessible pore volume.				

109

Model and Drift Layout	**W01T01**	**W01T12**	**W01T22**	**W01T23**
Emplacement: Storage Model D Storage term calculated from model presented in Appendix G where air volume is trapped in a rigid volume with no escape or dis/exsolution. High storage at early time as water fills and compresses air in accessible pore volume.				
Emplacement: Storage Model E "Unconfined" storage at early time as water fills accessible pore volume. When water has filled the pore volume models uses confined storage term for drift elements scaled up by factor 50 from Big Bertha experiments				
Emplacement: Storage Model E Plots show maximum pressure in each drift section versus position and time since start of emplacement.				

111

Length scales used within DFN modelling

D.1   Introduction

This section discusses the length scales used for the hydraulic features within the DFN models. Within the current study conservative values have been chosen for poorly known parameters such as feature length.

D.2   Major Fracture Zone length scales

MFZs have been modelled deterministically within the study using planar tessellations provided by Pöyry Environment from the Olkiluoto bedrock model. The MFZ tesselations for RH9, RH19A, RH19B, RH20A, RH20B, RH20C, RH21 and RH24 have typical lengths of 600 m to 2000 m with RH20C being the smallest of the zones included in the models.

D.3   Local Fracture Zone length scales

The LFZ's have been modelled as a parent planar structure with clustered WCFs sub-parallel to the parent plane. The LFZ parent planes have been modelled as 500 m square with associated WCFs 50 m in length (1/10 of WCF side-length). The 500 m LFZ side-length is below the size of the smallest of the MFZs and corresponds to the largest stochastic features used in the models of /LaPointe and Hermansson 2002/. They argued that all larger structures would be identified as deterministic features. It is likely that some of these features are in fact smaller than 500 m.

D.4   Background Rock WCF length scales

It had originally been intended to use the power law length distribution given by /LaPointe and Hermansson 2002/ as the basis for modeling of the WCFs within this study. The distributions were based on the analysis of trench data (typical scale > 1 m) and lineaments (typical scale > 1,000 m). The LaPointe and Hermansson length distributions extend from approximately 1 m to 500 m (see comment about LFZs). However, LaPointe and Hermansson consider only features greater then 10 m in diameter for the purposes of the seismic analysis performed, on the grounds that smaller fractures were very unlikely to slip more than 1 mm.

Within the DFN flow models it was also decided to use only fractures greater than 10 m in size, on the grounds that small fractures would typically be poorly connected and not contribute significantly to flow.

CONNECTFLOW uses a different convention to that used by LaPointe and Hermansson in Posiva report WR-2002-02. CONNECTFLOW assumes that the fracture length power exponent is that of the probability density function (pdf) while LaPointe and Hermansson gives the exponent of the cumulative density function (cdf), which is 1 greater than that of the pdf. The values given in WR 2002-02 in the DFN modelling were used directly without adding the 1 that would be necessary to make them consistent with LaPointe and Hermansson's usage (see Table D-1). This problem was not identified until after the completion of the modelling

The result is that the fracture length distribution for BR-WCFs used in the DFN models includes more large fractures than the distribution specified by /LaPointe and Hermansson 2002/. The models already neglected the contribution of small fractures (below 10 m in length) assuming that all flowing features are at least 10 m in size. The length scale exponents (for cumulative density function) given by LaPointe and Hermansson and those used in the DFN modelling are given in Table D-2 below. The length scale distributions used in the models are similar to the length scale distribution used by /Hellä et al. 2006/ where all sets use an exponent of 1.6.

Table D-1. Comparison of power-law distribution conventions used by LaPointe and Hermansson and as used in CONNECTFLOW.

	Lapointe and Hermansson (Pareto distribution)	CONNECTFLOW (Power-law distribution)
Power law slope exponent	k	b
Minimum scale	x_m	x_m
Cumulative density function	$P(X.x) = \left(\dfrac{x}{x_m}\right)^{-k}$	$P(X.x) = \left(\dfrac{x}{x_m}\right)^{-b+1}$
Distribution mean	$\dfrac{kx_m}{k-1}$ for $k>1$	$\dfrac{(b-1)x_m}{b}$ for $b>2$

Table D-2. Comparison of power-law CDF exponents.

	LaPointe and Hermansson Power law cdf exponent	KBS-3H DFN models Power law cdf exponent
WCF Set 1	2.5	1.5
WCF Set 2	2.72	1.72
WCF Set 3	2.66	1.66

D.5 Impact on models of using lower exponent for BR-WCFs

The KBS3H DFN models contain fewer but larger features and are better connected than would be the case if they had used the higher power-law exponents given by LaPointe and Hermansson (op cit). The number of intersections in the models along 1D features (e.g. boreholes) is the same as the total fracture surface area in the models is constant (calibrated to observation). However "connectivity" effects would be much more important with the higher exponents and more work would be needed to calibrate the observed transmissivity distribution. The KBS-3H DFN models were typically well-connected resulting in only minor connectivity issues (e.g. disconnected and poorly connected features), this was one reason why a good calibration to the observed well test data was achieved in the DFN models.

D.5.1 Geometric models

When considering drift intersections a larger number of "small fractures" would result in more partial intersections with fracture or intersections with disconnected features. This would result in additional transmissive features that would require sealing (compartment plugs) or need to be avoided (blank zones) depending on the rules used (disconnected features within the models would have been ignored). However the impact of additional small fractures due to the higher exponent is probably small compared to the choice of ignoring fractures below 10 m in size.

D.5.2 Upscaling calculations

The lower connectivity of the networks using higher exponents would result in lower effective hydraulic conductivity. The KBS-3H DFN models were thought to be conservative anyway because of the choice of sizes for the LFZs.

D.5.3 Flow models

Given the difficulties of running the transient calculations for the different cases, models using the higher exponent with more fractures would probably have been impractical given the computing resources available. However it might have been possible to build models where small fractures are only included close to the drift. The difference on model results from using higher exponents would be:

- The drifts would be less well connected to the boundary conditions, indicating potentially lower inflows.

- In two-drift models the drifts would be less well connected to each other (fewer direct connections between the drifts – but the lower connectivity to the boundaries might result in greater pressure drops).

D.6 Conclusions

Given the purpose of the models: to provide insight into the processes associated with the evolution of the KBS-3H repository system and the other uncertainties associated with the modelling e.g.:

- Storage model uncertainty and influence of bentonite saturation.
- Neglect of small fractures (< 10 m).
- Use of 1D drift representations.
- Simplified treatment of LFZs and WCFs.

The length scale distributions used are felt to provide a reasonable representation of possible fracture flow behaviour at the scales of single drifts and of likely intersection statistics at repository scale, although the role of small fractures or small-scale flow channelling represents a significant uncertainty associated with the models.

Future modelling of the fracture system should use the LaPointe and Hermansson distributions but will need to address the importance (or otherwise of small fractures). A schematic of the different length scales used in the models is shown in Figure D-1.
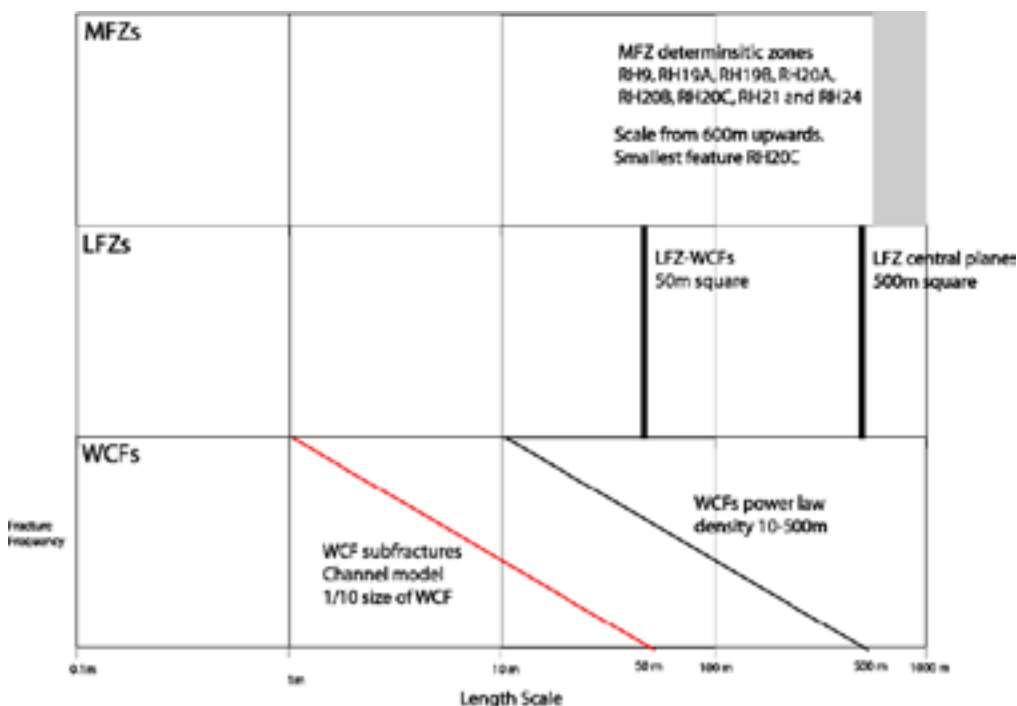
Figure D-1. *Length scales of different features used in DFN modelling.*

Input data used to derive KBS-3H DFN models

This appendix identifies the input data used to develop the KBS-3H DFN flow models. The datasets were provided as spreadsheets by Pöyry Environment but are traceable to the reports identified here.

Inflow database

The database of borehole inflows and analysis of the inflow dataset is given in /Hellä et al. 2006/.

Structures database

The database of identified borehole structure intersections was taken from /Vaittinen et al. 2003/.

HTU double packer test data

The HTU (double packer) test data was a compilation of the data reported in the references /Hämäläinen 1997abcde, 2003abc, 2004ab, 2005, 2006ab/ (see Chapter 7 above).

List of input parameters for KBS-3H process report and evolution report

A list of input parameters to be used in the HMCGB analyses of steel components has been defined in the Appendix A of the report by Johnson L, Marschall P, Wersin P and Gribi P (2005) HMCBG processes related to the steel components in the KBS-3H disposal concept, Posiva Working Report 2005-09.

These parameters have been checked and updated for the KBS-3H Process Report and Evolution Report. The Table F-1 presents the list of parameters due to 15062006 (PM KBS-3H Safety Case 11/2005).

The checking of parameters has been done on all of those parameters, which are independent of the design options. The materials and dimensions for the new design options BD and DAWE will be compiled by the end of year 2006 as the design is on a more mature stage. However, the dimensions and masses for the fixing rings and steel plugs for the BD are included in the attached Table.

The data has been reviewed and checked by Jorma Autio, Lennart Börgesson, Bo Halvarsson and Margit Snellman.

Table F-1. Input parameter values for the HMCBG analyses presented in this report.

Parameter	Unit	Symbol	Reference value	Alternative values	Comment/ Ref.
System Description					
Repository depth					
one-storey	m		400		/Vieno 2004/
two-storeys	m			400 and 500	/Vieno 2004/
Deposition drift					
diameter	mm	$2\,r_t$	1,850	1,840	/Börgesson et al. 2005/
length	m		300		/Vieno 2004/
separation between drifts	m	d	25	40	/Vieno 2004/
drift dip	°		2 +/–1		Meeting 28.05.04
drift orientation	–		parallel to max. stress		/Vieno 2004/
Canister					
outer diameter	m	$2\,r_c$	1.05		/Börgesson et al. 2005/
length	m	l_c	4.835		/Halvarsson 2005/
pitch (center-to-center distance)	m m	p_c	10.9(Posiva) 10.2(Posiva)	8.6 (SKB) 8.1 (SKB)	BWR PWR
Supercontainer (perforated)					
total mass	kg		[850 kg, 890 kg with feet]		/Halvarsson 2005/
length	mm	l_{sc}	5,560 +5/0		/Halvarsson 2005/
feet	kg		40.2		/Halvarsson 2005/
outer diameter	mm	$2\,r_{sc}$	1,765		/Börgesson et al. 2005/
inner diameter	mm		1,749		/Börgesson et al. 2005/
thickness (of end plates)	mm		8		/Börgesson et al. 2005/

Parameter	Unit	Symbol	Reference value	Alternative values	Comment/ Ref.
radius of perforation holes	mm		100		/Börgesson et al. 2005, Blix 2004/
degree of perforation	%		62		/Börgesson et al. 2005, Blix 2004/
Distance blocks					
diameter	mm		1,765	1,845	/Börgesson et al. 2005/
length (depending on drift sep.)	mm		5,350 (25 m)	3,050 (40 m)	BWR /Vieno 2004/
			4,650 (25 m)	2,550 (40 m)	PWR /Vieno 2004/
void slot (option DAWE)	mm		37.5–42.5		/Börgesson et al. 2005/
pellet-filled slot (DAWE)	mm		37.5–42.5		/Börgesson et al. 2005/
void slot (Basic Design)	mm		0–5		/Börgesson et al. 2005/
Supporting feet, 4 feet per block, total mass	kg		13.9		/Halvarsson 2005/
Bentonite blocks					
initial water content	w–%		10		/Börgesson et al. 2005/
saturated density after swelling	kg m^{-3}		2,000		/Börgesson et al. 2005/
saturated porosity after swelling	%	ε_b	44		/SKB 1999/
swelling pressure	MPa		7–8	8.7 in SKB TR 99-07	Meeting 28.05.04
gap to canister (radial)	mm		5		/Börgesson et al. 2005/
gap to super container (radial)	mm		5		/Börgesson et al. 2005/
diameter end blocks	mm		1,740		/Halvarsson 2005/
diameter ring blocks	mm		1,740		/Halvarsson 2005/
length end blocks	mm		350		/Börgesson et al. 2005/
length ring blocks	mm		4,844 (4×1,211)		/Halvarsson 2005/
Bentonite pellets					
initial water content	w–%		10		/Börgesson et al. 2005/
initial density	kg m^{-3}		1,000		/Börgesson et al. 2005/
dry density	kg m^{-3}		909		/Börgesson et al. 2005/
Supporting feet (supercontainer)					
material type	–		steel		
total mass (per canister)	kg		40.2		10 feet per supercontainer
Supporting feet (distance block, DAWE)					
material type	–		steel		
total mass (per canister)	kg		13.9		4 feet per distance block
Fixing ring to prevent movement of distance block (BD)					
material type	–		10 mm thick steel plate		
total mass	kg		600	1,200	/Autio 2006/
Steel compartment plug					
material type	–		10 mm steel plate		
total mass	kg		1,400	2,800	/Autio 2006/

Parameter	Unit	Symbol	Reference value	Alternative values	Comment/ Ref.
Geochemical and biological conditions					
Host rock chemistry					
Salinity	g l^{-1}		10–25	25–45	/Posiva 2003, Vieno 2004/
Alkalinity	meq l^{-1}		0.4	0.1–1	/Posiva 2003/
pH			7.5–8.2		/Posiva 2003/
Redox potential	mV		–300..–250	≈ – 200	/Posiva 2003, Pitkänen et al. 2004/
Redox conditions			methano-genic	sulphidic	/Posiva 2003/
Degradable organic matter (n.a)	% rock		0		Meeting 28.05.04
Dissolved Fe(II)	mg l^{-1}		0.07	0–0.5	/Pitkänen et al. 2004/
Dissolved gases					
H_2	ml l^{-1}		< 0.1 generally	7–268 (a max.value below 800 m)	Not near saturation /Gascoyne 2000/ /Pitkänen et al. 2004/
CH$_4$	ml l^{-1}		< 400 generally at depths down to 500 m	770–990 (max.values below 800 m)	Near sat.in saline water <800 m, /Gascoyne 2000/ /Pitkänen et al. 2004/
Solubilities at 30°C (after. approx. 2000a /SKB 1999/ p. 100) and 0.1 MPa					
H_2	mol m^{-3} ml l^{-1}		0.77 19		/Himmelblau 1960/
CH$_4$	mol m^{-3} ml l^{-1}		1.3 33		/Himmelblau 1960/
Bentonite					
Bentonite type			MX–80		TILA-99
Porewater composition					e.g. /Vuorinen et al. 1998/ Table 2-2 saline water reducing conditions.
Fe(II) mineral content (pyrite, siderite)	%		1	0	/Müller-Vonmoos and Kahr 1983/
Steel corrosion rate	μm a^{-1}	R	1	2	/Smart et al. 2004/
				1–2	Sensitivity anal.
Rock properties					
Gneiss: fracture properties					Sparsely fractured rock and occasional "vein-like sections" /Vieno 2004/; see also /Posiva 2003/ and note at the end of this paper.
fracture type	–		fractures	vein-like	
orientation	–		several sets		
density	m^{-1}	N	1–3	3–10	
aperture	mm	a	calc. from T-distribut.		
transmissivity	m^2 s^{-1}	T	10^{-14}–10^{-7}		
hydraulic conductivity	m s^{-1}		10^{-8}–10^{-15}		/Börgesson et al. 2005/
Gneiss: average matrix properties					
porosity	%	ε_m	0.14	0.1–0.2	/Autio 2004/*
hydraulic conductivity	m s^{-1}		1E–14	≈< 1E–15	/Hautojärvi 2004/
gas effective diffusion constant	m^2 s^{-1}		2.63E–10		/Autio 2004/
intrinsic gas permeability	m^2		5.16E–21		/Autio 2004/

Parameter	Unit	Symbol	Reference value	Alternative values	Comment/ Ref.
EDZ: properties of crushed zone (0–4 mm)					
thickness (radial extent)	mm		4		/Autio 2004/
porosity	%		0.64	2–4	/Autio 2004/
fracture type	–		open cracks		/Autio 2004/
mean fracture aperture	μm		2		/Autio 2004/
small fractures (< 5.4 μm)	%		90		/Autio 2004/
larger fractures (> 5.4 μm)	%		10		/Autio 2004/
EDZ: properties of microfractured zone (4–9 mm)					
thickness (radial extent)	mm		5		/Autio 2004/
porosity	%		0.34		/Autio 2004/
fracture type	–		open cracks		/Autio 2004/
mean crack specific surface	μm^{-1}		0.004		/Autio 2004/
small fractures (< 2.16 μm)	%		60%		/Autio 2004/
EDZ: properties of zone of minor damage (9–23 mm)					
thickness (radial extent)	mm		14		/Autio 2004/
fracturation	–		similar as in undisturbed rock		/Autio 2004/
EDZ: average properties (0–23 mm)					
porosity	%	ε_{EDZ}	0.34		/Autio 2004/
gas effective diffusion constant	m^2 s^{-1}		3.97E–9		/Autio 2004/
intrinsic gas permeability	m^2		2.96E–19		/Autio 2004/***
Hydraulic properties					
Leakage rates for 300 m drift (operational phase)	litres·min^{-1}				/Vieno 2004, Hellä et al. 2006/
long dry sections			"dry"		
1–3 local fracture zones			>4 (one per 250 m)		Range of inflow from local fracture zones
a few fractures or fracture zones (per 100 m)			0.4–4 (one per 100 m)		
six 5 m long sections (per 300 m)			>0.1		
four to five 10 m long sections (per 300 m)			>0.1		
total leakage per compartment			10 (total)		e-mail MS 5.11.05 On the average four transimissive fractures (> 0.01 l/min) per 100 m sample length
Total leakage per drift			30 (total)		e-mail MS 5.11.05
Saturation time	a		10	12,000	Meeting 28.05.04
Hydraulic gradient (post-closure phase)	m m^{-1}		0.01		/Vieno 2004/

Parameter	Unit	Symbol	Reference value	Alternative values	Comment/ Ref.
Thermal properties					
Ambient temperature	°C	T_0	+10.5°C (400 m)		/Ikonen 2003/, gradient 1.5°C/100 m
Heat output	W				/Vieno 2004/
BWR canister			1,700		
PWR canister			1,370		
Thermal conductivity (gneiss)	$Wm^{-1}K^{-1}$		2.7		/Posiva 2003/, p. 114
Heat capacity (gneiss)	$J\,kg^{-1}K^{-1}$		797		/Posiva 2003/, p. 114
Thermal diffusivity (gneiss)	$m^2\,s^{-1}$		1.23E–06		/Posiva 2003/, p. 114
Thermal conductivity (bentonite)	$Wm^{-1}K^{-1}$		1.0		/Vieno 2004/
Maximum temperature at canister surface (for thermal dimensioning)	°C		90		10° below the design basis max. of 100°; /Vieno 2004/

Notes:

*   These values represent Gneissic tonalite in the Research Tunnel at Olkiluoto.

**   Scaling factor to convert to diffusivity of heavier molecules in water saturated samples by 1/35,000 /Autio et al. 1999/.

*** Hydraulic conductivity can be calculated using permeability /e.g. Autio et al. 1999/.

F.1   References for Table F-1

Autio J, 2004. Description of excavation damaged zone (EDZ) around a KBS-3H deposition drift, PM KBS-3H Safety case 10/2004, Saanio & Riekkola Oy, Helsinki.

Autio J, 2006. KBS-3H Design Description 2005. Working Report 2006-xx. Posiva Oy, Olkiluoto, (in preparation).

Autio J, Kirkkomäki T, Siitari-Kauppi M, Timonen J, Laajalahti M, Aaltonen T, Maaranen J, 1999. Use of 14C-PMMA method and He-gas methods to characterize excavation disturbance in crystalline rock. POSIVA 99-22, Posiva Oy, Helsinki.

Blix P, 2004. Sweco PIC, SKB KBS-3H finite element analysis of supercontainer, (15. Nov. 2004): (Found at Projectplace).

Börgesson L, Sandén T, Fälth B, Åkesson M, Hökmark H, 2005. Behaviour of the buffer in KBS-3H, SKB TR-05-50, Svensk Kärnbränslehantering AB.

Gascoyne M, 2000. Dissolved gases in groundwaters at Olkiluoto. Working Report 2000-49. Posiva Oy, Helsinki.

Halvarsson B, 2005. Based on drawings M-011C, M-025_revA, M-026, M-027B, M-028B, M-029B, and M-030C, Projectplace.se.

Hautojärvi A, 2004. Interview by Ari Ikonen, June 15, 2004.

Hellä P, Ahokas H, Palmén J, Tammisto E, 2006. Analysis of geohydrological data for assessment of the alternative repository layout KBS-3H. Working Report 2006-16. Posiva Oy, Olkiluoto.

Himmelblau D M, 1960. Solubilities of inert gases in water. J. Chem. Eng., Vol. 5/1, January 1960.

Ikonen K, 2003. Thermal Analyses of KBS-3H Type repository. POSIVA 2003-11, Posiva Oy, Olkiluoto.

Johnson L, Marschall P, Wersin P, Gribi P, 2005. HMCBG processes related to the steel components in the KBS-3H disposal concept. Working Report 2005-09. Posiva Oy, Olkiluoto.

Müller-Vonmoos M, Kahr G, 1983. Mineralogische Untersuchungen von Wyoming Bentonite MX-80 und Montigel. Nagra Technical Report NTB 83-12, Nagra, Wettingen, Switzerland.

Pitkänen P, Partamies S, Luukkonen A, 2004. Hydrogeochemical interpretation of baseline groundwater conditions at the Olkiluoto site. POSIVA 2003-07, Posiva Oy, Olkiluoto.

Posiva, 2003. Baseline conditions at Olkiluoto. POSIVA 2003-02, Posiva Oy, Olkiluoto.

SKB, 1999. SR 97 – Processes in the repository evolution. SKB TR-99-07, Svensk Kärnbränslehantering AB.

Smart N R, Rance A P, Werme L O, 2004. Anaerobic corrosion of steel in bentonite. Mat. Res. Soc. Symp. Proc. 807, 441–446.

Vieno T, 2004. Olkiluoto site data for KBS-3H design and analysis. PM KBS-3H Safety case 9/2004, Saanio & Riekkola Oy, Helsinki.

Vuorinen U, Kulmala S, Hakanen M, Ahonen L, Carlsson T, 1998. Solubility database for TILA–99. POSIVA 98-14, Posiva Oy, Helsinki.

Pressure build-up model of Poteri

G.1 Pressure build-up assuming no gas escape from the super container section (extract from memo by Antti Poteri VTT)

This appendix studies a case where water flow into a closed section of tunnel. At the beginning the tunnel is not saturated by water. The pore space is filled by air that is not able escape from the closed tunnel section. This situation can be conceptualised by a closed container that is filled by the inflowing water (Figure G-1). It is assumed that the inflowing water comes along a fracture that is connected to a large reservoir of water that is able to maintain constant pressure (P_r). The evolution of the water inflow rate and build-up of the pressure inside the closed section of the tunnel is governed by the compression of the air.

It is assumed that the trapped air behaves as a perfect gas. It is also assumed that there is no gas in the fractures (i.e. the flowing water flushes the gasses away from the fractures). Dissolution of the gas/air into the water is not taken into account because it is regarded to be a slow process compared to the water inflow.

The closed section of tunnel contains bentonite. Water leakage to the bentonite is not taken into account. The leakage is assumed to be small, and on the other hand, the bentonite swells about the amount of water intake. This means that leakage to the bentonite does not affect the pressure build-up process considered in this study.
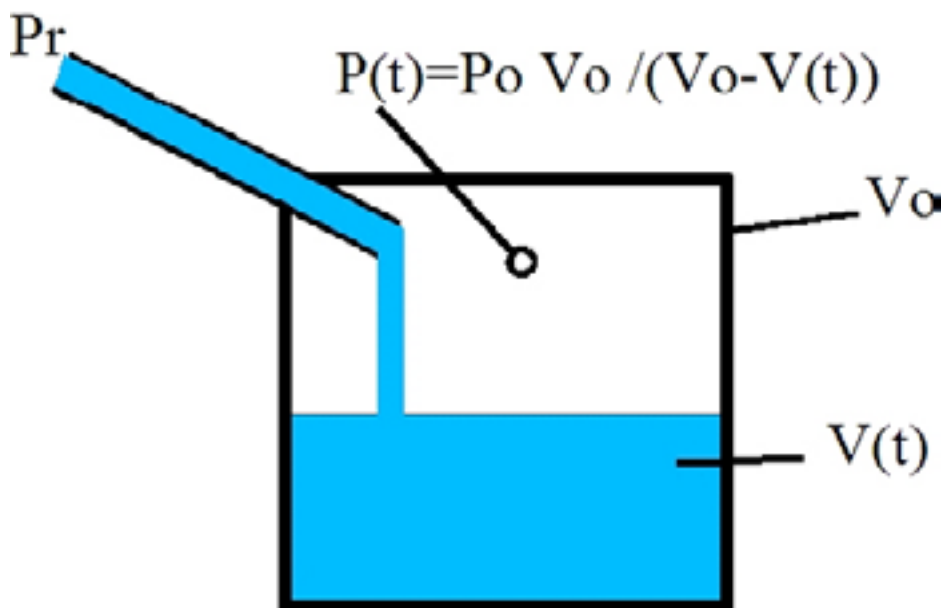
Figure G-1. Conceptualisation of the groundwater flow to open tunnel.

It is assumed that at the beginning there is a pressure Po in the void space. The volume of the void space is Vo. Water flows to the void space through a fracture that is connected to a constant pressure of Pr in the bedrock. Then the flow rate to the tunnel is

$$\frac{dV(t)}{dt} = k\,\Delta P(t) = k\,(P_r - P(t)) \tag{6}$$

where P(t) is the time dependent pressure in the void space of the tunnel and k is the conductance of the fracture. The flowing groundwater fills up the void space in the tunnel. This causes a pressure build-up in the void space, because the void space is filled by the inflowing water

$$P(t) = \frac{P_o V_o}{V_o - V(t)} \tag{7}$$

where V(t) is the total volume of water that has entered tunnel during the time [0,t].

Substituting (7) to (6) and solving the equation for the initial condition V(0) = 0 gives

$$V(t) = \frac{V_o}{P_r}\left\{ P_r - P_o - P_o\, \mathbf{W}\!\left(\frac{P_r - P_o}{P_o}\, \mathbf{Exp}\!\left[\frac{P_r(V_o - k\,P_r t)}{P_o V_o} - 1 \right] \right) \right\} \tag{8}$$

where W(x) is a solution for W in $x = \mathbf{w}\,\mathbf{Exp(w)}$.

Flow rate to the void space is calculated as a time derivate of (8)

$$\frac{dV(t)}{dt} = k\,P_r\left\{ 1 - \frac{1}{1 + \mathbf{W}\!\left(\dfrac{P_r - P_o}{P_o}\, \mathbf{Exp}\!\left[\dfrac{P_r(V_o - k\,P_r t)}{P_o V_o} - 1 \right] \right)} \right\} \tag{9}$$

Pressure in the void is given from (7) (or more easily using (6) and (9))

$$P(t) = \frac{P_r}{1 + \mathbf{W}\!\left(\dfrac{P_r - P_o}{P_o}\, \mathbf{Exp}\!\left[\dfrac{P_r(V_o - k\,P_r t)}{P_o V_o} - 1 \right] \right)} \tag{10}$$

then the pressure build-up rate can be calculated as a time derivate of (10)

$$\frac{dP(t)}{dt} = \frac{k\,P_r^3}{P_o V_o}\, \frac{\mathbf{W}\!\left(\dfrac{P_r - P_o}{P_o}\, \mathbf{Exp}\!\left[\dfrac{P_r(V_o - k\,P_r t)}{P_o V_o} - 1 \right] \right)}{1 + \mathbf{W}\!\left(\dfrac{P_r - P_o}{P_o}\, \mathbf{Exp}\!\left[\dfrac{P_r(V_o - k\,P_r t)}{P_o V_o} - 1 \right] \right)} \tag{11}$$

Equations (8) to (11) are below plotted for following cases:

Void space in the atmospheric pressure at the beginning and at the depth of 500 metres below the surface:

- V_o = 1,500 litres.
- P_r = 5 MPa.
- P_o = 0.1 MPa.

Two different leakage rates are considered:

- k = 60/5 litres/hour/MPa, this gives a leakage of about 60 litres/hour at the initial state.

- k = 6/5 litres/hour/MPa, this gives a leakage of about 6 litres/hour at the initial state.
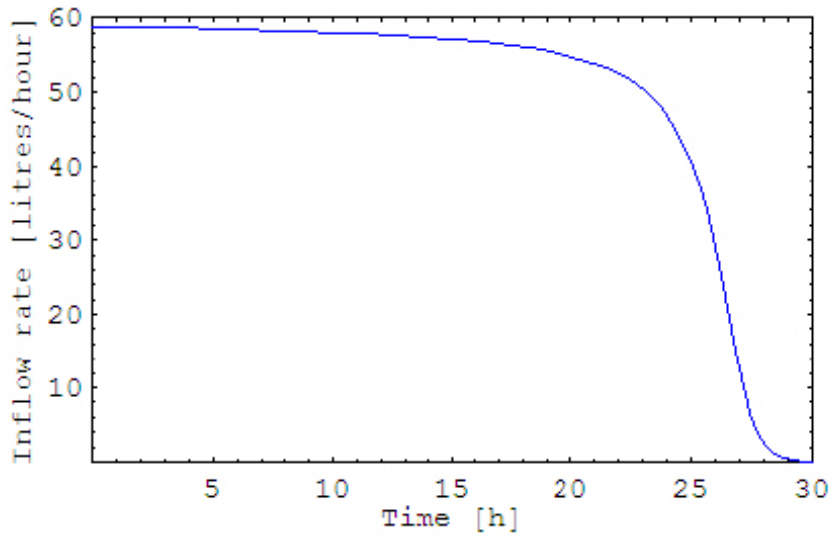
The rationale to select these flow rates is that we cannot allow a leakage that is higher that 1 litre/min and a leakage that is smaller than 0.1 litre/min is not a problem.
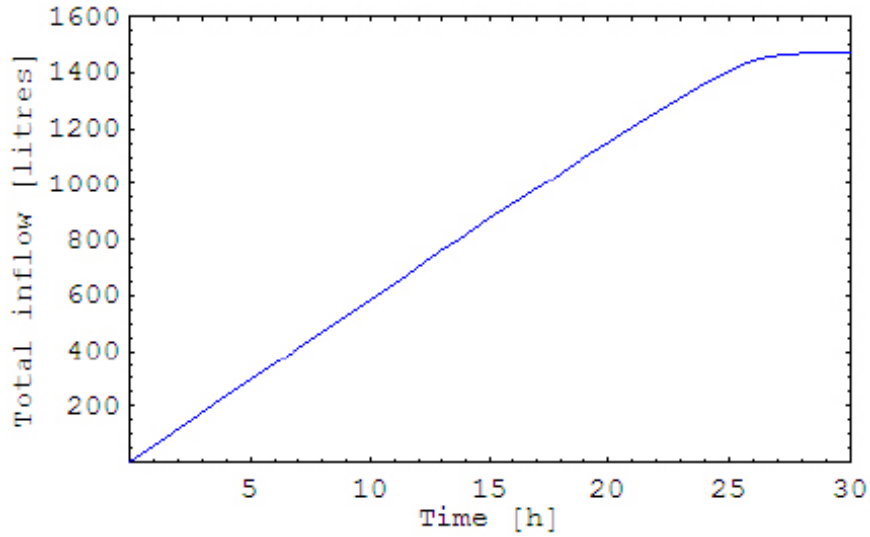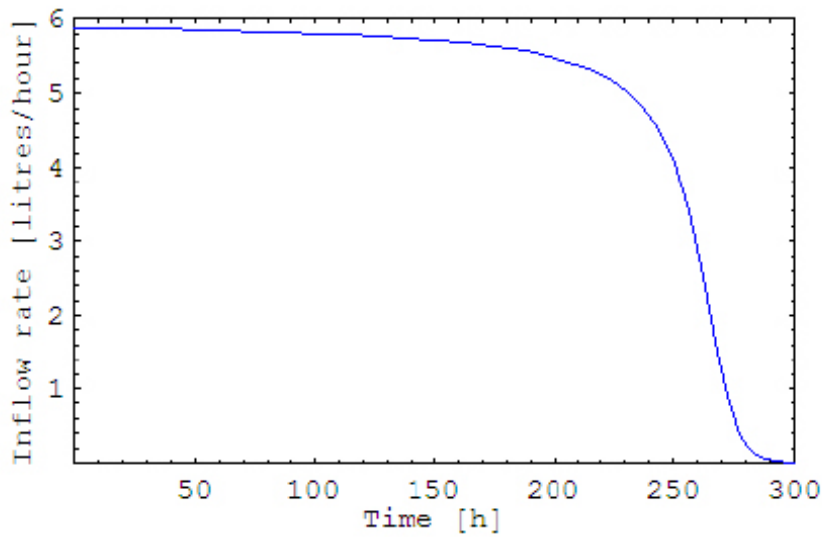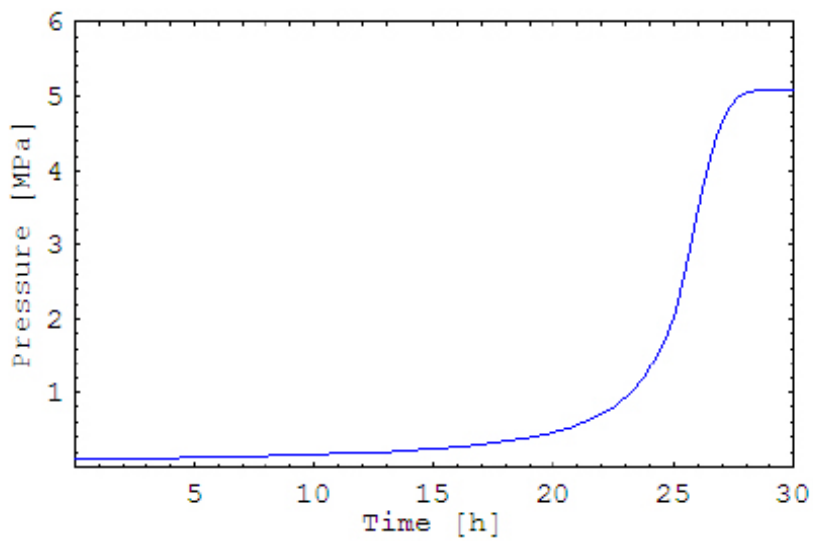

Figure G-2. *Integrated inflow to the void space. Leakage rate 60 litres/hour.*
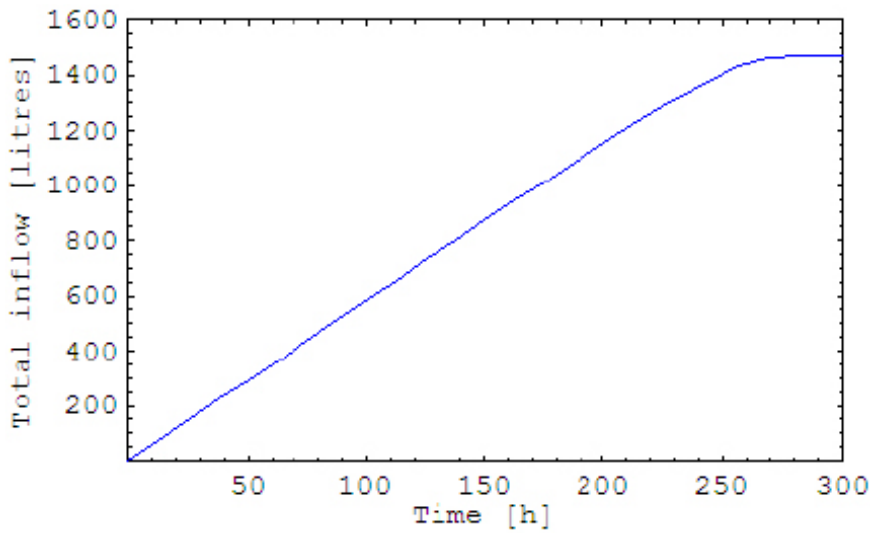
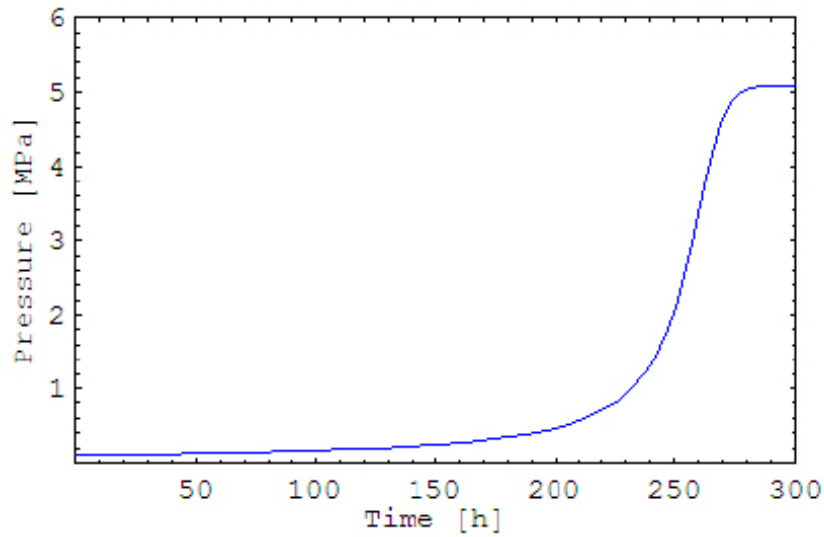**Figure G-3.** *Integrated inflow to the void space. Leakage rate 6 litres/hour.*

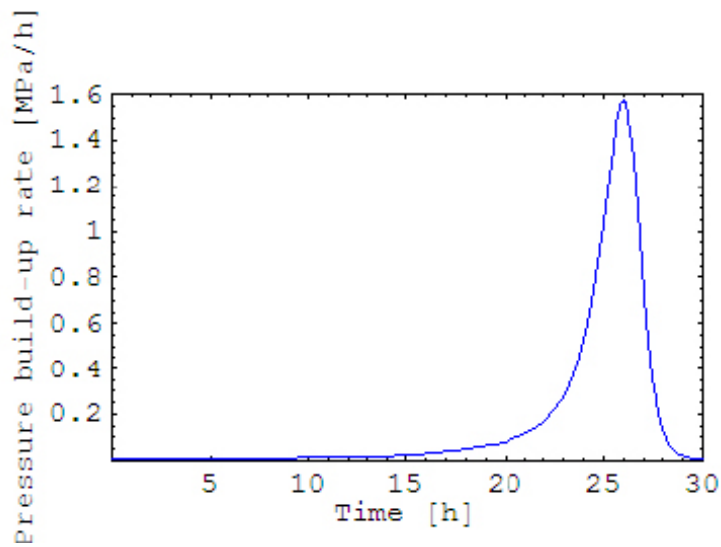**Figure G-4.** *Inflow rate. Leakage rate at the beginning 60 litres/hour.*

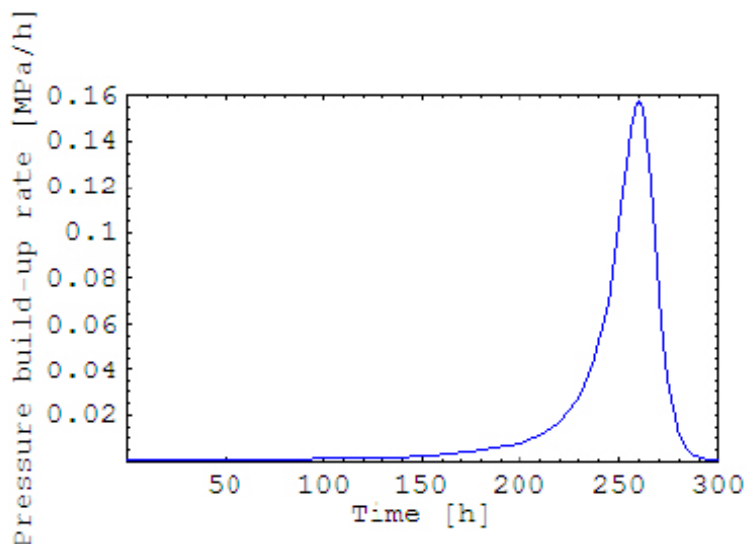**Figure G-5.** *Inflow rate. Leakage rate at the beginning 6 litres/hour.*

Figure G-6. *Pressure in the void space. Leakage rate at the beginning 60 litres/hour.*

Figure G-7. *Pressure in the void space. Leakage rate at the beginning 6 litres/hour.*

Figure G-8. *Pressure build-up rate. Leakage rate at the beginning 60 litres/hour.*

Figure G-9. *Pressure build-up rate. Leakage rate at the beginning 6 litres/hour.*